Mesoscopic Models of Stochastic Transport

Active Particles, Molecular Motors and Resistive Switching

Dissertation

zur Erlangung des akademischen Grades

doctor rerum naturalium

(Dr. rer. nat.)

im Fach: Physik

Spezialisierung: Theoretische Physik

eingereicht an der

Mathematisch-Naturwissenschaftlichen Fakultät

der Humboldt-Universität zu Berlin

von

M.Sc. Paul Kaspar Radtke

Präsidentin der Humboldt-Universität zu Berlin

Prof. Dr. Sabine Kunst

Dekan der Mathematisch-Naturwissenschaftlichen Fakultät

Prof. Dr. Elmar Kulke

Gutachter/innen:

1. Lutz Schimansky-Geier
2. Harald Engel
3. Ulrich Behn

Tag der mündlichen Prüfung: 14. September 2017

Abstract

Transport phenomena occur in biological and artificial systems at all length scales. In this thesis, we investigate them from a mesoscopic perspective, in which fluctuations around their average properties play an important role. The transport processes are active, i.e. they consume energy in dissipative systems outside of thermal equilibrium. They will be dealt with using concepts of stochastic processes, such as ratchets, Langevin equations and master equations.

In the first part, we investigate the unbiased diffusive motion of active Brownian particles with an additional torque. It can appear in many real life systems, for example in sperm cells, bacteria, nanorods and Janus particles. They are driven by a correlated noise modeled by the Ornstein-Uhlenbeck process, which leads to a persistence in their motion. By confining the Brownian particles into an infinite channel geometry of varying width, biased transport appears in a nonequilibrium situation, where the noisy drive and the dissipation of momentum are decoupled. This way, we have realized a novel kind of ratchet.

In the second part, we study intracellular cargo transport in the axons of nerve cells. It is performed by molecular motors walking on the cytoskeleton, which is modeled by an asymmetric exclusion process model, i.e with a hopping process on a lattice. For high motor densities, jams of motors emerge. In a new approach, we add a cargo exchange interaction between the motors. This way, the characteristics of slow axonal transport, such as a motor density dependent cargo transport speed and transport direction reversals, can be accounted for with a single motor species. It is explained by the transient attachment of cargos to reverse walking motors jams, which can be considered as quasi particles.

In the third part, we discuss resistive switching, the non-volatile change of resistance in a dielectric due to electric pulses. It is exploited for applications in computer memory. We propose a stochastic lattice hopping model based on the on oxygen vacancies. The transport of the vacancies alters the electric properties of the switch. We define binary logical states by means of the underlying vacancy distributions, and establish a framework of writing and reading such a memory element with voltage pulses. Considerations about the discriminability of these operations under fluctuations together with the markedness of the resistive switching effect itself enable us to predict an optimal vacancy number.

Zusammenfassung

Transportphänomene treten in biologischen und künstlichen Systemen auf allen Längenskalen auf. In dieser Arbeit untersuchen wir sie aus einer mesoskopischen Perspektive, in der Fluktuationen physikalischer Größen um ihre Mittelwerte eine wichtige Rolle spielen. Die Transportprozesse sind aktiv, d.h. sie verbrauchen Energie in dissipativen Systemen außerhalb des thermischen Gleichgewichts. Wir betrachten sie mittels der Konzepte stochastischer Prozesse, unter anderem Ratschen, Langevin Gleichungen und Master Gleichungen.

Im ersten Teil untersuchen wir die im Mittel symmetrische diffusive Bewegung Brownscher Teilchen mit zusätzlichem Drehmoment. Sie tritt vielen realen Systemen auf, so z.B. bei Spermien, Bakterien, Nanostäbchen und Janusteilchen. Die Brownschen Teilchen werden von einem korrelierten Rauschen getrieben, welches durch den Ornstein-Uhlenbeck Prozess modelliert wird und zu einer persistenten Bewegung führt. Wird ihre Bewegung auf einen unendlichen Kanal mit variierender Breite beschränkt, tritt im Nichtgleichgewicht, wo der rauschende Antrieb und seine Dissipation entkoppelt sind, Transport in eine bevorzugte Richtung ein. Dadurch haben wir einen neuen Ratschentyp realisiert.

Im zweiten Teil betrachten wir intrazellulären Frachttransport in den Axonen von Nervenzellen. Der Transport wird von auf dem Zytoskelett entlanglaufenden molekularen Motoren geleistet. Wir modellieren ihre Bewegung durch einen asymmetrischen einfachen Ausschluss-Prozess, d.h. einem Hüpfprozess auf einem Gitter. Bei hohen Motordichten treten Staus auf. In einem neuen Ansatz führen wir einenzusätzlichen Frachtaustausch zwischen den Motoren ein. Dadurch lassen sich charakteristische Eigenschaften des langsamen axonalen Transports mit einer einzigen Motorspezies reproduzieren: eine motordichtenabhängige Frachttransportgeschwindigkeit, und Umkehrungen der Transportrichtung. Bewerkstelligt wird dies durch die transiente Anbindung der Fracht an rückwärtslaufende Staus, welche als Quasiteilchen betrachtet werden können.

Im dritten Teil diskutieren wir *resistive switching*, die nicht volatile Widerstandsänderung eines Dielektrikum durch elektrische Impulse. Es wird für Anwendungen im Computerspeicher ausgenutzt. Wir schlagen ein stochastisches Gitterhüpfmodell vor, das auf Sauerstoffvakanzen basiert. Der Transport der Vakanzen ändert die elektrischen Eigenschaften des switches. Wir definieren binäre logische Zustände mit Hilfe der zugrunde liegenden Vakanzenverteilung und definieren Schreibe- und Leseoperationen durch Spannungsimpulse für ein solches Speicherelement. Überlegungen über die Unterscheidbarkeit dieser Operationen unter Fluktuationen zusammen mit der Deutlichkeit der unterschiedlichen Widerstandszustände selbst ermöglichen es uns, eine optimale Vakanzenzahl vorherzusagen.

Contents

1. Introduction **1**
1.1. Guide to the Thesis 2

I. Geometrical Transport of Active Particles with Torque **5**

2. Brownian Motion and the Rectification of Noise **7**
2.1. Brownian Particles and Active Motion 7
2.2. Diffusion of a Brownian Particle in the Langevin Picture 8
2.3. The Feynman-Smoluchowski Ratchet 10
2.4. Biased Motion in Dynamical Systems 12

3. Persistent Motion and Transport of Brownian Particles with Torque **15**
3.1. Introduction 15
3.2. Persistent Motion of Brownian Particles in Thermal Equilibrium . . 17
3.2.1. Fokker-Planck Equation and its Stationary Free Solution . . 19
3.3. Persistent Motion of Active Particles 22
3.3.1. Diffusion 23
3.3.2. Directed Transport in Confined Geometries 25
3.3.3. Elucidation of the Transport Mechanism 29
3.4. Conclusion 30

II. Transport by Molecular Motors Across the Cytoskeleton **33**

4. Intracellular Transport **35**
4.1. The Cytoskeleton and Molecular Motors 35
4.2. From the Brownian Ratchet to a Hopping Process 37
4.3. The Asymmetric Simple Exclusion Process 41

5. A Cargo Hopping Model for Slow Axonal Transport **47**
5.1. Introduction 47
5.2. The Hopping Model of Cargo Transfer 48
5.3. Numerical Study: Jamming and Cluster Formation 50
5.4. A Mean Field Analysis 55
5.5. Cargo Transport with the Clustering Mechanism 56

5.6. Summary and Outlook 58

III. Resistive Switching **63**

6. Resistive Switching **65**
6.1. Occurrence and Mechanisms of Resistive Switching 65
6.2. Applications: ReRAM in 3d Stackbars and Neuromorphic Computing 67
6.3. Theoretical Background: the Memristor as the Fourth Basic Passive Circuit Element 71
6.4. The HP-memristor 73

7. A Nonlinear HP-Type Complementary Resistive Switch **79**
7.1. Introduction 79
7.2. A Nonlinear HP-Memristor. 80
7.3. The CRS Composed of Two Nonlinear HP-Memristors 84
7.4. Summary 87

8. Stochastic Dynamics of Resistive Switching with Two Active Zones **89**
8.1. Introduction 89
8.2. A Stochastic Vacancy Hopping Model for Bipolar Resistive Switching 91
8.3. General Dynamics 93
8.3.1. Effects of Fluctuations 97
8.3.2. Continuum Limit and Generalized Burgers' Equation for Wave Transit 98
8.4. Logical States 101
8.4.1. Reading and Writing Operations 101
8.4.2. Clarity and Stability of the Reading Operation 103
8.5. Conclusion 105

9. Comparison of the Resistive Switching Models and Outlook **109**
9.1. Comparison of the Deterministic and Stochastic RS-Models 109
9.2. Is the Particle Based RS-Device a Memristor? 112
9.3. Outlook: A Langevin Model of Resistive Switching 113

IV. Conclusions **115**

A. Appendix **123**
A.1. Simulation Details of the VEOV-Model 123
A.2. Derivation of the Burgers' Equation 124

1. Introduction

Transport phenomena occur in biological systems at almost all levels of organization, ranging from individual molecules to the complex locomotion of higher animals. Cells need to transport nutrients absorbed at their membrane to the nucleus and proteins synthesized therein in the reverse direction [80, 120]. Bacteria follow chemical gradients to acquire food or escape toxic environments [38, 96]. Complex animals hunt for prey and escape predators.

All of these are active processes which happen outside of thermal equilibrium in open systems. From a physical point of view, the internal complexity of living organisms can only be build up or kept by exporting entropy, for which the systems need to expend free chemical energy. Indeed, one of the primal motivations for motion of living beings is gathering this energy in the form of food. Or to escape from those who want to make them their food - the inner complexity of a salmon is reduced quite dramatically when it is decomposed into its constituent amino acids in the stomach of a bear.

Some of these transport processes have analogues in artificial systems, for example the locomotion of bacteria and sperm cells [46, 47, 181] with a flagellum closely resembles the motion of nanorods [118, 161] and Janus particles [4, 105] in a water peroxide solution. In other artificial systems, such as plasmas of charged particles [93, 106, 165], transport can be induced by an external forcing, like external magnetic and electric fields. The goal of the transport processes can be either to actually transport cargo to its destination, or to alter the physical properties of a larger system by changing parts of its machinery. The dopant drift in transition metal oxides for example is not only interesting in its own right, but far more importantly changes the electric properties of the media [150, 184]. An effect that is exploited for applications in computer memory [72, 184, 192].

In this thesis, we will deal with transport processes on a mesoscopic level. The mesoscale is the loosely defined area in between microscopic and macroscopic objects. For a physicist, the term microscopic usually describes systems of a few atoms or molecules, for which quantum effects are dominant. Macroscopic objects on the other hand contain huge numbers of particles and are usually governed by classical mechanics and thermodynamics, with average properties determined from its constituent materials. Mesoscopic objects contain a large number of atoms also, but their behavior is severely affected by fluctuations around average properties and quantum effects may also be present.

In a heuristic example, a macroscopic view of a ball is just that: a ball. From a

microscopic point of view the quantum mechanical interactions of a few atoms and molecules may be considered. A mesoscopic view may contain a set of larger molecules in a roughly spherical shape with thermal fluctuations and effective interactions between them.

The methods used to study mesoscopic objects reflect the chance and fluctuations characterising their behavior. For instance, chemical reaction processes are described by a master equation, reflecting that a reaction only takes place with a certain probability that is proportional to the densities of the molecules taking part in the reaction and their reaction rates. Stochastic differential equations take into account the noisy forces acting on the particles due to random collisions with the environment. And interactions between different particles will be handled by effective forces, which are not derived from microscopic interactions bottom-up.

1.1. Guide to the Thesis

In the present work, we will investigate mesoscopic models for stochastic transport with applications in three different subfields of physics. Each corresponds to a part of this thesis and is composed several chapters: an introduction, which covers the physical or biological background and the employed methods, and the main body containing our research in the respective areas.

In **part I**, we discuss the diffusional motion of Brownian particles with an additional constant torque. They are driven by random fluctuations modeled by an Ornstein-Uhlenbeck process with nonzero correlation time. It causes a persistent motion and is implemented (i) as thermal noise in equilibrium and (ii) as noisy propulsion of active particles in nonequilibrium. If the particles are further confined to a channel geometry of varying width, in the nonequilibrium case directed transport emerges. This way, we have realized a novel kind of ratchet, in which the unbiased circular motion of active Brownian particles is rectified. We elucidate the transport mechanism and interpret its qualitative behavior with regard to the different time scales in the particles dynamics.

In **part II**, we investigate the intracellular transport of cargos by molecular motors walking on the cytoskeleton. The motors are first considered as Brownian particles diffusing on a potential landscape. With the influx of chemical energy, a conformation ratchet is realized and biased transport emerges. The internal dynamics is simplified to a hopping process governed by a master equation, for which interactions with other motors on a crowded track are taken into account in form of an exclusion process. Such a process is then used to develop a model for cargo transport in the axon of nerve cells. Therein, on top of the motor's motion, cargos can transiently bind or hop to neighboring motors. The cargo transport speed and direction can be controlled by the density of motors on the track, reproducing experimental results in a minimal mesoscopic model. Within a mean field approximation together with phenomenological assumptions about the clustering of motors, we derive an analytical

expression for the stationary cargo velocity.

In **part III**, we study resistive switching (RS), the non-volatile change in the resistance of a dielectric due to the action of an external electric field. Its main application, the resistive random access memory, favors the anti-serial combination of two switches to an composite resistive switch (CRS). The memristor, the fourth basic passive circuit element, is introduced as the idealized concept behind RS.

First, we develop an analytically treatable memristor model to describe the CRS. Motivated by the irregular shape of the filament protruding into the device, we suggest a nonlinearity in the resistance-interpolation function.

Second, we account for fluctuations, which play an increasing role upon the miniaturization of resistive switches, by formulating a stochastic model. It is based on the motion of oxygen vacancies, governed by a master equation. Upon the application of a voltage pulse, the vacancies collectively travel wave-like through the switch, which we verify by deriving a generalized Burgers' equation. Further, we define binary logical states by means of the underlying vacancy distributions, and establish a framework of writing and reading such a memory element with voltage pulses. Considerations about the discriminability of these operations under fluctuations together with the markedness of the resistive switching effect itself will enable us to predict on optimal vacancy number for the performance.

In **part IV**, we will revisit the main motivations, results and outlooks of the individual parts, with an emphasis on the connecting elements between them.

Part I.

Geometrical Transport of Active Particles with Torque

2. Brownian Motion and the Rectification of Noise

Brownian motion is the archetypical problem in the theory of stochastic processes. The erratic, jittery motion of pollen particles immersed in water is the result of countless unpredictable collisions of the pollen particles with water molecules. It can be described in statistical terms only. Fascinatingly, these collisions are both the source of friction and noisy drive of the particles. The question arises, if the noise can be harvested to perform work.

In this chapter, we will introduce some of the concepts used throughout the thesis. At first, a short historic background of the diffusive motion of Brownian particles in physics is given, which we then formalize by means of stochastic differential equations. Afterwards, we introduce the concept of the rectification of noise using the example of the Feynman-Smoluchowski ratchet. The flashing ratchet shows how this can be altered for the directed transport of Brownian particles. Finally, we make a short excursus to Sinai billiards, dynamical systems whose geometrical tunnel structure leads to a separated phase space in which transport occurs.

2.1. Brownian Particles and Active Motion

The notion of Brownian particles first emerged when the botanist Robert Brown observed the stochastic motion of pollen grains from the plant *Clarkia pulchella* in 1827, which were suspended in water. The pollen grains performed a jittery motion, which he initially attributed to the 'life force'. However, later experiments with inorganic matter showed the same effects, whose origin was ultimately unknown at the time.

Eventually, the phenomenon was explained in Albert Einstein's groundbreaking discussion [37] in the language of modern statistics (a similar approach was developed independently by Smoluchowski [167]). By balancing the diffusion current with the drift current through Stokes' law, Einstein obtained a relation between the particle diffusion coefficient and the fluid friction. This connection, also called the Einstein relation, was later generalized to the **fluctuation-dissipation theorems** (**FDT**) in the work of Callen and Welton [21].

In the second part of his 1905 paper Einstein derives the overdamped diffusion equation heuristically. With its help, he predicts that the root of the mean square displacement of Brownian particles is proportional to the square root of time. This

allowed for easy experimental validation of the predictions. It was no longer required to determine the velocity from the trajectories of Brownian particles, but only the distance travelled. Indeed, the velocity was hardly accessible due to the erratic and non-differentiable motion of Brownian particles. In effect, the theory of Brownian motion formed a cornerstone in the atomistic theory and was used by Perrin to determine the Avogadro-Loschmidt number experimentally.

The approach of Einstein was later translated into the Newtonian language of equations of motion by Paul Langevin [94]. He supplemented Newtonian equations of motions with a stochastic force, a language more familiar to physicists.

A further important contribution was made by Lars Onsager's regression hypothesis [124], and the linear response formalism of Kubo [90]. Together, these contributions allowed the study of stochastic systems out of equilibrium, i.e., particles driven by non-thermal noise.

Today, many descriptions of biological agents work in this framework, for example the motion of bacteria [157] or the emergence of swarming effects in locusts [12].

2.2. Diffusion of a Brownian Particle in the Langevin Picture

Here, we introduce the conceptions of diffusive motion and stochastic differential equations using the example of a free Brownian particle. More detailed presentations can be found in one of the many standard texts dealing with stochastic processes, such as [51, 82, 136].

Let us consider a small particle that is thrown into a fluid with an initial impulse. It will travel a certain distance until its directed motion eventually stops. This is due to constant collisions with the fluids' molecules, hence after some time the particle's momentum has dissipated into all directions. Therefore, a description of its motion has to include a counteracting friction force. The simplest choice is a linear drag according to Stokes' Law

$$F_S(t) = -\gamma_0 v(t), \tag{2.1}$$

with particle's velocity $v(t)$ and the friction coefficient γ_0. If the particle is small enough, the collisions not only stop it, but deflect it into other directions as well. The source of these deflections are the thermal fluctuations of the fluids' molecules, whose properties are known in statistical terms only. Therefore, the description of such a mesoscopic particle has to include a random force F_R. With the position x and mass m, this leads to the equation of motion

$$\dot{x}(t) = v, \qquad m\dot{v}(t) = F_S(t) + F_R(t). \tag{2.2}$$

The random force is equivalently referred to as noise. To give eq. (2.2) a well defined meaning, we have to make demands on the nature of the random force. First we require its mean to vanish in thermal equilibrium, $\langle F_R(t)\rangle_{\text{eq}} = 0$. Second, we specify

its autocorrelation function $c_{FF}(s) = \langle F_R(t)F_R(t+s)\rangle$ by assuming

$$\int_{-\infty}^{\infty} c_{FF}(s)\mathrm{d}s = 2\mathcal{D}_\xi m^2, \tag{2.3}$$

with $\mathcal{D}_\xi$ denoting the noise intensity. One solution of eq. (2.3) is a weighted delta distribution

$$c_{FF}(t) = 2\mathcal{D}_\xi m^2 \delta(t). \tag{2.4}$$

This a valid assumption, if the mean time between two successive collisions of the Brownian particle with the fluid is much shorter than other characteristic time scales of the system. It is not the only conceivable solution of eq. (2.3), we will encounter a correlated random force in chapter 3.

Third, we assume that $F_R(t)$ obeys a Gaussian distribution. Therefore its statistical properties are entirely described by its mean and autocorrelation function. The random force (or noise, equivalently) introduced under these assumptions is called white Gaussian noise with zero mean, and will henceforth be referred to as $\xi(t)$. We can write the random force

$$F_R(t) = \sqrt{2\mathcal{D}_\xi} m\xi(t), \text{ with } \langle\xi(t)\rangle = 0 \text{ and } \langle\xi(t)\xi(t+s)\rangle = \delta(s). \tag{2.5}$$

An equation of motion including such a random force is also referred to as **Langevin equation** [94]. The strength of the random force scales with the noise intensity $\mathcal{D}_\xi$.

We now turn to the diffusive properties Brownian particle driven by white Gaussian noise $\xi(t)$. To that end, its Langevin equation (2.2) is multiplied with $x(t)$, which delivers an differential equation for $\langle x(t)v(t)\rangle$. It is solved by variation of constants, yielding

$$\frac{1}{2}\frac{\mathrm{d}}{\mathrm{d}t}\left\langle x^2(t)\right\rangle = \left\langle v^2(t)\right\rangle \left(1 - e^{-\frac{\gamma_0}{m}t}\right) \tag{2.6}$$

In thermal equilibrium, the equipartition theorem holds, meaning that each degree of freedom of the system has the same temperature dependent energy on average, $\langle v^2\rangle = k_B T/m$. Here, k_B denotes the Boltzmann constant and T the temperature. Integration after the time yields an expression for the **mean square displacement** (**MSD**)

$$\left\langle (x(t) - x_0)^2\right\rangle = \frac{2k_BT}{\gamma_0}\left(t - \frac{m}{\gamma_0}\left[1 - e^{-\frac{\gamma_0}{m}t}\right]\right), \tag{2.7}$$

By definition, the long time behavior of the MSD, i.e. for $t \gg \gamma_0/m$, is described by the time independent effective diffusion coefficient,

$$D_{\text{eff}} = \lim_{t\to\infty} \frac{\langle (x(t) - x_0)^2\rangle}{2t}. \tag{2.8}$$

For our Brownian particle, this leads to the first fluctuation dissipation theorem in its most basic form,

$$D_{\text{eff}} = \frac{k_BT}{\gamma_0}, \tag{2.9}$$

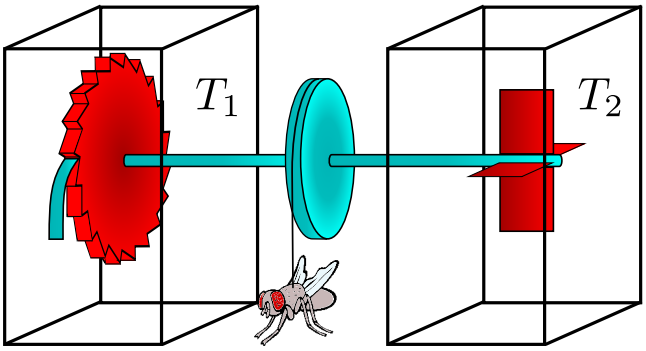

Figure 2.1.: The Feynman-Smoluchowski ratchet. A temperature difference of the heat baths of the paddlewheel (T_1) and the ratchet (T_2) can be used to lift the fruitfly against earth's gravitational pull, but only if $T_2 < T_1$.

one of the many famous Einstein relations. If we calculate the velocity variance from eq. (2.2) and compare it to the equipartition theorem for $t = 0$, the second fluctuation dissipation relation follows

$$\mathcal{D}_\xi = \gamma_0 k_B T. \tag{2.10}$$

For a free Brownian particle we obviously have $D_{\text{eff}} = \mathcal{D}_\xi \gamma_0^{-2}$.

2.3. The Feynman-Smoluchowski Ratchet

After having introduced the random thermal force, we ask ourselves if it can be used to harvest work? This brings us to the concept of the ratchet. Their notion was introduced in a Gedankenexperiment by Marian von Smoluchowski [168] in 1912 and later popularized by Richard Feynman in his famous lectures [44]. Ratchets are devices capable of rectifying unbiased fluctuations, thus leading to the possibility of directed transport. The archetypical ratchet consists of a paddle wheel connected by a solid rod to a ratchet, meaning a round gear with asymmetrical teeth. A springloaded finger called a pawl engages the teeth. Due to the asymmetry of the teeth the gear can only turn in one direction: in the forward direction, the pawl slides up over the gently sloped edges of the teeth, whereas in the backward direction the pawl is caught by the steeply sloped edge of the first tooth it encounters, thereby blocking any further motion. The paddlewheel is immersed in a gas or fluid with molecules of temperature T. Now, random collisions with the molecules will turn the wheel in both directions with equal probability. But as the pawl allows rotation in only one direction, the whole device is thought to theoretically constantly rotate in the forward direction. This could be used to extract work, for example by lifting a small fly against gravity. Such a device is depicted in figure 2.1.

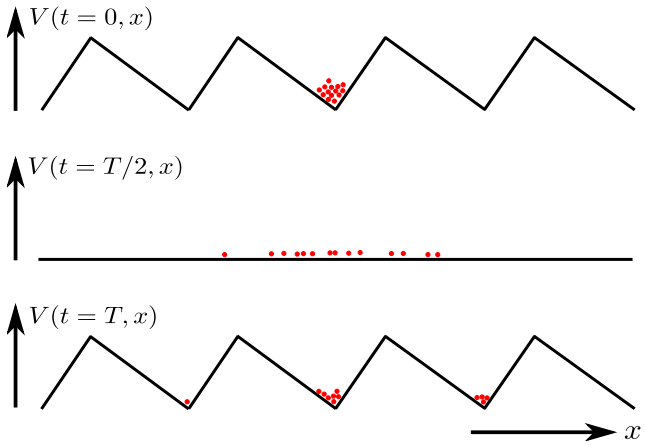

Figure 2.2.: Concept of a flashing ratchet. Brownian particles experience a periodic ratchet potential, that is switched on and off. During the on-phases, the particles are confined near the potential minima, while they diffuse freely in the off-phases. If the potential is switched back on after an off phase, the particles will slide to the next minimum in the direction of the potential slope; since more particles will fall onto the gentler sloped side of the potential landscape, a net transport in this direction occurs.

Obviously, gaining work of a single heat bath contradicts the second law of thermodynamics. Smoluchowski resolved this apparent paradox by arguing that the pawl holding back the ratchet must be thought of as microscopic and thus under the influence of noise as well[1]. Hence it releases the gear from time to time. If this coincides with a small backward rotation caused by the paddlewheel, the gear slides back. Effectively, the forward and backward rotation cancel each other out and no fly will leave the ground - unless it flaps its own wings.

In order to be able to do work, the ratchet and the paddlewheel must be connected to two different heat baths with temperatures T_2 and T_1. If the heat bath connected to the paddlewheel has a higher temperature (T_2) than that connected to the gear (T_1), i.e. $T_2 > T_1$, the instances of forward rotation induced by the paddlewheel outweigh the backward rotations with opened pawl, and the fly can be lifted. This motion is accompanied by a heat transport form the paddlewheels heat bath to the gear's heatbath. The upward motion of the fly must stop once both are equilibrated, $T_1 = T_2$. Although introduced as Gedankenexperiment, a device resembling its classical form has recently been constructed and investigated in a granular gas [40].

Another kind of ratchet, which bears more resemblence to the transport processes we are investigating in this work, is the **flashing ratchet** [1, 9, 31, 138]. Brownian

[1] The working principle of the pawl is quite similar to the valve controlled by Maxwell's demon. The valve connects two otherwise isolated boxes of gas, and allows only fast molecules to pass in the one direction and slow molecules to pass in the other.

particles perform a diffusive motion, and further experience a periodic potential landscape $V(x,t)$ that is switched on and off. While the ratchet potential is on, the particles are concentrated close to the minima. Once switched off, they perform a free diffusive motion on the plane and spread spatially. Turning it back on, the particles will again be located in the potential minima. However, a substantial number of particles has travelled so far that it settles into the next minimum, while a much smaller number falls into the previous minumum. This way, a net particle flux is realized. With the right choice of parameters, transport can even be obtained with a constant force acting against the desired direction of transport. Obviously, the thermodynamic equilibrium is broken by switching on the potential, which then transfers energy to the particles. A flashing ratchet is shown in Fig. 2.2.

More generally, the term ratchet refers to nonequilibrium phenomena that can arise provided all space-time symmetries which inhibit directed motion are broken [45]. This can be caused either explicitly by an asymmetric, periodic structure or by an unbiased, but asymmetric drive [59].

Nowadays, ratchet model are employed to explain a wide range of transport phenomena. Arguably the most prominent applications occur in biophysics, for example the description of molecular motors along the cytoskeleton [5, 79]. Such systems will be investigated in part II. Therein, we also introduce chemically driven conformation ratchets. They will link the stochastic motion of a Brownian particle to the discrete hopping processes of the molecular motors, and closely resemble the flashing ratchet discussed in this section.

2.4. Biased Motion in Dynamical Systems

Another example for biased transport occurs in a modification of so called Sinai billiards [166]. Billiards are dynamical systems where particles alternate between motion in straight lines and specular reflections (meaning mirror-like, the angle of incidence equals the angle of reflection) at the boundaries. In a Sinai billiard, a disk is removed from the center, leading to another boundary at which particles are reflected. Such a system shows thermodynamic behavior, its physical counterpart is the Lorenz gas.

This setup was modified and studied with regard to transport properties by H. Schanz and M. Prusty [139, 156]. They considered electrons in a confining channel periodic in the x-direction. The upper wall was even, whereas from the lower wall disks with varying radii were removed, cf. figure 2.3. Also, the electrons were subjected to a magnetic field perpendicular to the image plane, hence their trajectories possess a constant curvature depending on the field strength.

In this setup the electrons either had deterministic quasi-periodic or chaotic trajectories where backscattering takes place, depending on their initial conditions. Both types of motion lie in distinct areas of phase space. While the regular orbits transport continuously in one direction, the chaotic orbits transport in the opposite

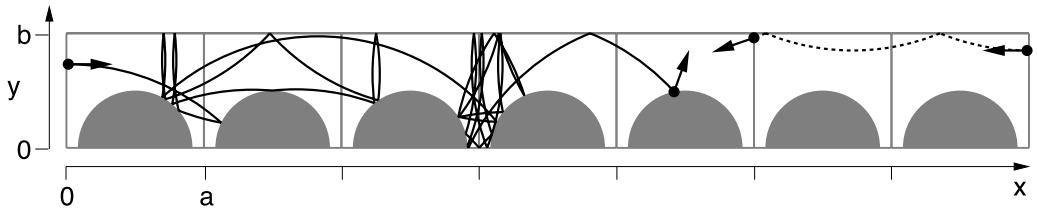

Figure 2.3.: Setup directed chaos from [156]. The dotted line represents a quasi-periodic motion, the particle bounces of the upper boundary repeatedly without ever reaching the grey discs. The solid line shows a chaotic trajectory.

direction. They exhibit a diffusive behavior with an additional drift, whose exact rates depend on the geometric setup and the field strength. For an equilibrium ensemble, both transports compensate each other on average, leading to an unbiased system.

Summary

In this chapter we have introduced the basic concepts of Brownian motion, and how their noisy trajectories are treated mathematically within the framework of stochastic differential equations. Further, we introduced the notion of ratchets; machines that can rectify unbiased noisy motion outside of equilibrium, given that spatio-temporal symmetries are broken. In the following chapter, we will apply these concepts to the transport of active Brownian particles confined to a channel geometry that is resembling the Sinai billiard. We will revisit these concepts in the other parts of this thesis as well.

3. Persistent Motion and Transport of Brownian Particles with Torque

The diffusive motion of Brownian particles is unbiased in its nature. In order to speak of transport, the isotropy of their motion must be broken, so that a sense of direction is introduced. The question arises, if we can engineer an environment in such a way, that the undirected fluctuations driving the Brownian particle lead to a directed motion. To this end we will investigate the persistent motion of Brownian particles driven by a correlated noise, which is modeled by the Ornstein-Uhlenbeck process. An additional constant torque leads to circular trajectories, as they can be observed for ions, plasmas in magnetic fields, as well as for many artificial systems and biological agents. The particles are considered first as driven by noise in thermal equilibrium and second with a noisy propulsion in nonequilibrium. We will calculate the systems' free diffusional dynamics and simulate its behavior in a variable tunnel geometry that is resembling the Sinai billiards. In the nonequilibrium process, a directed transport emerges, its properties are studied in detail with respect to the correlation time, the torque, and the channel geometry. Eventually, the transport mechanism is traced back to a persistent sliding of particles along the smooth boundaries in contrast to scattered motion at uneven or rough ones.

3.1. Introduction

Instead of the white noise drive covered in the introduction 2.2, we now consider particles driven by a time correlated Gaussian noise, namely an **Ornstein-Uhlenbeck process** (**OUP**) [63–65, 68, 69, 112, 127, 178]. Such a correlation of the motion appears, if the time scale of subsequent pushes of the random force cannot be neglected against the other internal time scales of the system. The OUP drive leads to a persistent motion that can be realized both for systems in and outside of thermal equilibrium. In the former case, we generally think of charged particles in a gaseous environment, in the latter, of biological or artificial microswimmers.

Further, the particles are subjected to a torque, leading to a circular motion and an alteration of the diffusive properties [61, 185, 186]. For Brownian particles such motion appears in many real world phenomena, for example in gases of charged particles [165] or plasmas [93, 106], as well as in heavy ions [74, 75, 127, 165], for all of which it is caused by a uniform magnetostatic field. A circular motion appears for microswimmers as well, active Brownian particles [147] that can be produced

artificially or be biological agents. Examples of artificial systems include nanorods [118, 161] and Janus particles [4, 105] swimming in a water peroxide solution, in which they are catalyzing a chemical reaction used for their propulsion. The torques induced by an external magnetic field can be used to steer the nanorods [85], for Janus particles laser irradiation leads to the same effect [73]. Alternatively the circular motion appears due to an asymmetry in their geometry, which is e.g. the case for L-shaped nanorods [62, 92]. A circular motion for biological agents appears due to asymmetries in the propulsion itself as occurring in the chemotaxis of sperm cells [46, 47, 181], or due to interaction with other agents, leading to the formation of vortices around which the agents are swarming [23, 24, 81]. In the cases of active Brownian particles, the agents have an internal energy supply.

We want to investigate a channel geometry of varying width results in the directed transport of confined Brownian particles. In a setup resembling the Sinai-billiard of section 2.4, the particles are confined to an infinitely long channel with a periodically varying width. One of the channel walls is introduced as a reflecting disk. Later on, it will be interchanged by a reflecting triangle, thereby adding another symmetry breaking. When a particle hits one of these walls, specular reflections take place, this means that the angle of reflection is equal to the angle of incidence. Finally, we also consider a 'rough' lower wall where elastic scattering is modeled by equidistributed reflection angles, regardless of the angle of incidence. The different realizations of the tunnel are depicted in Fig. 3.1 together with some sample trajectories of the particles. In the recent years, various other geometrical setups for directed transport have been studied, either for corrugated walls in the Ficks-Jacob approximation with an external forcing [114, 115], for microswimmers in ratchet like hard repulsion potentials [4, 103, 105] or for the transport along obstacles [54, 159].

In our case, the symmetry breaking is realized by a nonvanishing mean torque together with the confining geometry. We are interested in realizing a ratchet mechanism to rectify the unbiased diffusive motion of our Brownian agents and achieve directed transport. To that end, we also introduce the driving by a correlated noise. The correlated noise is realized with a memory kernel for the equilibrium processes in section 3.2, and without a fluctuation-dissipation theorem for active microswimmers outside of equilibrium in section 3.3. In the latter case, we will observe the emergence of directed transport, which is investigated in detail and explained phenomenologically.

3.2. Persistent Motion of Brownian Particles in Thermal Equilibrium

We consider our Brownian particle in two dimensional space, with the position $\boldsymbol{r}(t) = (x(t), y(t))$ and velocity $\dot{\boldsymbol{r}}(t) = \boldsymbol{v}(t) = (v_x(t), v_y(t))$ at time t. It is driven by correlated noise $\boldsymbol{\varepsilon}(t) = (\varepsilon_x(t), \varepsilon_y(t))$ in thermal equilibrium and has unit mass

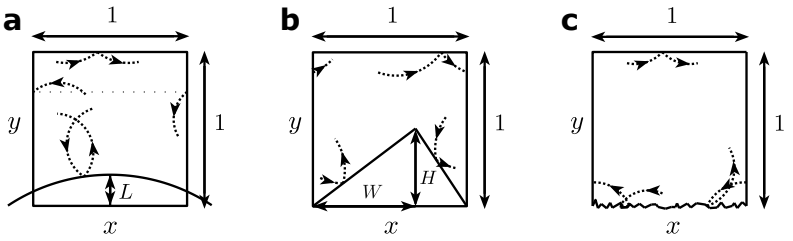

Figure 3.1.: Illustration of the channel geometry, a box of unit size whose left and right side are oriented at one another, realizing periodic boundary conditions. At the top and bottom specular reflections take place. **a** shows a lower boundary formed by a disc of radius $R = 1.2$ that protrudes by $L = 0.2$ into the box. **b** shows an edged boundary parameterized by $H = 0.5$ and $W = 2/3$. **c** A flat lower boundary with equidistributed scattering angles due to a 'rough' surface.

$m = 1$.

Uncorrelated white noise is an idealization, valid if the correlation time τ_c of the random force is small against other characteristic time scales of the system. Foremost, it must be compared to the friction function that determines how fast the inertia of our particle dissipates, which will largely depend on the viscosity of the fluid it is immersed in. In case of similar time scales of both, we say that subsequent pushes of the random force are exponentially correlated

$$\langle \varepsilon_i(s)\varepsilon_j(s+t)\rangle = \frac{\mathcal{D}_\xi}{\tau_c} e^{-|t|/\tau_c}\delta_{ij}, \tag{3.1}$$

whose individual components in x and y direction are independent. eq. (3.1) represents the Ornstein-Uhlenbeck process (OUP), it is the most natural continuous valued colored noise [64]. The term colored refers to its spectral density of the random force, which becomes a function of the angular frequency ω. It is given by a Lorentzian with the width $\omega_c = 2\pi/\tau_c$

$$S_{\varepsilon_i\varepsilon_j}(\omega) = 2D_\xi \frac{\omega_c^2}{\omega^2 + \omega_c^2}\delta_{ij}. \tag{3.2}$$

In analogy to visible light, the terms white and colored become obvious. White light is composed of all colors, hence a flat spectrum is called white noise (in case of eq. (3.2) it follows for vanishing correlation time $\tau_c = 0$), whereas if one contribution outweighs the others, its color changes. Specifically, eq. (3.2) is referred to as red noise, because lower frequencies are enhanced while higher frequencies are suppressed.

In thermal equilibrium, the friction and the noise have the same origin, random collisions with the particles of the immersing fluid. A fluctuation dissipation theorem relates the autocorrelation function of the noise and the friction function

$$\langle \varepsilon_i(t)\varepsilon_j(s)\rangle = k_B T\gamma(|t-s|)\delta_{ij}, \tag{3.3}$$

Here, the Einstein relation (2.10), $\mathcal{D}_\xi = \gamma_0 k_B T$, was used to relate the noise intensity $\mathcal{D}_\xi$ to the heat bath. Assuming that a FDR holds, we are forced to relinquish the Markov property by introducing a dissipative memory kernel $\gamma(|t-s|)$ to govern the friction. We then speak of a generalized Langevin equation [119, 127] for the velocity,

$$\dot{\boldsymbol{v}}(t) = -\int_0^t \gamma(|t-s|)\boldsymbol{v}(s)\mathrm{d}s + \boldsymbol{\varepsilon}(t) + \bar{\boldsymbol{\Omega}}\boldsymbol{v}(t). \tag{3.4}$$

The additional mean torque is realized by multiplication of $\boldsymbol{v}$ with the rotation matrix $\bar{\boldsymbol{\Omega}}$, resulting in the force

$$\bar{\boldsymbol{\Omega}}\boldsymbol{v} = \begin{pmatrix} \Omega v_y \\ -\Omega v_x \end{pmatrix}. \tag{3.5}$$

In order to reformulate the equations of motion in a Markovian frame, we equate (3.1) and (3.3) and introduce the integral term in eq. (3.4) as an auxiliary variable $\boldsymbol{\chi}(t)$,

$$\boldsymbol{\chi}(t) = \frac{\gamma}{\tau_c}\int_0^t e^{-(t-s)/\tau_c}\boldsymbol{v}(s)\mathrm{d}s. \tag{3.6}$$

Our system is then governed by the set of equations

$$\begin{aligned} \dot{\boldsymbol{r}}(t) &= \boldsymbol{v}, & \dot{\boldsymbol{v}}(t) &= -\boldsymbol{\chi} + \boldsymbol{\varepsilon} + \bar{\boldsymbol{\Omega}}\boldsymbol{v}, \\ \dot{\boldsymbol{\chi}}(t) &= -\frac{1}{\tau_c}\boldsymbol{\chi} + \frac{\gamma}{\tau_c}\boldsymbol{v}, & \dot{\boldsymbol{\varepsilon}}(t) &= -\frac{1}{\tau_c}\boldsymbol{\varepsilon} + \frac{\sqrt{2\mathcal{D}_\xi}}{\tau_c}\boldsymbol{\xi}(t). \end{aligned} \tag{3.7}$$

As before, $\boldsymbol{\xi}(t)$ denotes white Gaussian noise of zero mean and unit variance, ergo $\langle \xi_i(t)\xi_j(s)\rangle = \delta_{ij}\delta(t-s)$ and $\langle \xi_i(t)\rangle = 0$. We can easily see that the equation for $\dot{\boldsymbol{\chi}}$ follows from (3.6) through time differentiation. The identification of $\dot{\boldsymbol{\varepsilon}}$ with its autocorrelation function (3.1) follows from application of the Green-Kubo relation [90].

In the equations of motion (3.7), the linear combination of $\chi(t)$ and $\epsilon(t)$ appears twice. By subtracting their respective equations of motion $\boldsymbol{\eta}(t) := -\boldsymbol{\chi} + \boldsymbol{\varepsilon}$, we find a set of six coupled differential equations that is modeling the persistent motion of Brownian particles in thermal equilibrium,

$$\begin{aligned} \dot{\boldsymbol{r}}(t) &= \boldsymbol{v}, \qquad \dot{\boldsymbol{v}}(t) = \boldsymbol{\eta} + \bar{\boldsymbol{\Omega}}\boldsymbol{v}, \\ \dot{\boldsymbol{\eta}}(t) &= -\frac{1}{\tau_c}\boldsymbol{\eta} - \frac{\gamma}{\tau_c}\boldsymbol{v} + \frac{\sqrt{2D}}{\tau_c}\boldsymbol{\xi}(t). \end{aligned} \tag{3.8}$$

In Fig. 3.2.**a**, several trajectories are shown for various lengths of the correlation time[1]. We see that a longer correlation of the noise smoothens the paths and leads to a more prominent impact of the mean torque, a very distinct circular motion

[1] The equations of the Langevin dynamics are iterated using a stochastic Heun algorithm, which proves effective for both white and colored noise [113]. The Heun method is equivalent to the Runge-Kutta method of second order with symmetrical sampling points.

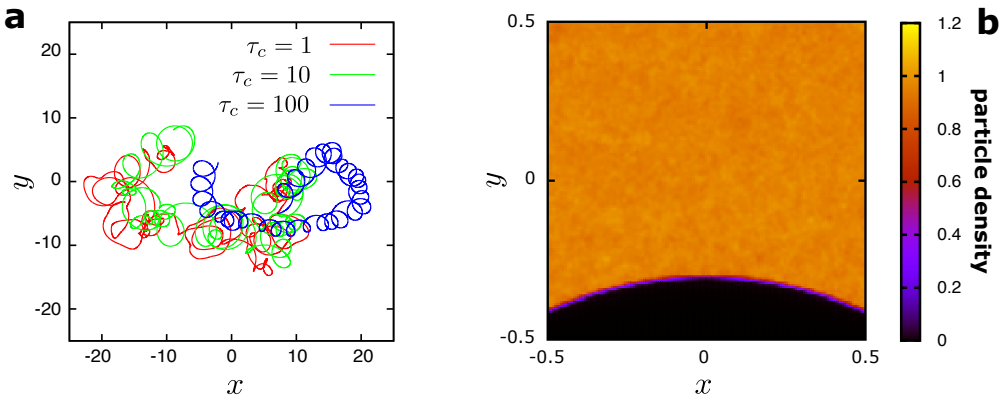

Figure 3.2.: a Trajectories of particles exposed to colored noise in equilibrium for several correlation times at constant $\gamma = 0.2$, $\mathcal{D}_\xi = 0.04$, $\Omega = 0.3$. The particles are driven by an identical realization of the noise $\boldsymbol{\xi}(t)$ for a displayed time length is $t_l = 600$. **b** Corresponding density plot for the confinement specified in Fig. 3.1.**a**. A uniform density is obtained regardless of the set of parameters.

is now superimposed on the overall large scale trajectory. The radii of the circles is determined by the cyclotron radius (or equivalently Larmor radius) R_c, which is obtained by equating the Lorentz force (which causes the mean torque) and the centrifugal force that are acting on a particle,

$$R_c = \frac{v}{\Omega}. \tag{3.9}$$

Obviously, the value of R_c varies with the speed. Meanwhile, the spatial displacement and the mean speed barely differ for different correlation times. Fig. 3.2.**b** displays the two dimensional particle density distribution for particles confined in the geometry given by Fig. 3.1.**a**. Besides small statistical fluctuations, the density is uniform regardless of the application of an additional constant torque Ω or the choice of the other parameters, as we expect for an equilibrium situation.

3.2.1. Fokker-Planck Equation and its Stationary Free Solution

Instead of supplementing individual particles with a random force that obeys specified statistical properties, we can consider the behavior of a particle ensemble. Its behavior is described by a partial differential equation for the probability density, namely the **Fokker-Planck equation** (**FPE**). We will briefly describe the connection between the FPE and its corresponding set of Langevin equations, and then formulate the FPE that follows in this framework from the equations of motion (3.8).

Via a so called Kramers Moyal expansion [146] of the transition probability we obtain the moments of our distribution, also called kinetic coefficients. For a Gaussian process, all moments except the first and second vanish. The remaining are defined

as follows

$$K_1(v,t) = \lim_{\Delta t\to 0} \frac{\langle \Delta v(t)\rangle}{\Delta t}, \qquad K_2(v,t) = \lim_{\Delta t\to 0} \frac{\langle (\Delta v(t))\rangle^2}{2\Delta t}. \tag{3.10}$$

With their help the FPE is written

$$\frac{\partial}{\partial t}P(v,t;v_0,t_0) = \left(\frac{\partial}{\partial v}K_1(v,t) + \frac{\partial^2}{\partial v^2}K_2(v,t)\right)P(v,t;v_0,t_0). \tag{3.11}$$

The first term on the right hand side denotes the drift, i.e. the force due to the negative gradient of a potential, and the second denotes the diffusion. The probability at point (v,t) is given in dependence of the initial velocity and time (v_0,t_0). According to the Kolmogorov axiom for conditional probabilities, $P(v,t;v_0,t_0) = P(v,t|v_0,t_0)P(v_0,t_0)$, eq. (3.11) holds for the conditional probability as well. Further assuming a Markovian, i.e. memoryless, process, the initial values of the system are forgotten and P depends on (v,t) only. White noise meets this criterion.

The probability is normalized to

$$\int_{-\infty}^{\infty} P(v,t)\mathrm{d}v = 1. \tag{3.12}$$

Now, with the Langevin equation (2.2) the kinetic coefficients can be calculated and inserted into eq. (3.11), yielding

$$\frac{\partial}{\partial t}P(v,t) = \left(\frac{\partial}{\partial v}\gamma v + \frac{\partial^2}{\partial v^2}\mathcal{D}_\xi\right)P(v,t), \tag{3.13}$$

the Fokker-Planck equation of a free Brownian particle in one dimension. The approach for a multi dimensional system is identical and results in a FPE equation in several variables [146].

Applying this mechanism to the persistent Brownian particle described by the equations of motion (3.8) requires calculating additional kinetic coefficients in η and those mixed in v and η. One obtains the Fokker-Planck equation

$$\frac{\partial P(\boldsymbol{r},\boldsymbol{v},\boldsymbol{\eta},t)}{\partial t} = -\frac{\partial}{\partial \boldsymbol{r}}(\boldsymbol{v}P) - \frac{\partial}{\partial \boldsymbol{v}}\left(\bar{\boldsymbol{\Omega}}\boldsymbol{v} + \boldsymbol{\eta}\right)P + \frac{1}{\tau_c}\frac{\partial}{\partial \boldsymbol{\eta}}\left(\boldsymbol{\eta} + \gamma\boldsymbol{v}\right)P + \frac{\mathcal{D}_\xi}{\tau_c^2}\frac{\partial^2}{\partial \boldsymbol{\eta}^2}P. \tag{3.14}$$

We want to solve the FPE (3.14) in the stationary, free case, for which the probability P^0 no longer depends on $\boldsymbol{r}$ and t. To this end, our Ansatz for the probability density is the summation of the weighted correlation functions

$$P^0(\boldsymbol{v},\boldsymbol{\eta}) = Z^{-1}\exp\left(-\frac{1}{\mathcal{D}_\xi}\sum_{i,j}c_{ij}q_iq_j\right), \qquad q_i,q_j \in \{v_x,v_y,\eta_x,\eta_y\}. \tag{3.15}$$

Here, Z denotes the normalization constant. The weighting parameters c_{ij} are determined by inserting $P^0(\boldsymbol{v}, \boldsymbol{\eta})$ into the FPE. This gives a set of equations for the weights that is successively solved. Performing this delivers

$$P^0(\boldsymbol{v}, \boldsymbol{\eta}) = \frac{\gamma\tau_c}{4\pi^2\mathcal{D}_\xi^2} \exp\left(-\frac{1}{2\mathcal{D}_\xi}\left(\gamma\boldsymbol{v}^2 + \tau_c\boldsymbol{\eta}^2\right)\right). \tag{3.16}$$

Obviously, the stationary distribution is not altered by the magnetic field. We can eliminate the dependence on η_x, η_y via integration over these variables, further integration over v_j with $i \neq j$ delivers a one dimensional Gaussian velocity distribution

$$P^0(v_i) = \sqrt{\frac{\gamma}{2\pi\mathcal{D}_\xi}} \exp\left(-\frac{\gamma}{2\mathcal{D}_\xi}v_i^2\right), \quad i \in \{x, y\}. \tag{3.17}$$

It depends only on a single parameter, the ratios of the noise intensity and the friction coefficient, γ/D_ξ. For the speed, i.e. the absolute value of the velocity $|\boldsymbol{v}|$, a Maxwell-Boltzmann distribution follows from eq. (3.17).

Velocity distributions obtained from numerical simulations are depicted in Fig. 3.3.**a**, and compared to the analytical result eq. (3.17) in perfect agreement. This remains true, if the particles are confined in either of the tunnel geometries. Thus, the system of Langevin equations (3.8) indeed describes an equilibrium with the heat bath, neither the torque nor the correlation time has any influence on the stationary properties. Further, this means that the velocity distribution remains symmetrical in the confinement. This holds true both globally for the entire confinement and in the vicinity of the boundaries. Hence, no directed transport can emerge for particles driven by thermal noise.

Effective Diffusion Coefficient

In the following, we want to determine the diffusive properties within and outside the channel confinement for our system with correlated noise in equilibrium. We would assume, that the diffusive properties for large time scales are similar to those for a particles driven by white noise in equilibrium, and indeed this is what was already found out by [127]. We will shortly summarize their approach and state the result. First, the Laplace transformation of eq. (3.4) is taken and solved for the Laplace transformed velocity. This expression must then be examined for its parameter dependent poles and its Laplacian inverse can be taken by integration over the complex plane according to those poles. With the resulting term for the velocity, we can write down its velocity autocorrelation function, from which by integration over time in the large time limit the effective diffusion coefficient follows,

$$D_{\text{eff}} = \frac{\mathcal{D}_\xi}{\gamma^2 + \Omega^2}. \tag{3.18}$$

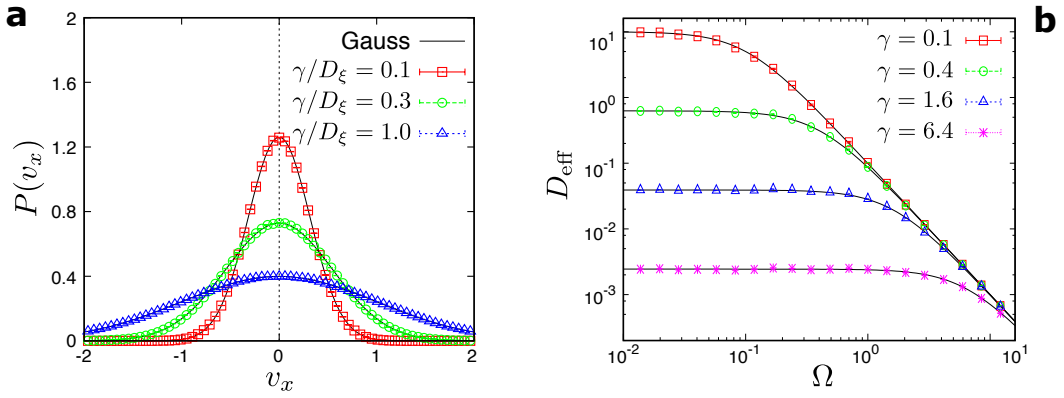

Figure 3.3.: a Velocity distribution for a particle driven by thermal colored noise for several parameters $\mathcal{D}_\xi/\gamma$, simulation (colored symbols) versus theory (black lines; cf. equation (3.17) in perfect agreement. The simulations were performed for several mean torques Ω, in free space and with boundaries, and for various $\mathcal{D}_\xi$, γ at a fixed ratio, none of which alters the result. **b** Effective diffusion coefficient in free space as a function of the mean torque for different friction coefficients at $D_\xi = 0.1$, cf. eq. (3.18). Simulations performed for various correlation times τ_c, yielding the same curves.

It does obviously not depend on the correlation time and is identical to the effective diffusion coefficient for particles driven by white Gaussian noise, since the correlation time does not appear. It is depicted in Fig. 3.3.**b**, which we have validated numerically for nonvanishing correlation times. The trajectories in Fig. 3.2 already hinted at this result, with no visible variation in the spatial spread for the various τ_c.

3.3. Persistent Motion of Active Particles

In the second case we consider noisy propulsion in nonequilibrium. Our Brownian particle is again equipped with an additional torque and a correlated OUP-drive. Confined to the tunnel, in the non-thermal process a directed transport emerges.

The autocorrelation function of the noise is given by eq. (3.2) again, but unlike in the case for the thermal colored driving we require no FDT to hold and replace the memory kernel eq. (3.4) by a delta distribution. The system is then governed by the set of Langevin equations

$$\begin{aligned} \dot{\boldsymbol{r}}(t) =& \boldsymbol{v}(t), \qquad \dot{\boldsymbol{v}}(t) = -\gamma_0 \boldsymbol{v}(t) + \bar{\boldsymbol{\Omega}}\boldsymbol{v}(t) + \boldsymbol{\epsilon}(t), \\ & \dot{\boldsymbol{\epsilon}}(t) = -\frac{1}{\tau_c}\boldsymbol{\epsilon}(t) + \frac{\sqrt{2\mathcal{D}_\xi}}{\tau_c}\boldsymbol{\xi}(t). \end{aligned} \tag{3.19}$$

Again, $\boldsymbol{\xi}(t)$ denotes white Gaussian noise of zero mean with uncorrelated components, i.e. $\langle \xi_i(t) \rangle = 0$ and $\langle \xi_i(s)\xi_j(s+t) \rangle = \delta(t)\delta_{ij}$.

In this way, we have effectively realized the motion of an active particle. The correlated OUP noise supplies a permanent flux of energy, which then dissipates during the persistent and curved motion due to Stokes friction. The persistence of this motion expresses the nonequilibrium. With $\tau_c \to 0$ white noise follows realizing again an equilibrium situation.

3.3.1. Diffusion

In the following, we want to derive the effective diffusion coefficient for our process driven by colored noise outside of equilibrium. To this end, we will first derive the time dependent velocity autocorrelation with the help of the Wiener-Khintchine theorem, which relates the spectrum and the autocorrelation function of a stationary process as a Fourier pair. Its spectrum can then be traced back to the Lorentzian spectrum of the noise eq. (3.2). With the velocity autocorrelation function, the diffusion coefficient then follows by time integration. Second, we will numerically verify this result and compare it the diffusive displacement in the confined geometry.

We start by considering the Fourier images of the the equations of motion (3.19), the respective transforms are indicated by an additional ω-subscript. Solving for $v_{x\omega}$ and $v_{y\omega}$ yields

$$v_{x\omega} = \frac{F_{x\omega}(i\omega - \gamma_0) + F_{y\omega}\Omega}{(i\omega - \gamma_0)^2 + \Omega^2}, \qquad v_{y\omega} = \frac{F_{y\omega}(i\omega - \gamma_0) - F_{x\omega}\Omega}{(i\omega - \gamma_0)^2 + \Omega^2}. \tag{3.20}$$

According to the Wiener-Khintchine theorem [83, 188], the autocorrelation function and the spectral density of a stationary process form a Fourier transform pair, i.e.

$$\langle v(s)v(s+t)\rangle = c_{vv}(t) = \frac{1}{2\pi}\int_{-\infty}^{\infty} S_{vv}(\omega)e^{i\omega t}\mathrm{d}\omega. \tag{3.21}$$

With the spectra of v and F_R, defined as

$$S_{vv}(\omega) = \lim_{T\to\infty}\frac{1}{T}\left\langle |v_\omega|^2\right\rangle, \qquad S_{FF}(\omega) = \lim_{T\to\infty}\frac{1}{T}\left\langle |F_\omega|^2\right\rangle, \tag{3.22}$$

we can express $c_{vv}(t)$ in terms of the known noise spectrum. Thus we need to calculate $|v_{x\omega}|^2$. It yields

$$|v_{x\omega}|^2 = \frac{|F_{x\omega}|^2(\omega^2+\gamma_0^2) + |F_{y\omega}|^2\Omega^2 + 2\,\mathbb{R}\mathrm{e}(F_{x\omega}\overline{F}_{y\omega})\gamma_0\Omega + 2\,\mathbb{I}\mathrm{m}(F_{x\omega}\overline{F}_{y\omega})\omega\Omega}{(\gamma_0^2+\Omega^2-\omega^2)^2 + 4\omega^2\gamma_0^2}, \tag{3.23}$$

with $\mathbb{R}\mathrm{e}$ denoting the real and $\mathbb{I}\mathrm{m}$ the imaginary part, the bar indicates the complex conjugate. Analogously, we obtain $|v_{y\omega}|^2$ by interchanging x and y.

Since the random forces F_x and F_y are statistically independent, their Fourier transforms are uncorrelated as well. Also $\boldsymbol{F_R}$ is unbiased, negative and positive fluctuations are equally likely, and thus its average is zero. Due to these properties,

the mixed terms in eq. (3.23) vanish: $\left\langle F_{x\omega}\overline{F}_{y\omega}\right\rangle = \left\langle F_{x\omega}\right\rangle\left\langle \overline{F}_{y\omega}\right\rangle = 0$. Hence we obtain the velocity spectrum

$$S_{v_iv_i}(\omega) = \frac{\omega^2+\gamma_0^2+\Omega^2}{(\gamma_0^2+\Omega^2-\omega^2)^2+4\omega^2\gamma_0^2}S_{FF}(\omega), \qquad i\in\{x,y\}, \tag{3.24}$$

with the Lorentzian for the colored noise given by eq. (3.2). Evidently, the velocity spectrum is identical for the x- and y-direction.

Finally, we insert this result into the Wiener-Khintchine theorem (3.21) and perform the integration to obtain an expression for the velocity autocorrelation function,

$$\begin{aligned} c_{v_iv_i}(t) =& \frac{\mathcal{D}_\xi\omega_c}{\gamma_0\left(\gamma_0^4-2\gamma_0^2(\omega_c^2-\Omega^2)+(\omega_c^2+\Omega^2)^2\right)}\Big[e^{-|t|\omega_c}\gamma_0(\gamma_0^2-\omega_c^2+\Omega^2) \\ &+ e^{-|t|\gamma_0}\omega_c\Big(\cos(|t|\Omega)\left(-\gamma_0^2+\omega_c^2+\Omega^2\right)+\sin(|t|\Omega)2\gamma_0\Omega\Big)\Big]. \end{aligned} \tag{3.25}$$

Eq. (3.25) shows a complex transient oscillating behavior. To elucidate its behavior a little further, and because we are mainly interested in time independent properties anyway, we can look at the mean square velocity by setting $t=0$, yielding

$$\left\langle v_i^2\right\rangle = \frac{\mathcal{D}_\xi\omega_c}{\gamma_0}\frac{\gamma_0+\omega_c}{(\gamma_0+\omega_c)^2+\Omega^2}. \tag{3.26}$$

Obviously, the magnetic field and the friction dampen the particles mean square velocity. The behavior due to the correlation time is more complex. For a vanishing mean torque, i.e. $\Omega=0$, this reproduces the known formula for c_{vv} without external force field [136].

As the next step, we want to use the velocity autocorrelation function (3.25) to determine the diffusion of the free system. The definition of D_{eff} was given in eq. (2.8). In the limit a large times $t\to\infty$ and for small observation windows $\Delta t\to 0$ we can interpret the expression therein, $\left\langle\Delta x^2\right\rangle/\Delta t$, as a time derivative $2xdx/dt$. With the initial condition $x(t=0)=0$ we obtain

$$\begin{aligned} &\frac{\mathrm{d}}{\mathrm{d}t}\frac{\left\langle x^2(t)\right\rangle}{2} = \langle x(t)v_x(t)\rangle = \int_0^t \langle v_x(s)\,v_x(t)\rangle\,\mathrm{d}s \\ &= \frac{\mathcal{D}_\xi}{\gamma_0^2+\Omega^2} + e^{-t\omega_c}\frac{\mathcal{D}_\xi\left(\gamma_0^2-\omega_c^2+\Omega^2\right)}{\gamma_0^4-2\gamma_0^2\left(\omega_c^2-\Omega^2\right)+\left(\omega_c^2+\Omega^2\right)^2} \\ &+ e^{-t\gamma_0}\frac{\mathcal{D}_\xi\omega_c^2\Big[\cos(\Omega t)\gamma_0\left(\gamma_0^2-\omega_c^2-3\Omega^2\right)+\sin(\Omega t)\Omega\left(-3\gamma_0^2+\omega_c^2+\Omega^2\right)\Big]}{\gamma_0\left(\gamma_0^2+\Omega^2\right)\left(\gamma_0^4-2\gamma_0^2\left(\omega_c^2-\Omega^2\right)+\left(\omega_c^2+\Omega^2\right)^2\right)}. \end{aligned} \tag{3.27}$$

Since we only investigate the effective diffusion coefficients in this work, we will not further discuss this result. It should have an interesting regime dependent crossover

structure from ballistic to diffusive motion, that could be given further attention, analogously to similar studies for other dynamics [134, 185]. In the limit of large times $t \to \infty$ all except the first term vanish, resulting in the expression for the effective diffusion coefficient

$$D_{\text{eff}} = \frac{\mathcal{D}_\xi}{\gamma_0^2 + \Omega^2}. \tag{3.28}$$

The same result was obtained for particles driven by colored noise in thermal equilibrium eq. (3.18), where we discussed and plotted its behavior in Fig. 3.3.**b**.

3.3.2. Directed Transport in Confined Geometries

Fig. 3.4 depicts some trajectories in the circular channel for the non-thermal dynamics given by eq. (3.19). Rising correlation times lead to a reduction of the total spatial displacements as do increasing mean torques, although less severely. With both influences acting on the particles together another effect can be observed: the particles stay in the vicinity of the reflecting boundaries for a longer time and perform a curly hopping motion that changes to a narrow creeping for large τ_c. We remark that a sliding along the channel walls has also been studied in [181, 187] and observed experimentally in [33]. While the red trajectory (empty arrowheads) is largely unbiased, with bigger torques the particles travel a longer distance along the flat wall than along the curved wall.

This sticking to the walls is confirmed in the density plots, depicted in Fig. 3.5 with and without an additional constant torque. In case of $\Omega = 0$, the particles spent more time close to the boundaries of the domain, however, there is no left-right symmetry breaking as expected. In case With an additional constant torque, they spent markedly more time close to the boundaries. Also, there is a breaking of the left-right symmetry in their occupation probability.

The velocity distributions for the same situation are depicted in Fig. 3.6 [113]. While the velocity is Gaussian distributed for $\tau_c = 0$, it remains symmetrical on an unbounded plane or in the confined geometry without constant torque. In contrast, if all these influences act on the particles together, i.e. boundaries, finite correlation time and constant torque field, the velocity distribution loses its symmetry (green circles). For $\Omega = 1$, the v_x-distribution's left tail is lowered, while its right tail is raised. Thus, we have a net particle flux. Unlike for particles in equilibrium, the velocity distributions are narrowing with growing $|\Omega|$. Furthermore, we notice that the confinement particularly leads to a narrowing in $P(v_y)$, which now markedly differs from $P(v_x)$.

Let us now address the net stationary particle fluxes J that pass in the x-direction through our channel. Hereby, J is normalized with respect to the number of particles.

The numerical results for the net transport are shown in Fig. 3.7 as a function of the correlation time for several values of the mean torque. J has a maximum at approximately $\tau_c \approx 2 - 3$ for all depicted Ω values. For vanishing correlation times,

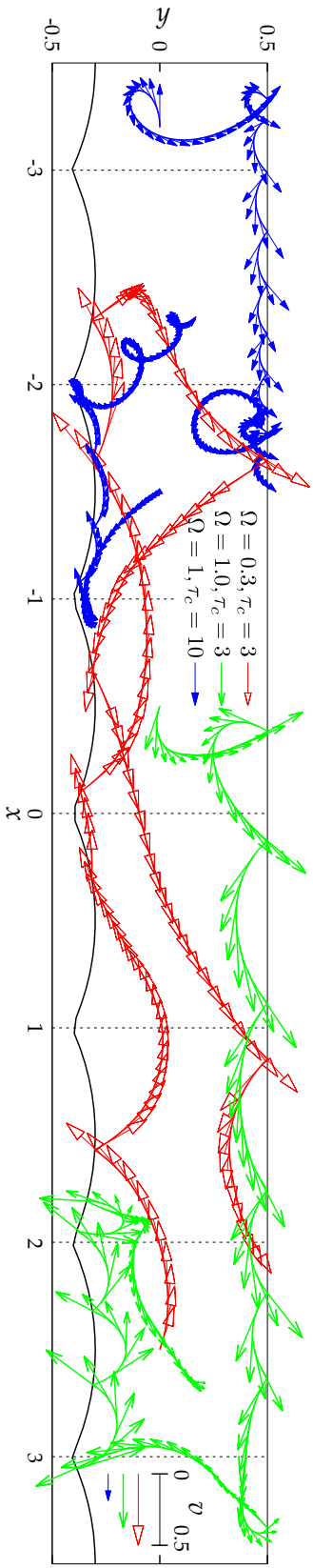

Figure 3.4.: (Color online) Trajectories of confined (cf. Fig. 3.1 (a)) particles exposed to non-thermal colored noise with several torques and correlation times at constant $\gamma_0 = 0.2$, $\mathcal{D}_\xi = 0.04$. The depicted time length is $t_l = 33$, the velocity is indicated by the arrows, between two consecutive arrows $\Delta t = 1/4$ has passed.

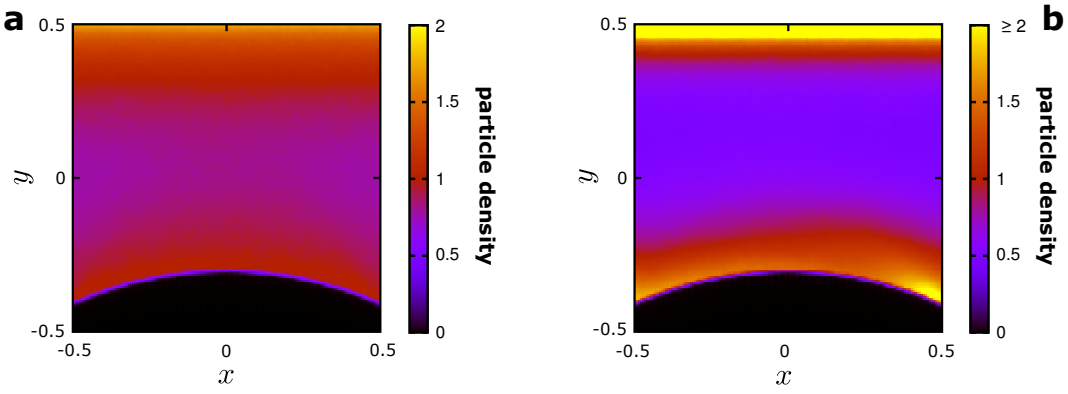

Figure 3.5.: Density plot for particle driven by colored noise outside of equilibrium. All curves are at $\gamma_0 = 0.2$, $\mathcal{D}_\xi = 0.04$ and $\tau_c = 3$, **a** without additional torque and **b** with $\Omega = 1$. The color scale is cut off for densities larger than 2.

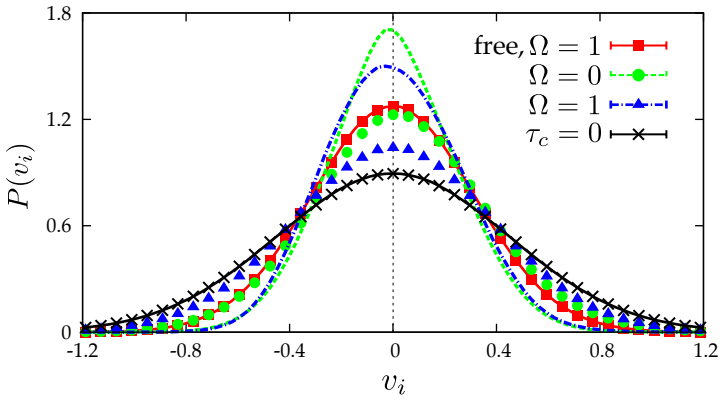

Figure 3.6.: Velocity distribution (v_x – symbols, v_y – lines) for particles driven by non-thermal colored noise with $\tau_c = 1$, $\gamma_0 = 0.2$, $\mathcal{D}_\xi = 0.04$. Except for the red distribution (squares), the particles are confined in Fig. 3.1 (a). For $\tau_c = 0$, the same Gaussian distribution emerges regardless of Ω.

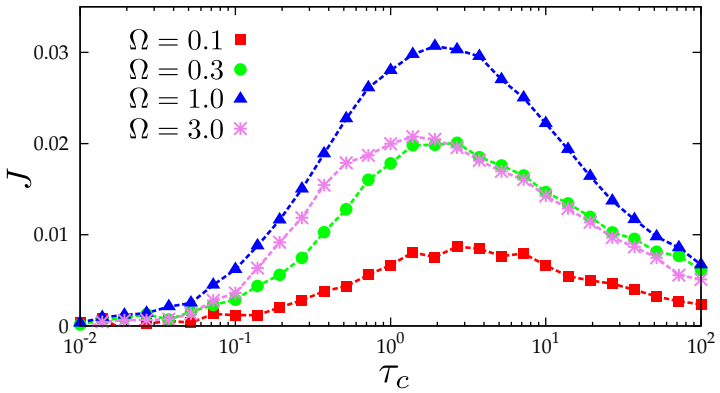

Figure 3.7.: Net transport for particles driven by non-thermal colored noise for several mean torques at $\gamma_0 = 0.2$, $\mathcal{D}_\xi = 0.04$. The channel geometry is specified in Fig. 3.1 (a).

J converges to zero, which is consistent in view of the white noise case that follows in this limit. Therein, the equilibrium condition forbids directed transport as the noise strength in eq. (3.19) vanishes. For large correlation times the net transport also converges to zero.

The effect of the mean torque is examined in further detail for several geometries in Fig. 3.8. Evidently, J vanishes for $\Omega = 0$ and also for strong torques regardless of the mean turning direction. The direction of the net transport changes with the orientation of Ω.

Given the emergence of a directed transport, we can justify its qualitative form, i.e. the asymptotics in τ_c and Ω as well as the occurrence of a maximum, with regard to the behavior of the speed. As implied by eq. (3.26) it vanishes both for large mean torques and correlation times. For transport to take place however, we need a torque to break the symmetry, and a nonzero correlation time for nonequilibrium. Hence we have no transport in either of the cases $\Omega \to 0, \Omega \to \infty, \tau_c \to 0, \tau_c \to \infty$, leaving only a maximum value in between, which has to change its direction with the sign if the sign of the torque switches.

We want to turn to the effects of the differing geometries in more depth now. As we see in Fig. 3.8, the anti-symmetrical behavior in Ω is only conserved as long as the lower boundary keeps as left-right symmetry (cf. Fig. 3.1 (a,c)). Otherwise, as for the edged boundaries (cf. Fig. 3.1 (b)), the heights of the positive and negative peaks differ, whereas the direction of the current coincides for $W = 1/3$ and $W = 2/3$ (i.e. is independent of the orientation of the saw teeth). Also, the position of the maximum moves to slightly smaller Ω values for the edged surface compared the disc.

If we narrow the channel by increasing the origin of the reflecting disc, the resulting transport curves also rise. However, their overall behavior remains, especially the

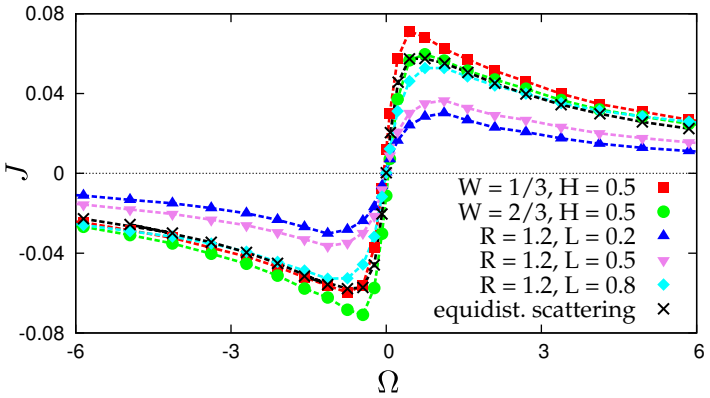

Figure 3.8.: Net transport for various confining geometries (cf. Fig. 3.1). All curves are at $\gamma_0 = 0.2$, $\mathcal{D}_\xi = 0.04$ and $\tau_c = 3$.

position of the maximum is barely altered and remains at around $\Omega^{\max} \approx 1 - 1.5$. From this we conclude, that the position of the $\Omega^{\max}$ cannot be traced to some resonant-like effect between the channel width and the cyclotron radius $R_c = v/\Omega$. Rather, the position of $\Omega^{\max}$, as well as $\tau_c^{\max}$, is a tradeoff between the necessary symmetry breaking and the reduction of the particles' speed.

Due to the unit scaling of the velocity, our net flux is identical to the mean velocity in x-direction, $J = \langle v_x \rangle$. Other correlation ratchets [11, 107] display values for $\langle v_x \rangle$ in the same order of magnitude.

3.3.3. Elucidation of the Transport Mechanism

There are three possible types of trajectories in our channel: particles in the middle perform a more or less circular motion without net bias, whose regularity is enhanced by Ω and decreased by $\mathcal{D}_\xi$ and γ_0. Particles near the top eventually collide with the wall and are reflected. A counter clockwise mean turning rate then results in a forward motion and multiple further reflections. If we consider a particle that is driven to the wall by a noise pointing into that particular direction, the noise works largely as a drag force after reflection. It is still oriented in the same direction, whereas the particle has changed its own. As a result, the velocity normal to the boundary decreases (cf. Fig. 3.6). Once the noise orientation has changed (after about $\Delta t \approx \tau_c$), the particle is driven away from the boundary, although this may be counteracted by the particles inertia together with the torque. Such situations are shown in Fig. 3.4. Clearly visible are the repeated reflections with ever decreasing radius and speed at the top.

Without additional obstacle, particles near the bottom perform an antagonistic motion that cancels out the forward flux. The obstacle on the other hand modulates the reflection angles depending on the point of incidence. As seen in Fig. 3.4, the distance the particles have to travel until the next reflection varies depending on

whether the surface tangential is rising or decreasing. This constitutes a scattering effect that helps particles to escape from the vicinity of the boundary.

Hence the backward flux is hindered and a positive net transport emerges. In this picture, we can also explain the augmentation of J with the narrowing of the channel (cf. Fig. 3.8), for the particles cannot move as far without interaction with the boundaries. Accordingly, the proportion of intermediate unbiased motion is reduced and the impact of the symmetry breaking enhanced.

We confirm this rationale by considering a box with a flat but rough lower boundary, modeled by random equidistributed reflection angles (cf. Fig. 3.1 (c) and Fig. 3.8, black symbols). Obviously, this leads to a similar behavior of J.

Consequently, the flux is dominated by the sliding motion along the flat boundary and affected by the persistence, the torque and the noise driven velocity. In contrast, the geometry of the confinement and the shape of the lower boundary appear to be less important and influence the total value of J rather than its form. To evaluate qualitatively the dynamical dependence of the current, we expect that $J = J(\tau_c, \Omega, |\mathbf{v}|)$. It has to vanish if any of these three parameters vanishes, which favors a product of them. We can assume proportionality to the velocity, which we approximate by $\sqrt{\langle \boldsymbol{v}\boldsymbol{v} \rangle}$. Then, the dependence from the torque is met by an additional factor $\sqrt{\Omega}$. J rises linearly for small τ_c, in comparison to the numerical results this must be supplemented by an additional damping for large ones. Hence we propose

$$J \propto \operatorname{sgn}(\Omega) \sqrt{|\Omega| \langle \boldsymbol{v}\boldsymbol{v} \rangle} \tau_c \exp(-\tau_c/4), \tag{3.29}$$

which mimics the some aspects of the numerical results quite well, albeit with some quantitative deviations. Its course is shown in Fig. 3.9 as a function of the correlation time τ_c and the constant torque Ω. Eq. (3.29) yields a optimal torque at $|\Omega^{\max}| = 2\pi/\tau_c + \gamma_0$, where the transport has a maximum of $J^{\max} \propto \tau_c \exp(-\tau_c/4)$. This behavior can also be seen in Fig. 3.7, where $\Omega^{\max}$ wanders to slightly smaller values with τ_c, and in the height of the corresponding peaks. It can be interpreted as a time scale merging between the period due to the torque $\propto 1/\Omega$ and the two relaxation times τ_c and $\tau_{\text{inertia}} = 1/\gamma_0$ that characterize the persistence of the motion.

3.4. Conclusion

A persistent, circular motion of Brownian particles appears in many biological and artificial systems. In this chapter, we have studied their behavior in an additional geometric confinement, and investigated whether the particles' unbiased motion can be rectified by the confining channel geometry. Even though related studies of transport mechanisms possess some of the features, the combination of the asymmetric channel geometry with a dissipative dynamics and a nonzero mean torque to realize directed transport is new.

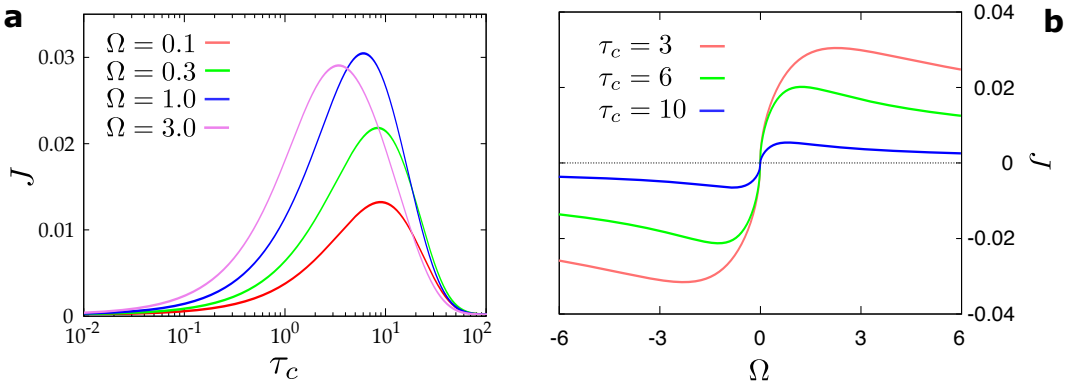

Figure 3.9.: Net transport from phenomenological formula (3.29), as a function of the **a** correlation time and **b** torque. All curves are at constant $\gamma_0 = 0.2$, $\mathcal{D}_\xi = 0.04$. The height of the blue curve is normalized to the peak flux of Fig. 3.7. The results can be compared to Figures 3.7 and 3.8,

Expectedly, in thermal equilibrium no transport arises. Outside of thermal equilibrium however, the active Brownian particles can effectively draw energy from an internal heat bath decoupled from the dissipative loss of their motion. Their noisy motion is rectified, leading to the emergence of directed transport. We have given a qualitative explanation of the mechanism that leads to this symmetry breaking, namely the particle hopping along the boundaries disrupted by the scattering effect of the reflecting disk/triangle. Optimal transport is reached for intermediate values of the torque and the persistence length, which we interpreted as a time scale merging between the period due to the torque, which is proportional to $1/\Omega$, and the two relaxation times τ_c and $\tau_{\text{inertia}} = 1/\gamma_0$ that characterize the persistence of the motion.

Due to the general settings of the propulsion, particles and geometry, our investigation might be the starting point for more precise application oriented modeling of noisy active particles. The case of a position dependent torque field might be of interest, for bacterial systems this can be related to the chemotactic response of bacteria like Escherichia coli and Salmonella [38, 96]. Depending on external stimuli, like an increasing chemoattractive gradient, they alter the probability of a clockwise rotation or a straight movement, as well as the speed of swimming. Also, it will be worthwhile to consider the motion of a moving barrier itself, which receives momentum by collisions with active particles. Recent experimental studies have observed how Escherichia coli [34] and Bacillus subtili [170] bacteria moving randomly in a fluid film can power submillimeter gears with asymmetrical teeth.

Part II.

Transport by Molecular Motors Across the Cytoskeleton

4. Intracellular Transport

Molecular motors walking on the cytoskeleton form the backbone of all active transport processes within cells. We briefly introduce the biological background and show why passive diffusive transport does not suffice. Afterwards, we discuss simple ways of modeling the stepping dynamics of molecular motors. Coming from the Langevin picture in part I of this work, the motor is regarded as a Brownian particle diffusing on a periodic ratchet potential stemming from the underlying filament. Conformational changes allow him to overcome the potential trapping and to take a step, but only if detailed balance is broken by the influx of chemical energy. Simplifying this process gives rise to a discrete hopping motion, which then allows for other complications such as interactions with other motors on crowded tracks. Finally, we will review these hopping processes in form of the asymmetric simple exclusion process and the Langmuir process, which are the basis if the investigations in the following chapter.

4.1. The Cytoskeleton and Molecular Motors

Cells are the basic functional units of all life. They consist of cytoplasm enclosed by a membrane, and in it the cell nucleus as well as the other organelles. Some cells, such as the unicellular E. Coli bacteria that we have used as an example for the geometrical transport in chapters 2 and 3, may further have a flaggelum that is used for their propulsion. The membrane is responsible for interaction with the environment. Through channels nutrients can be acquired and metabolized garbage taken out. In the cell nucleus, the proteins needed to fulfill the cell's functions are assembled according to the DNA code. The question arises, how can the nutrients reach the nucleus and how can the proteins synthesized therein reach the outer parts?

The most obvious solution is diffusive transport. Either of the aforementioned cargos is released into the cytoplasm, and eventually reaches its destination by chance. However, diffusion in cells takes place in a highly viscous surrounding where motion is slowed by a network of obstacles, creating the so-called molecular sieving effect. We take the diffusion coefficient measured in the E. Coli cytoplasm [91] to be $D_{\text{eff}} = 7\mu\text{m}^2/s$. $D|\text{eff}$ will depend on the protein size. For this value, proteins with a weight of 40ku (u - unified atomic mass unit) were considered, the value of D_{eff} drops to $0.4\mu\text{m}^2/s$ for a protein with 250ku for example. Using the definition equation of the diffusion coefficient eq. (2.8), we can calculate the time needed for diffusive transport for different cell sizes (taken from [145]),

E. Coli	$R \approx 1\ \mu$m	$\Rightarrow t \approx 20$ms,
typical eukaryotic cell	$R \approx 10 - 100\mu$m	$\Rightarrow t \approx 2 - 200$s,
neural axon	$R \approx 10$cm	$\Rightarrow t \approx 1$ year.

So while diffusive transport may be appropriate for E. Coli bacteria, in larger cells it takes a significant amount of time. Especially for the axons[1] of nerve cells, whose length can range from millimeters to meters for motor neurons. Clearly, diffusion does not suffice as the sole source of transport.

Hence an active mechanism is needed. Within the cytoplasm, there is another structure extending throughout: the **cytoskeleton**. It is a complex network of interlinking filaments and tubules which has various different functions. For example, it gives the cell resistance to mechanical deformations, and active deformations of the cytoskeleton can be used for cell migration [50]. The purpose that we are interested in however is that it also forms a road network for intracellular transport. This part of the cytoskeleton is made up of **microtubules**, 50nm wide tunnels made up of the polar tubulin proteins, and **actin filaments**.

Now that the road is found, we specify the traffic in this analogy. It comes in the form of **molecular motors**, little proteins with two polar heads[2] attaching to the road and a neck linker that can dock to the cargo. They undergo a series of conformational changes, after a cycle of which they can step forward on the tubule, pulling the cargo with them. This nonequilibrium process is fueled by the hydrolysation of adenosinetriphosphate (ATP) to adenosinediphosphate (ADP), a process freeing an energy of about $14k_BT$[31]. Just as there are different kinds of roads, there are different kinds of motors. Among them myosins, which are walking on the actin filaments, and kinesin and dynein, which are walking in opposing directions on the microtubules.

In Fig. 4.1, a fluorescence microscopy photo of the complex network structure of the cytoskeleton is shown, as well as a rendering of a kinesin motor pulling a cargo along a microtubule. As often for biological processes, the details are intricate and the variety is endless. Several different motors can attach to a cargo, and they can even attempt to pull it in different directions, described by the tug-of-war models [67, 120, 195]. Or in fact the motor density on the filamentous track can be quite high, so that they obstruct each others motion, which we will consider for the exclusion processes in section 4.3. Also, the function of molecular motors can be entirely different. Instead of transporting cargo, they can connect different filaments, which is the basis of muscular contraction [145].

[1] Outgoing signals of a neuron are transmitted through its axon to the dendrites of other neurons.

[2] Surprisingly, they are walking with their heads instead of their feet. In organic chemistry bulky parts of macromolecules that contain functional groups are called heads. The two heads of the molecular motor are polar and can hence attach to the polar filament on which they walk.

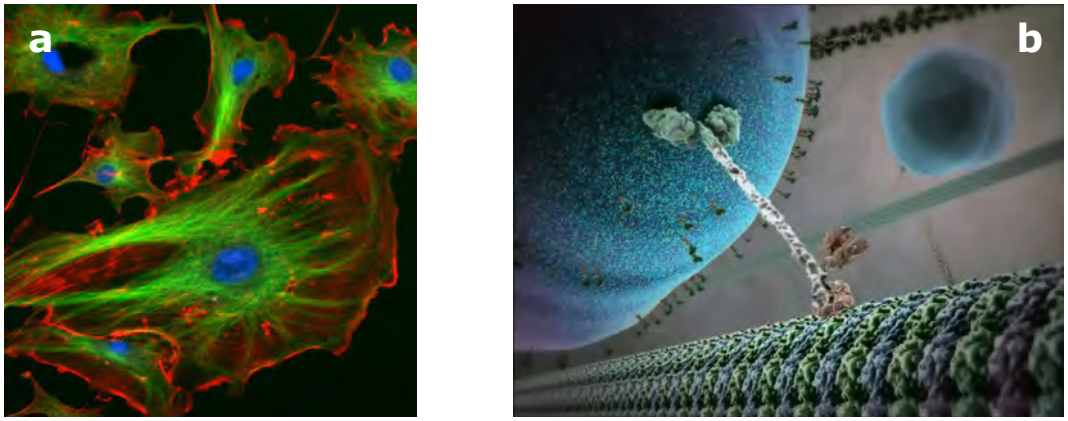

Figure 4.1.: a Fluorescence microscopy of the cytoskeleton of bovine pulmonary endothelilial cells. Nuclei in blue, actin filaments in red and microtubules in green. Taken from [121]. **b** Kinesin motor pulling a cargo along his way on a microtubule. The turquoise neck-linker connects to the huge blue cargo, while one of the motors' heads has just detached from the microtubule to perform the next step. Artistic rendering from [66].

4.2. From the Brownian Ratchet to a Hopping Process

Here, we review the mechanism how the molecular motor can perform a step. It also presents the formal link between the Langevin equations dealt with in chapters 2 and 3 and the hopping processes, which we encounter in chapters 5 and 8.

The intertwined macromolecules that make up the motor are considered as a Brownian particle that is trapped in a periodic potential made up by the filament on which it diffuses. The motor can make a transition to other conformation states, in either state he experiences the underlying potential landscape in a different way. By changing in between the states, he can escape his potential trapping and make a step on the microtubule, in a realization of a ratchet mechanism. We will show that in equilibrium detailed balance forbids a net transport, whereas if this process is biased by the hydrolysation of ATP, directed transport emerges. The details of this diffusion-conformation change-stepping process can be condensed; at first by considering a stochastic reaction network where reactions take place at discrete locations, and second by discarding the internal conformation changes altogether, resulting in particles hopping between discrete positions on the filament.

Let us give a schematic approach. In the simplest version, our molecular motor can exist in two distinct internal states [80, 130, 138]. It is attached to the microtubule, which has an ϵ-periodic ratchet potential that is different for either state. The position x of the motor is then modeled as an overdamped Brownian particle. Within the high viscosity environment of the cell, inertia quickly dissipates. Hence in eq. (2.2)

$m/\gamma \to 0$, and the velocity term is discarded (cf. section 2.2). With the additional force due to the potential landscape $-\mathrm{d}V_i(x)/\mathrm{d}x$, the Langevin equation reads

$$\frac{\mathrm{d}x(t)}{\mathrm{d}t} = -\frac{1}{\gamma}\frac{\mathrm{d}V_i(x)}{\mathrm{d}x} + \sqrt{2\mathcal{D}_\xi}\xi(t), \tag{4.1}$$

where $\xi(t)$ is Gaussian white noise of zero mean and unit variance. The index i indicates the conformational state. The corresponding probability distribution obeys the Fokker-Planck equation (cf. eq. (3.11))

$$\frac{\partial}{\partial t}P_i(x,t) = \frac{1}{\gamma}\partial_x\left((\partial_x V_i(x)) - k_BT\partial_x\right)P_i(t). \tag{4.2}$$

The additional parentheses around $(\partial_x V_i(x))$ indicate that the derivation operator therein only acts on the terms in the parentheses. Now, if we allow transitions in between the internal states, they are added as a source term to the FPE,

$$\frac{\partial}{\partial t}P_1(x,t) = \frac{1}{\gamma}\partial_x\left((\partial_x V_1(x)) - k_BT\partial_x\right)P_1 - W_{1\to2}P_1 + W_{2\to1}P_2, \tag{4.3}$$

$$\frac{\partial}{\partial t}P_2(x,t) = \frac{1}{\gamma}\partial_x\left((\partial_x V_2(x)) - k_BT\partial_x\right)P_2 + W_{1\to2}P_1 - W_{2\to1}P_2. \tag{4.4}$$

This setup is shown in Fig. 4.2.**a**. It strongly resembles the flashing ratchet of section 2.3. In comparison, the time periodic switching of a potential landscape has been replaced by an internal transition to a different state, for which the potential is experienced differently.

Adding up equations (4.3) and (4.4) leads to the conservation equation for the net probability $P = P_1 + P_2$ and flux $J = J_1 + J_2$, $\partial_t P = -\partial_x J$. We investigate the corresponding steady state solutions,

$$-\gamma J_0 = (\partial_x V_1(x))P_1 + (\partial_x V_2(x))P_2 + k_BT\partial_x P = (\partial_x V_{\text{eff}})P + k_BT\partial_x P. \tag{4.5}$$

In order to solve eq. (4.5), an effective potential V_{eff} that acts on the entire probability distribution is introduced. With the definition $\lambda(x) = P_1(x)/P(x)$ it can be written as

$$V_{\text{eff}}(x') - V_{\text{eff}}(0) = \int_0^{x'} \mathrm{d}x\Big[\lambda(x)\partial_x V_1(x) + (1-\lambda(x))\partial_x V_2(x)\Big], \tag{4.6}$$

which can be checked by simple spatial derivation. For asymmetric potentials like our ratchet potential, the effective potential generically has a nonzero average slope on large scales $x' \gg \epsilon$: $[V_{\text{eff}}(x') - V_{\text{eff}}(0)]/x' \neq 0$, although the constituent potentials V_1 and V_2 are flat [80].

If the system is in thermal equilibrium however, detailed balance holds, i.e., $W_{1\to2}P_1(x) = W_{2\to1}P_2(x)$. Following the Arrhenius equation, the probability of a chemical reaction, such as the conformational change that our molecular motor performs, falls exponentially with the required activation energy. In our case, the

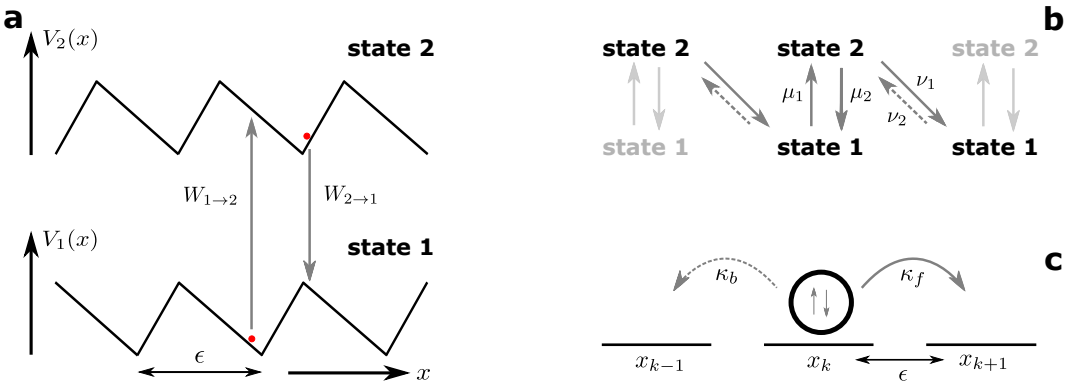

Figure 4.2.: **a** Schematic of a conformation ratchet. A Brownian particle is confined near the minimum of a periodic potential landscape $V_1(x) = V_1(x + \epsilon)$. By an internal conformation change it experiences a spatially shifted potential landscape $V_2(x) = V_1(x - \epsilon/3)$. From here, it can transition back to its original state, or to a state 1 conformation one landscape spacing ϵ farther. This results in an effective particle flux, unless in thermal equilibrium the transition rates obey detailed balance. **b** If the position is discretized into areas one lattice spacing ϵ apart, this process can be seen purely as chemical reactions between the different states. A flux results, if particles are more likely to transition forward from state 2 than backward from state 1. **c** If the internal dynamics is neglected entirely, we have a particle on a lattice with a forward and backward hopping rate.

activation energy is the potential energy difference at the position x where the conformational state is changed. For the ratio of the rates we have

$$\frac{W_{1\to2}}{W_{2\to1}} = \exp\left(\frac{V_1(x) - V_2(x)}{k_B T}\right). \tag{4.7}$$

In this case λ is given by

$$\lambda(x) = \left[1 + \exp\left(-\frac{V_1(x) - V_2(x)}{k_B T}\right)\right]^{-1}. \tag{4.8}$$

Substituting eq. (4.8) into eq. (4.6) shows that the effective potential must be a periodic function, since all its parts consist of functions with the periodicity ϵ. This means, that on a large scale there is no net force acting on the particles, $x' \gg \epsilon$: $[V_{\text{eff}}(x') - V_{\text{eff}}(0)]/x' = 0$. No transport can arise.

The detailed balance can be broken, if chemical energy is fed into the system.

Following [130], such a reaction scheme can be written as

$$\begin{aligned} S_1 &\underset{\alpha_2}{\overset{\alpha_1}{\rightleftharpoons}} S_2, & \alpha_1/\alpha_2 &= e^{\left(\frac{V_1(x)-V_2(x)}{k_BT}\right)}, \\ S_1{+}\mathrm{ATP} &\underset{\beta_2}{\overset{\beta_1}{\rightleftharpoons}} S_2 + \mathrm{ADP} + P, \quad \Longleftrightarrow & \beta_1/\beta_2 &= e^{\left(\frac{V_1(x)-V_2(x)+\Delta\mu}{k_BT}\right)}, \\ S_1{+}\mathrm{ADP} + P &\underset{\gamma_2}{\overset{\gamma_1}{\rightleftharpoons}} S_2 + \mathrm{ATP}, & \gamma_1/\gamma_2 &= e^{\left(\frac{V_1(x)-V_2(x)-\Delta\mu}{k_BT}\right)}, \end{aligned} \tag{4.9}$$

where the two conformational states are denoted by S_1 and S_2, and α_i, β_i and γ_i denote the transition rates of the individual processes. Obviously, besides their position dependence (cf. the sketched ratchet potentials in Fig. 4.2.**a**), they will also depend on other parameters such as the ATP concentration.

The first reaction pathway are thermal state transitions, while the others involve a change in the chemical potential. The second reaction includes the hydrolysation of ATP to ADP with a chemical free energy gain $\Delta\mu$, whereas in the third reaction the hydrolysation occurs in the opposite direction, with a loss of chemical free energy. The total transition rates from all reaction pathways eq. (4.9) gives

$$\frac{W_{1\to2}}{W_{2\to1}} = \frac{\alpha_2 e^{\left(\frac{V_1(x)-V_2(x)}{k_BT}\right)} + \beta_2 e^{\left(\frac{V_1(x)-V_2(x)+\Delta\mu}{k_BT}\right)} + \gamma_2 e^{\left(\frac{V_1(x)-V_2(x)-\Delta\mu}{k_BT}\right)}}{\alpha_2+\beta_2+\gamma_2}, \tag{4.10}$$

which differs from the detailed balance expression eq. (4.7). Without detailed balance, the effective potential eq. (4.6) again induces a large scale net force that is driving the transport. A numerical approach will be necessary to find the steady state solution of eqs. (4.3) and (4.4).

In a further simplification, the transition rate functions are taken to be localized in the potential minima [110]. The minima's discrete set of positions $\{x_k = k\epsilon | k \in \mathbf{N}\}$ then replaces the continuous position variable. The resulting discrete Brownian ratchet can be mapped onto a stochastic reaction network, see Fig. 4.2.**b**. The dynamics is described by the coupled master equations

$$\frac{\mathrm{d}}{\mathrm{d}t}P_{k,1} = \mu_2 P_{k,2} - \mu_1 P_{k,1} + \nu_1 P_{k-1,2} - \nu_2 P_{k,1}, \tag{4.11}$$

$$\frac{\mathrm{d}}{\mathrm{d}t}P_{k,2} = \mu_1 P_{k,1} - \mu_2 P_{k,2} + \nu_2 P_{k+1,2} - \nu_1 P_{k,1}, \tag{4.12}$$

where the additional index k denotes the number of the potential minimum, $P_{k,i}(t) = P_i(x_k, t)$. In comparison with eqs. (4.3) and (4.4) we see that the continuum diffusion and drift terms are replaced by hopping reactions in between neighboring states.

If we are not interested in the mechanics of a step, the internal state changes can be discarded altogether. All processes are then condensed into a single forward and backward hopping rate, κ_f and κ_b, as depicted in Fig. 4.2.**c**. Obviously, transport emerges once κ_f and κ_b differ. Such a reduction of complexity gives the opportunity to investigate new problems, like interactions between motors on a crowded track.

Figure 4.3.: a The asymmetric simple exclusion process. Particles can hop forward and backward on a lattice if those neighboring sites are not yet occupied. **b** The zero point process. Multiple particles can occupy a lattice site, the total transition rate from a site is proportional to the number of particles on it.

4.3. The Asymmetric Simple Exclusion Process

Since its introduction in the 1970, the **asymmetric simple exclusion process** (**ASEP**), has become a model system for nonequilibrium statistical physics, more specifically of stochastic transport. It is used for the abstract description of various processes, ranging from the motion of ants, pedestrians or motorized traffic, to biopolymerization, protein synthesis and the motion of molecular motors [41, 86, 88, 111, 128]. While the ASEP is a very simple driven system with hard-core interaction and biased diffusion, it shows a range of nontrivial macroscopic phenomena, among them jamming, shock fronts, phase transitions and condensation [16].

Its generic form is a one dimensional lattice of length N, onto which a number of particles is distributed. The remaining sites are empty. Each of the particles can now hop to neighboring empty sites, to the left with rate κ_b and to the right with rate κ_f. If the neighbor sites are occupied, hopping is prohibited. Hence the name exclusion process. As a result, the particles perform a biased random walk with an exponentially distributed waiting time between subsequent steps, whose mean is given by $\tau = 1/(\kappa_f + \kappa_b)$. This setup is illustrated in Fig. 4.3.**a**.

The ASEP is a Markov process; all possible reactions depend only on the current configuration of the lattice. As we will see, the ASEP can fulfill the Burgers' equation in a continuous limit. Simple cases of the ASEP are exactly solvable, either by applying the methods of the random walk, or by requiring more sophisticated analysis in form of matrix equations [32, 57, 58].

If the rates κ_f and κ_b are identical, we speak of an symmetric exclusion process instead. In case that one of the rates is zero, the term **totally asymmetric simple exclusion process** (**TASEP**) is used.

It is also possible to neglect the exclusion rule, in which case an arbitrary number of identical particles can occupy an individual lattice site. Such a setup is called the **zero-range process**. It is depicted in Fig. 4.3.**b**. The total transition rate from one site to the next is proportional to the number of particles on it. It is analytically solvable, since its partition function factorizes, cf. [155]. We remark that the zero-range process resembles the stochastic particle hopping model for resistive

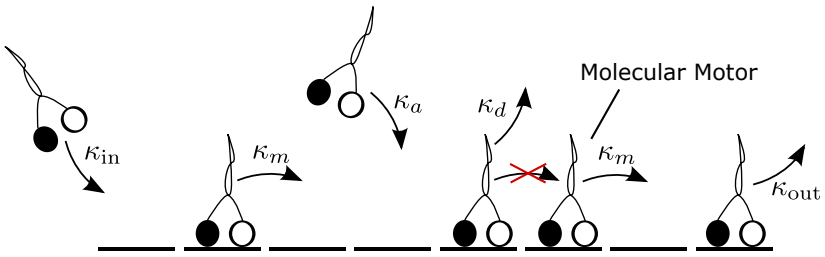

Figure 4.4.: Schematic of the Langmuir process. Molecular motors are hopping forward on an actin filament, but only if the next lattice site is empty. They can also attach and detach from the filament, and enter or leave it at both its ends with the specified rates.

switching that we will treat in chapter 8, albeit the time dependent and nonlocal transition rates therein forbid such an easy analytical treatment.

In the context of intracellular transport, the hopping particles of the ASEP are the molecular motors, and the lattice corresponds to the microtubule. Motor transport (or cargo transport if attached to the motors) results as a sequence of elementary hopping processes. Although such models are abstract and highly idealized descriptions of reality, they capture essential and relevant features of motor dynamics while requiring only a comparatively small number of parameters

Adding further complications make the exclusion processes well suited to describe the motion of molecular motors. One of the most basic of such alterations is the **Langmuir process**. It is a TASEP supplemented with an adsorption-desorption kinetics, the motors can detach from the filament with a rate κ_d and attach to an empty site with the rate κ_a, while they move forward with the rate κ_m. These processes take place on a finite lattice. The motors can enter it on the first site with a rate κ_{in} and leave on the last site with κ_{out}. The Langmuir process is illustrated in Fig. 4.4. If however, biological considerations like the unstable connection of the motors to the microtubule are considered, it is no longer possible to obtain exact results. We are forced to switch to a mean-field description [17, 43], which we now apply to the Langmuir process.

Let a configuration of lattice vacancies $(n_1, n_2, \cdots, n_L)$ be denoted by $\mathcal{N}$, and by $\{\mathcal{N}'\}$ the set of configurations that arises from $\mathcal{N}$ through a single particle hopping to a neighboring site. Each lattice site i can either be occupied by a motor, which is denoted by $n_i = 1$, or be empty, which is denoted by $n_i = 0$. Then the evolution of the corresponding probability distribution is governed by the master equation

$$\frac{\mathrm{d}}{\mathrm{d}t}P(\mathcal{N},t) = \sum_{\{\mathcal{N}'\}\neq\mathcal{N}} \Big(- W_{\mathcal{N}\to\mathcal{N}'}P(\mathcal{N},t) + W_{\mathcal{N}'\to\mathcal{N}}P(\mathcal{N}',t)\Big), \tag{4.13}$$

where $W_{\mathcal{N}\to\mathcal{N}'}$ are the transition rates from one configuration to the next. The

corresponding rates are (cf. Fig. 4.4)

$$10 \longrightarrow 01 \text{ with rate } \kappa_m, \tag{4.14}$$
$$0 \longrightarrow 1 \text{ with rate } \kappa_a, \tag{4.15}$$
$$1 \longrightarrow 0 \text{ with rate } \kappa_d, \tag{4.16}$$
$$0 \longrightarrow 1 \text{ at the first lattice site with rate } \kappa_{\text{in}}, \tag{4.17}$$
$$1 \longrightarrow 0 \text{ at the last lattice site with rate } \kappa_{\text{out}}. \tag{4.18}$$

The left-hand configuration transforms to the right-hand configuration, in case of the motor forward hopping eq. (4.14) it means that a motor at site i hops to an empty site at $i+1$, leaving his original position empty.

We are interested in a stationary solution of the motor density and flux J in this nonequilibrium system. The mean occupation density at the i-th lattice site is given by the probability weighted sum over all corresponding configurations,

$$\langle n_i(t)\rangle = \sum_{\mathcal{N}} n_i P(\mathcal{N}, t). \tag{4.19}$$

For a lattice site in the bulk the time dependence of its average occupation is given by

$$\frac{\mathrm{d}\langle n_i\rangle}{\mathrm{d}t} = \kappa_m \langle n_{i-1}(1-n_i)\rangle - \kappa_m \langle n_i(1-n_{i+1})\rangle + \kappa_a(1-\langle n_i\rangle) - \kappa_d \langle n_i\rangle . \tag{4.20}$$

For the boundary positions 1 and N, some of the neighbors are missing, while the insertion rate α and depletion rate β must be further considered,

$$\frac{\mathrm{d}\langle n_1\rangle}{\mathrm{d}t} = \kappa_{\text{in}} \langle 1-n_1\rangle - \kappa_m \langle n_1(1-n_2)\rangle - \kappa_d \langle n_i\rangle , \tag{4.21}$$
$$\frac{\mathrm{d}\langle n_L\rangle}{\mathrm{d}t} = \kappa_m \langle n_{N-1}(1-n_N)\rangle - \kappa_{\text{out}} \langle n_N\rangle + \kappa_a(1-\langle n_N\rangle). \tag{4.22}$$

The stationarity dictates that the flux is equal at all lattice sites, specifically at the start- and endpoint. Hence from eq. (4.21) follows

$$J = \kappa_{\text{in}}(1-\langle n_1\rangle) = \kappa_{\text{out}} \langle n_N\rangle . \tag{4.23}$$

Calculating the time evolution of eqs. (4.20-4.22) is nontrivial. The two-point correlation functions $\langle n_i n_j\rangle$ lead to an infinite hierarchy of higher order equations of motion. However, it is possible to obtain solutions within a mean-field approach [41, 129]. Therein, we neglect the two-point correlations and replace them with the averages of the individual lattice sites,

$$\langle n_i n_j\rangle = \langle n_i\rangle \langle n_j\rangle . \tag{4.24}$$

Further, we introduce a continuous lattice, by setting $x = i\epsilon$, where ϵ is the distance in between neighboring lattice sites. Formally, the continuum limit is taken by letting

the lattice spacing become infinitesimal while the number of lattice sites N runs to infinity, in such a way that the product of both remains constant. Let the averaged density profile be denoted by $\rho(x)$. From the connection

$$\langle n_i \rangle (t) = \frac{1}{\epsilon} \int_{i\epsilon}^{(i+1)\epsilon} \mathrm{d}x \rho(x,t), \tag{4.25}$$

we obtain $\rho(x = i\epsilon, t) = \langle n_i \rangle (t)$. The hopping that formerly depended upon the density of neighboring lattice sites now depends on those at an infinitesimal distance ϵ, which will obviously introduce a derivative. Expansion of eq. (4.25) up to the second order yields

$$\rho(x \pm \epsilon, t) = \rho(x,t) \pm \epsilon \partial_x \rho(x,t) + \frac{1}{2} \partial_x^2 \rho(x,t) + \mathcal{O}(\epsilon^3). \tag{4.26}$$

Plugging this into eq. (4.20) and discarding all terms of higher order results in

$$\frac{\partial \rho}{\partial t} = -\epsilon \kappa_m (1 - 2\rho) \partial_x \rho - \frac{\epsilon^2}{2} \kappa_m \partial_x^2 \rho + \kappa_a (1 - \rho) - \kappa_d \rho. \tag{4.27}$$

We will discuss the dynamics in a simplified case, where the additional sources and sinks due to the motor adsorption/desorption dynamics are disregarded, i.e. $\kappa_a = \kappa_d = 0$. We use the continuity equation $\partial_\tau \rho_0 = -\partial_x J_0 = 0$, which is formulated in a rescaled time $\epsilon t = \tau$ to eliminate the lattice spacing ϵ from the right hand side of eq. (4.27), to obtain an expression for the stationary flux,

$$J_0 = \kappa_m \rho (1 - \rho) - \kappa_m \frac{\epsilon}{2} \partial_x \rho. \tag{4.28}$$

Eq. (4.28) is composed of two contributions. The first contribution is the flux caused by the active dynamics of the hopping particles, since $\rho \in [0, 1]$ it is always a positive contribution, as expected by the forward motion of the particles. The second contribution is the diffusive flux caused by the gradient in the particle density, it can take either sign. The corresponding phase diagram can be calculated explicitly, [16, 88, 89]. We will only briefly state the results, they are displayed in Fig. 4.5 together with numerical simulations for the density distributions. One obtains different phases, in a low density regime $\kappa_{\mathrm{in}} < \kappa_{\mathrm{out}}$, the current is determined by the insertion rate into the system. In a high density phase $\kappa_{\mathrm{in}} > \kappa_{\mathrm{out}}$ the current is determined by the removal rate, and in the optimal current regime $\kappa_{\mathrm{in}}/\kappa_m > 1/2, \kappa_{\mathrm{out}}/\kappa_m > 1/2$ it is constant.

In case of periodic boundary conditions, the steady state solution can be easily determined from eq. (4.28). The stationary density must be constant and the diffusive term vanishes,

$$J_0^{\mathrm{pbc}} = \kappa_m \rho (1 - \rho). \tag{4.29}$$

The transport only depends on the density of motors, without motors obviously transport cannot occur, while on a full lattice everything is jammed and no transport occurs either.

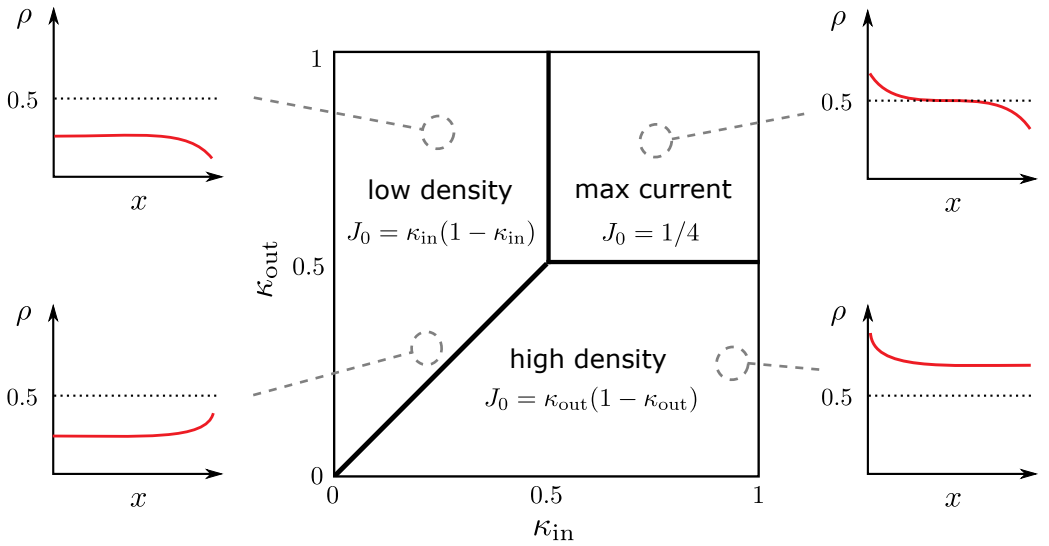

Figure 4.5.: Mean field phase diagram for the TASEP on a finite lattice with insertion and removal rates κ_{in} and κ_{out}, both normalized to the motor hopping rate κ_m. Depending on their values, we have different phases for the stationary flux, cf. eq. (4.28). Density distributions from numerical simulations are shown for the encircled values of κ_{in} and κ_{out}.

Finally, we mention that eq. (4.27) has the form of a Burgers' equation with additional source terms κ_{in} and κ_{out}. Its solutions generally include singularities, shocks in the density that are traveling through the system. These shock waves can be analyzed with the method of characteristics. Following similar arguments as in the treatment of the Langmuir process, we will encounter another generalized Burgers' equation later on for the stochastic resistive switching model in chapter 8.

Summary

In this chapter we have elaborated on the biological necessity of active transport within cells. It is achieved by molecular motors carrying cargo along the cytoskeleton, a nonequilibrium action fueled by the hydrolysation of ATP. At first, the molecular motor was considered as a Brownian particle trapped in a potential landscape. The motor can step forward by means of the conformation ratchet, its description can be reduced to a discrete hopping process. This simplification of the internal dynamics allows to us to consider new complications, namely interactions with other motors on a crowded track. With the asymmetric simple exclusion process, a simple intracellular transport model with a single motor species has been introduced. It forms the basis for more complex studies of cargo transport in the axons of nerve cells, which we

will conduct in the following chapter.

5. A Cargo Hopping Model for Slow Axonal Transport

Experimental evidence suggests a loose binding of cytosolic cargos to motors in axonal transport of nerve cells. Hence the cargo can attach and detach from the motors. Also, at higher motor densities an increasing number of these cargos show a reversal of their transport direction. With this motivation, we supplement the TASEP model for motor and cargo-motor complexes walking on the microtubule by an additional exchange mechanism of the cargos between adjacent motors. The cargo transport then takes place in different modi between a low density liquid phase without such interactions, and a high density phase in which motor jamming leads to the formation of clusters. The cargo transport speed and direction can be controlled by the density of motors on the track They will predominantly attach to single motors in the liquid phase or reverse walking cluster-quasiparticles. Within a mean field approximation together with phenomenological assumptions about the cluster distribution we can derive an analytical expression for the stationary cargo velocity.

5.1. Introduction

It is not the purpose of molecular motors to wander the cell alone, but to carry cargos along their way. Together, they form a **cargo-motor complex** (**CMC**). In most contexts of transport by molecular motors such as the ASEP and Langmuir process discussed in chapter 4, the connection between the cargo and the molecular motor is considered fixed. Hence the dynamics of the cargo follows that of the motor pulling it [87, 194]. However, for slow axonal transport, experimental evidence suggests that the combination of molecular motor and cargo is rather loose.

If we look at the transport in neuronal axons, two types prevail: the fast transport of vesicular cargos and the much slower transport of cytosolic cargos. The latter are categorized into two sorts, cytosolic protein complexes (*slow component b*) and neurofilaments (*slow component a*). While their overall transport speeds, found by radiolabeling [18], are much slower, the instantaneous transport speeds for slow component a and b, as measured by light microscopy, are of the same order of magnitude as for vesicular cargos. This is because the cytosolic proteins show quick bouts of rapid movement, combined with inactive periods [19].

The transport mechanism for vesicular cargos has long been attributed to the action of molecular motors, whereas the transport of cytosolic cargos remained

unexplained. First experiments tracking radiolabeled cytosolic proteins showed a wavelike propagation along the neuronal axon [97, 149]. Recently refined experimental techniques allowed to hypothesize, that their transport is due to attachment to molecular motors as well [28, 176]. Biotinylated kinesin motors were bound to a streptavidin-labeled qdot-cargo. They have a binding mechanism that resembles slow component b, and exhibit a weak connection of the cargo to the motor [29]. With increasing kinesin concentration, the velocity of the qdots decreases, and the amount of cargos who show a reversal of their transport direction increases.

The most common model for slow axonal transport is the *stop-and-go* hypothesis proposed in [19] that was apprehended in several other works [104, 160]. It assumes that particles will be transported by molecular motors, to which they are loosely attached. Once the attachment is dissolved, the cargos disengage from the track and pause; transport will stop. It is implemented by a stochastic reaction network, that switches between forward and backward motion, and is on- or off-track. It can be fitted to experimental data well, but does not provide an explanation of how the backward motion is realized with a single motor species.

In this work, we present a minimal agent based model for slow axonal transport. To this end a TASEP dynamics of molecular motors and CMCs is supplemented with an additional hopping process of the cargos. The transient construction of the CMC is modeled as a cargo hopping in between neighboring motors [148]. Similar systems have been dealt with in [57, 58], without motility of the CMCs. This way, we are able to account for the reversal of the transport direction with a single motor species. However, we remark that the inter-motor hopping of the cargos is speculative. It can also be interpreted as a simplified representation of a cargo attached to several motors, with new links added at one side and existing ones removed at the other, or as the 2nd order process 'cargo detaches from motor i, diffuses, and then reattaches to motor $i \pm 1$'.

5.2. The Hopping Model of Cargo Transfer

We will investigate a single species of molecular motors, designated by 1, that walks to the forward direction. With the cargos attached to CMCs we introduce a second particle type designated by 2, which follows its own dynamics. The formation of CMCs is transient, i.e. the link between motors and cargos can both be established and released. Unlike in the Langmuir dynamics of section 4.3, the motors and cargos can only hop to adjacent sites or motors, but not off-track, so that both their numbers are preserved. Different hopping rates lead to a rich behavior depending on their respective concentrations. In this very simple way the TASEP can account for both the motion of motors and cargos. If we further denote empty lattice sites by 0, these

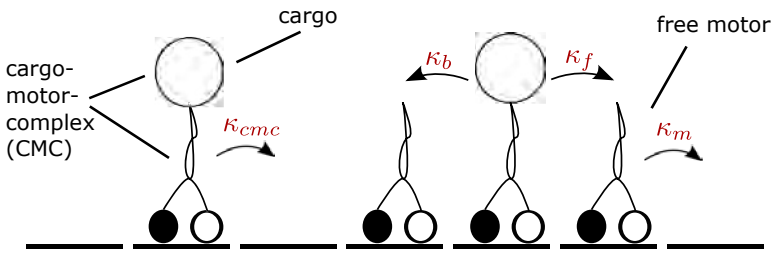

Figure 5.1.: Schematic of the allowed reactions, forward motion of unloaded (= free) molecular motors with rate κ_m and of CMCs with rate κ_{cmc} to empty lattice sites. Cargos hopping forward and backward to adjacent free motors with the rates κ_f and κ_b respectively.

processes can be written down in the scheme

$$10 \longrightarrow 01, \text{with rate } \kappa_m, \tag{5.1}$$
$$20 \longrightarrow 02, \text{with rate } \kappa_{cmc}, \tag{5.2}$$
$$21 \longrightarrow 12, \text{with rate } \kappa_f \text{ and} \tag{5.3}$$
$$21 \longleftarrow 12, \text{with rate } \kappa_b. \tag{5.4}$$

An illustration of the hopping processes eqs. (5.1)-(5.4) is depicted in Fig. 5.1. Processes (5.1) and (5.2) represent an elementary step of a motor, that either walks alone or carries a cargo. As covered in the introduction, the motor is biased and walks in a single direction, for which he requires the subsequent lattice site to be empty. It is straightforward to assume that the CMC will move forward at a rate κ_{cmc} that is not bigger than that of free motors κ_m, since it bears extra load. In case of equality, $\kappa_{cmc} = \kappa_m$, the cargo transport of the system cannot principally distinguished from the motor transport, and all results of the TASEP still apply - except that to gain the cargo net transport one needs to multiply the TASEP transport rate with the density of CMCs. There is nothing left to discuss here.

If on the other hand $\kappa_{cmc} < \kappa_m$, the CMCs will form a kind of barrier, dragging down the entire system to their speed, since motors lack a mechanism to overtake CMC's. This is similar to a single lane road, in which a truck at the front dictates the speed for the cars piling up behind him. So the dynamic is basically a TASEP with a different hopping rate, namely κ_{cmc}. This case is not of much interest either.

Processes (5.3) and (5.4) on the other hand represent the possibility of exchanging cargos between neighboring motors, to the left and to the right. In the unbiased case $\kappa_f = \kappa_b$ the cargo hopping is similar to a diffusional action, whereas the biased case $\kappa_f \leq \kappa_b$ can be used to overcome a traffic jam of motors.

In the subsequent investigations, we will consider rates fixed at $\kappa_m = 0.7$, $\kappa_{cmc} = 0.14$, $\kappa_f = 0.6$ and $\kappa_b = 0.4$. Both the motor and CMC motion and the cargo hopping motion are biased to the forward direction.

The probability of either of the reactions (5.1)-(5.4) to occur within the infinitesimal time interval $\mathrm{d}t$ is given by $\kappa_i \mathrm{d}t$. Again we designate a lattice configuration of motors and cargos by $\mathcal{N}$, and by $\{\mathcal{N}'\}$ the set of configurations one elementary hopping reaction different from $\mathcal{N}$, with a transition rate denoted by $W_{\mathcal{N}\to\mathcal{N}'}$. The dynamics of such a system is given by the master equation

$$\frac{\mathrm{d}}{\mathrm{d}t}P(\mathcal{N},t) = \sum_{\{\mathcal{N}'\}\neq\mathcal{N}} \Big(- W_{\mathcal{N}\to\mathcal{N}'}P(\mathcal{N},t) + W_{\mathcal{N}'\to\mathcal{N}}P(\mathcal{N}',t)\Big), \tag{5.5}$$

which is distinguished from the master equation of the Langmuir process eq. (4.13) only by the different underlying allowed processes. Similarly to it, it will be impossible to solve eq. (5.5) directly, because the correlation functions of the densities at neighboring lattice sites lead to an infinite hierarchy of n-point functions. However, we can derive results in a mean-field picture.

5.3. Numerical Study: Jamming and Cluster Formation

Before we attempt to do so, let us get some feeling of the dynamics by means of numerical simulations of the cargo motility on crowded microtubules. The simulation is done with the Gillespie algorithm [36, 42, 55, 56], as befitting a large system of chemical reactions - all of the reactions (5.1)-(5.4) take place at each lattice site. The Gillespie algorithm is a variant of the dynamic Monte Carlo method, based on the drawing of two random numbers. The first random number determines which of the reactions takes place, with a probability proportional to the corresponding rate, and the second random number determines the time when the reaction takes places, according to the total reaction rate of all allowed transitions. Thereafter, the system is updated and this process is iterated for the next reaction.

We observe the stationary average cargo velocity v_c as a function of the density of motors, $\rho_m = M/N$ and the density of cargos $\rho_c = C/N$, where M and C denote the number of motors, cargos and lattice sites. In our system C is identical to the number of CMC's, for all cargos are bound to motors. Obviously, the number of motors must at least be equal, but normally larger than, the number of cargos. We assume periodic boundary conditions for the investigation.

Let us make a few principal considerations: for small densities $\rho_m, \rho_{cmc} \ll 1$ or a lack of free motors $\rho_m \simeq \rho_{cmc}$, the hopping of cargos in between motors will barely occur. Hence the transport velocity is dictated by κ_{cmc}. For large motor densities on the other hand, $\rho_m \simeq 1, \rho_{cmc} \ll \rho_m$, the inter-motor hopping processes dominate. Depending on their bias, we can even expect the transport direction to change $v_c \propto (\kappa_f - \kappa_b)$. For a large density of CMC's, $\rho_{cmc} \simeq 1$ the whole system will be fairly static, since few hopping processes are allowed. Most interesting will be the intermediate cases, in which the transport is determined by an interplay of the specific processes.

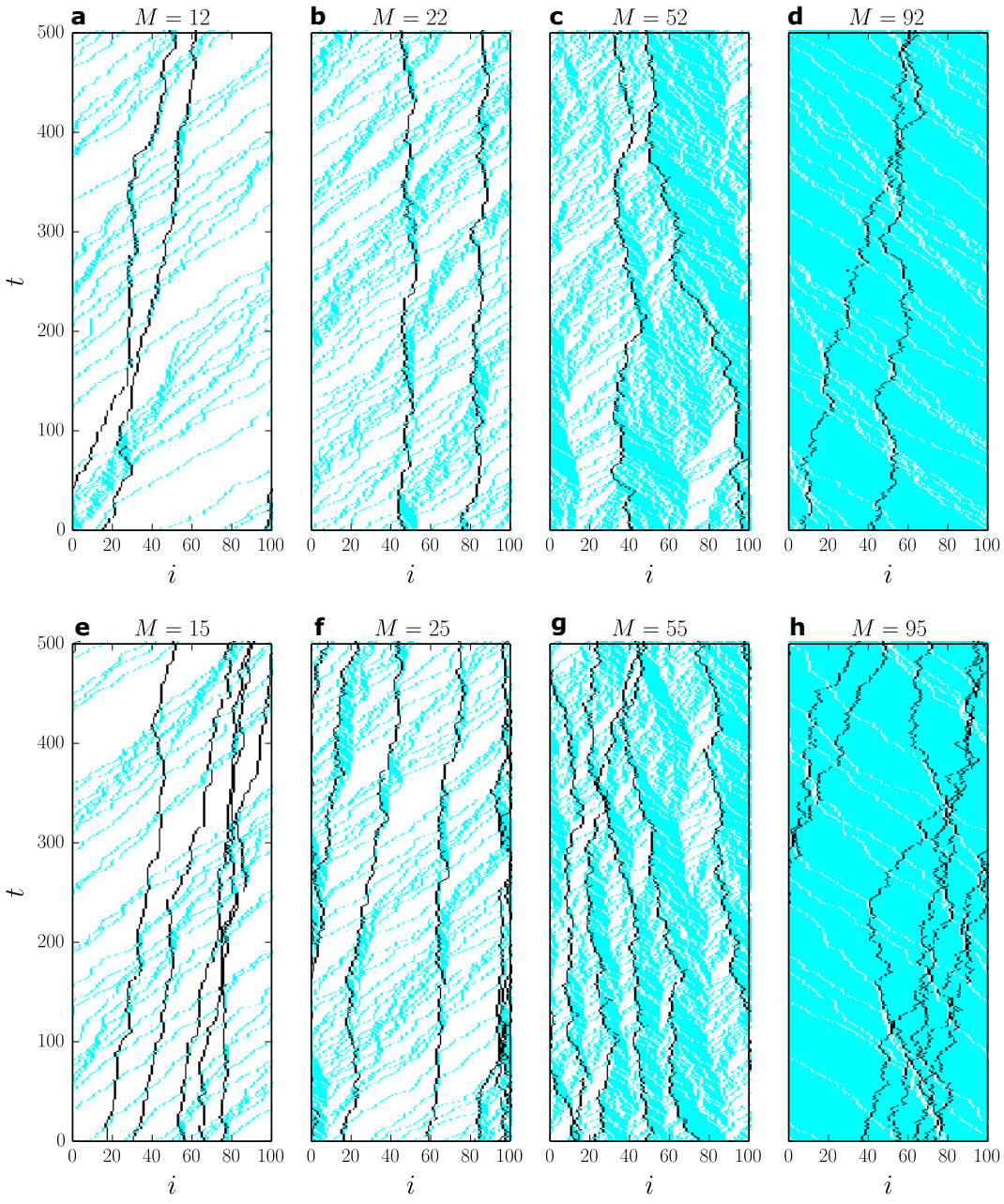

Figure 5.2.: Kymographs illustrating lattice evolution, with motors (blue), CMC's (black) and empty spaces (white) for periodic boundary conditions at fixed lattice length $N = 100$ and $\kappa_m = 0.7$, $\kappa_{cmc} = 0.14$, $\kappa_f = 0.6$ and $\kappa_b = 0.4$. For various motor numbers M and **a**-**d** 2 cargos and **e**-**h** 5 cargos, respectively. Rates fixed at $\kappa_m = 0.7$, $\kappa_{cmc} = 0.14$, $\kappa_f = 0.6$ and $\kappa_b = 0.4$. Forward hopping translates into a motion towards larger lattice site numbers with increasing time, i.e., to the upper right, backward motion accordingly to the upper left side. The cluster formation behind the CMC's can be seen in the intermediate density cases **b**, **c**, **f** and **g** by the solid shaded areas to their right-hand sites.

In Fig. 5.2, various of these cases are shown as kymographs in a small lattice. Here, we already find our considerations confirmed. For small motor densities (Fig. 5.2.**a**) the CMC's move forward with a small rate, basically dictated by κ_{cmc}, the free motors seem to pass through the CMC's (this is when the cargo hops), barely changing their trajectories, but leading to small excursions to the left at times. For increased motor densities (Fig. 5.2.**b**), these excursions become more pronounced and compensate the forward motion of the motors entirely. No transport seems to take place. On a more densely crowded track (Fig. 5.2.**c**), the motion direction of the cargo reverses. Hopping in between motors is the dominant process. We can see how the CMC's form a barrier, behind which the motors assemble. A sort of jamming sets in. Due to the difference in the cargo densities on both sides, the cargos hop preferentially backwards, which causes the reversal of the transport direction. At even higher densities (Fig. 5.2.**d**), there is no longer a noticeable motor density difference left and right of the cargos. Instead of motors hopping to the forward, it seems like lattice vacancies, i.e. empty sites, perform an antagonistic backwards motion. The mean hopping direction of the cargos in this case is determined by $\kappa_f - \kappa_b$, which for the chosen parameters translates to a forward motion.

If we compare different densities of cargos (Fig. 5.2.**a**-**d** vs **e**-**h**), we note that in general the reversals of the transport directions are more emphasized for small ρ_c. This is because the cargos cannot overtake each other and thus tend to block either motion.

The mean cargo transport velocity v_c as a function of both the motor and cargo densities is depicted in Fig. 5.3. We see our general considerations and the kymographs affirmed. v_c describes a U-form if plotted against the motor density. The changes in the average transport speed are less pronounced for higher cargo densities ρ_c. Only for small ρ_c, there is a sufficient one sided jam so that the direction of transport is actually inverted, with the hopping rates used in Fig. 5.3 an inversion of the transport direction requires $\rho_c \lesssim 0.1$. Interestingly, this inversion happens albeit the hopping of the cargo is biased to the forward direction as well, $\kappa_f - \kappa_b > 0$.

Let us further dwell in the different modes of transportation that our system exhibits. Already by looking at the kymographs for intermediate motor densities (Fig. 5.2.**d**,**e**,**f**,**g**), it becomes apparent that ρ_m varies on both sides of the CMC's. This can be explained by the jamming effect caused by the reduced forward motion rate of the CMC. As a result, motors accumulate on the left hand side of the CMC, and rarefy on the right. Around the area of the motor, a cluster of motors emerges, i.e., a consecutive sequence of motors or CMCs that is not interrupted by an empty lattice site. With growth on the one site and evaporation on the other, the cluster will move toward the direction opposing that of the motors. The CMCs, in their role as crystallization points of the cluster, move along with them. Since the hopping of cargos can only take place within the clusters, the effective hopping rates must be affected by the condensation and evaporation of the cluster. This mechanism can even lead to a reversal of the direction of transport, as seen in Fig. 5.3, and is

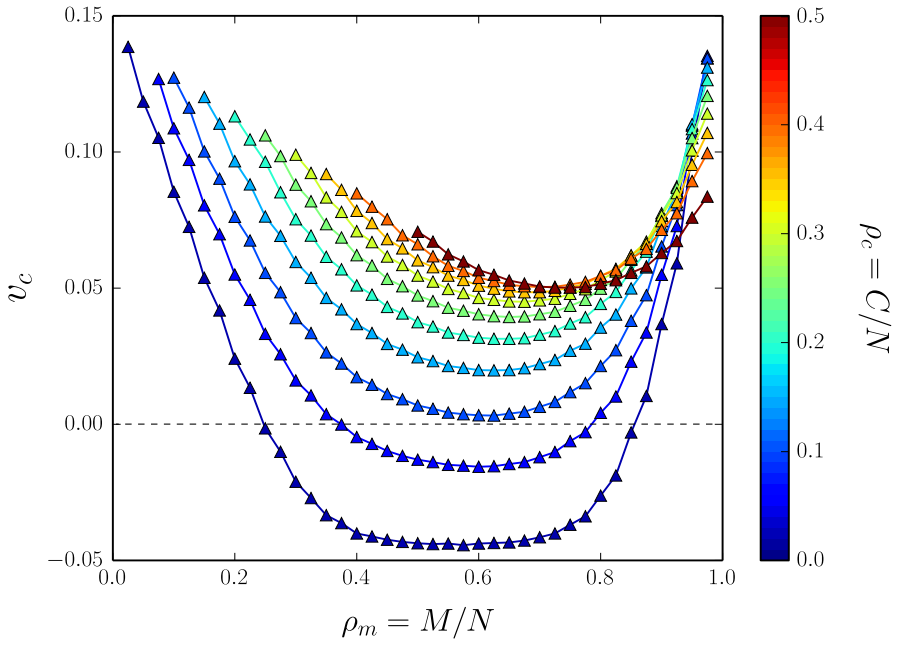

Figure 5.3.: Average cargo transport velocity v_c over motor density for various cargo densities (color coded). Lattice length $N = 10^5$, errors small against symbol size.

large enough to overcome the cargos' bias of motion in the cluster that is given by the difference in their forward and backward hopping rates. In Fig. 5.4 a schematic representation of the clustering process is shown.

We want look at the clustering quantitatively. The probability that a lattice site is occupied by a cluster, P_{cl} must go to zero for an empty lattice, while for a completely crowded lattice it is unity. It must increase with the number of motors, and deviate from the motor number most for small occupation densities, since motors are unlikely to have neighbors in this case. Hence we suggest the function

$$P_{\mathrm{cl}}(\rho_m) = (\rho_m)^{\alpha}\,, \tag{5.6}$$

which is fitted in Fig. 5.5.**a** against the numerical result of the clustering probability for various motor and cargo densities. In good agreement we take $\alpha = 1.3$. Relation (5.6) will be used in further analysis later on. In particular the number of cargos has only little effect on the clustering probability. However, the number of cargos changes the distribution of cluster sizes significantly, as shown in the corresponding histograms Fig. 5.5.**b**. With cargos, the contribution of large clusters to the clustering probability P_{cl} increases. Hence we interpret the CMCs as crystallization points of traffic jams; random collisions of a few motors on a crowded track are replaced by extended jams.

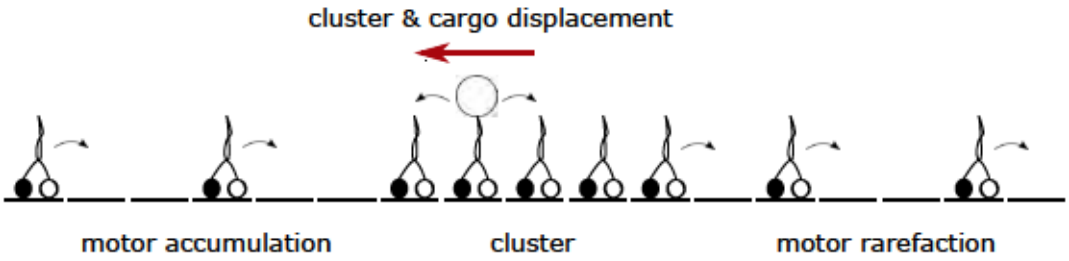

Figure 5.4.: Schematic of motor accumulation and rarefaction around a CMC, which forms the crystallization point of a cluster of motors. Due to the CMC's slower motion rate, particles accumulate on the left side of the CMC, leading to a jam. If the cargo binds to the motor on to the left, the freed motor on the right escapes the cluster eventually. Accordingly, the cluster will move in the direction opposing walking direction of the motors.

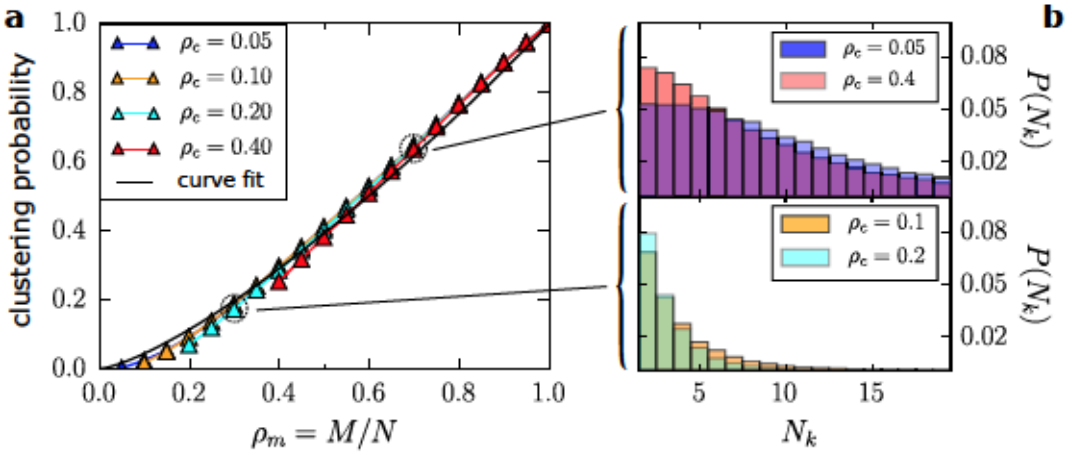

Figure 5.5.: Cluster formation on a crowded microtubule. A cluster is defined as an uninterrupted sequence of at least two motors. **a** The probability ratio that a lattice site is occupied by a cluster is shown as a function of the motor density. A least square fit to eq. (5.6) yields $\alpha = 1.30 \pm 0.02$ for $\rho_c = 0.05$, a value that only slightly increases to $\alpha = 1.33 \pm 0.02$ for $\rho_c = 0.4$. **b** Histogram of the cluster sizes for the encircled values beneath. It shows the probability that a particle is part of a cluster with the length N_k. The remaining motors are free. The distribution of the cluster sizes varies for different number of bound cargos, while the clustering probability on the lattice basically only depends on ρ_M.

5.4. A Mean Field Analysis

Similar to the case of the Langmuir dynamics, it is not possible to derive analytical results, so we will resort ourselves to a mean-field analysis. The resulting equations that describe the continuous time evolution of the system of particles obeying the dynamics defined in eqs. (5.1)-(5.4) are:

$$\begin{aligned}\frac{\mathrm{d}\langle m_i(t)\rangle}{\mathrm{d}t} =& -\kappa_m \langle u_i(1-m_{i+1})\rangle + \kappa_m \langle u_{i-1}(1-m_i)\rangle \\ & -\kappa_{cmc}\langle c_i(1-m_{i+1})\rangle + \kappa_{cmc}\langle c_{i-1}(1-m_i)\rangle\,,\end{aligned} \tag{5.7}$$

$$\begin{aligned}\frac{\mathrm{d}\langle c_i(t)\rangle}{\mathrm{d}t} =& -\kappa_{cmc}\langle c_i(1-m_{i+1})\rangle + \kappa_{cmc}\langle c_{i-1}(1-m_i)\rangle \\ & -\kappa_f\langle c_i u_{i+1}\rangle + \kappa_f\langle c_{i-1}u_i\rangle - \kappa_b\langle c_i u_{i-1}\rangle + \kappa_b\langle c_{i+1}u_i\rangle\,,\end{aligned} \tag{5.8}$$

where the average motor density at the i-th lattice sites is denoted by $\langle m_i(t)\rangle$ and the average cargo density by $\langle c_i(t)\rangle$. Since every CMC is made up of a cargo coupled to a motor, the hopping of the CMC contributes to the motor movement in eq. (5.7), and is identical to the dynamics of the cargos eq. (5.8), to which the inter-motor hopping processes contribute as well. By subtracting both equations, we can gain an expression for the unloaded motors, i.e. those without a cargo attached. We denote their average density by $\langle u_i(t)\rangle = \langle m_i(t)\rangle - \langle c_i(t)\rangle$.

Analogously to the approach in the Langmuir process, we apply a mean-field approximation to the occupation densities by decoupling the two point correlation functions. Furthermore, we introduce the continuous counterparts of the motors, cargos and unloaded motors by $\rho_m(x,t)$, $\rho_c(x,t)$ and $\rho_u(x,t)$ respectively, and expand their expressions up to the second order (Compare for the similar approach in the ASEP, eq. (4.25) and eq. (4.26)). We obtain

$$\begin{aligned}\frac{\partial\rho_m(x,t)}{\partial t} =& -\partial_x\epsilon\kappa_m\Big[\rho_u(1-\rho_m) + \frac{\epsilon}{2}\left(-\partial_x - \rho_u\partial_x\rho_m + \rho_m\partial_x\rho_u\right)\Big] \\ & -\partial_x\epsilon\kappa_{cmc}\Big[\rho_c(1-\rho_m) + \frac{\epsilon}{2}\left(-\partial_x - \rho_c\partial_x\rho_m + \rho_m\partial_x\rho_c\right)\Big]\end{aligned} \tag{5.9}$$

and

$$\begin{aligned}\frac{\partial\rho_c(x,t)}{\partial t} =& -\partial_x\epsilon\kappa_{cmc}\Big[\rho_c(1-\rho_m) + \frac{\epsilon}{2}\left(-\partial_x - \rho_c\partial_x\rho_m + \rho_m\partial_x\rho_c\right)\Big] \\ & -\partial_x\epsilon\kappa_f\Big[\rho_u\rho_c + \frac{\epsilon}{2}\left(\rho_c\partial_x\rho_u - \rho_u\partial_x\rho_c\right)\Big] \\ & -\partial_x\epsilon\kappa_b\Big[-\rho_u\rho_c + \frac{\epsilon}{2}\left(\rho_c\partial_x\rho_u - \rho_u\partial_x\rho_c\right)\Big].\end{aligned} \tag{5.10}$$

For our calculation, we assume both periodic boundary conditions and stationarity. As a result, the system must also be translation invariant and have a constant density profile. Hence the functional dependences on x and t are dropped.

It is convenient to introduce the density of empty sites (or vacancies) ρ_0 as another variable. Consquently, we can formulate the normalization equation

$$\rho_m + \rho_0 = \rho_u + \rho_c + \rho_0 = 1. \tag{5.11}$$

As usual, a continuity equation connects the time derivative of the density to the spatial derivative of the flux

$$\frac{\partial \rho_k(x,\tau)}{\partial \tau} = -\frac{\partial j_k(x,\tau)}{\partial x} \text{ with } k \in \{m, c\}, \tag{5.12}$$

with whom the expressions (5.9) and (5.10) can be identified. Eq. (5.12) is formulated in a rescaled time $\tau = \epsilon t$ to get rid of the lattice spacing ϵ. With the second derivatives disappearing due to the translation invariance, we obtain for the stationary currents

$$j_m = \kappa_m \rho_u \rho_0 + \kappa_{cmc} \rho_c \rho_0, \tag{5.13}$$

$$j_c = \kappa_{cmc} \rho_c \rho_0 + (\kappa_f - \kappa_b)\, \rho_u \rho_c. \tag{5.14}$$

By subtracting j_m from j_c the stationary flux for unloaded motors can be obtained. In case of identical hopping rates of the motors and the CMCs, $\kappa_m = \kappa_{cmc}$, we effectively only have a single motor species, and the flux eq. (5.13) is identical to that of a Langmuir process with periodic boundary conditions, given in eq. (4.29).

The cargo velocity $v_c = j_c/\rho_c$ can be easily calculated from eq. (5.14). It is positive, has a constant offset and increases linearly with the density of unloaded motors. Obviously, this behavior bears little resemblance to the numerical results shown in Fig. 5.3.

The deviations can be attributed to the assumption of a continuous density onto which the cargo hopping takes place. This assumption is introduced as a result of the MFA. In reality however, cargo exchange can only take place within the clusters, and will be interrupted at their end. The forward motion of motors and CMCs on the other hand, takes place outside or at the end of the clusters. Hence further sophistication is needed.

5.5. Cargo Transport with the Clustering Mechanism

To refine the coarse picture obtained within the MFA, we take into account the clustering. The flux of motors and cargos is split into two parts, a dense clustered phase, in which the biased cargo diffusion takes place and a low density liquid phase in which single motors and CMCs perform a totally biased walk without interactions. The fluid contains the remaining (not clustered) motors and CMCs mixed with the vacancies. Due to stationarity, we can assume that the cluster number and size distribution remains constant. The weighted sum of both fluxes yields an estimate for the total cargo transport. Some similar ideas for the split of transport modi in a two particle system have been discussed in [6].

If we denote the clustered phase by a superscript cl and the low density phase by li, the respective densities in both phases obey the normalization relations

$$\rho_m^{\mathrm{cl}} = \rho_u^{\mathrm{cl}} + \rho_c^{\mathrm{cl}} = 1, \tag{5.15}$$

$$\rho_m^{\mathrm{li}} + \rho_0^{\mathrm{li}} = \rho_u^{\mathrm{li}} + \rho_c^{\mathrm{li}} + \rho_0^{\mathrm{li}} = 1. \tag{5.16}$$

The total cargo flux is composed of two components, the cargo flux within clusters and the flux due to unhindered motion in the liquid phase. Accordingly, their individual weights are determined by clustering probability $P_{\mathrm{cl}}(\rho_m)$, whose phenomenological expression is given in eq. (5.6),

$$j_c = P_{\mathrm{cl}} j_c^{\mathrm{cl}} + (1 - P_{\mathrm{cl}}(\rho_m))\, j_c^{\mathrm{li}}. \tag{5.17}$$

Since by definition clusters have no vacancies, the forward hopping of the CMCs therein depends on the probability that the liquid phase begins at its right side. And in the liquid zone there are no neighboring particles in between which cargos can hop. Therefore we can give the following expressions for the currents in and outside the clusters,

$$j_c^{\mathrm{cl}} = \kappa_{cmc}\rho_c^{\mathrm{cl}}\,(1 - P_{\mathrm{cl}}(\rho_m)) + (\kappa_f - \kappa_m\,(1 - P_{\mathrm{cl}}(\rho_m)) - \kappa_b)\,\rho_c^{\mathrm{cl}}\rho_u^{\mathrm{cl}} \tag{5.18}$$

$$j_c^{\mathrm{li}} = \kappa_{cmc}\rho_c^{\mathrm{li}}\rho_0^{\mathrm{li}} \tag{5.19}$$

The second term in parenthesis, $\kappa_m\,(1 - P_{\mathrm{cl}})$, is a correction of the forward hopping rate κ_f. It is justified phenomenologically by taking into account the finiteness of the clusters: clusters loose motors on the right-hand-side while they acquire them on the opposite side, as it was discussed in detail in section 5.3 (compare also Fig. 5.4). Hence the forward hopping rate of the cargos must be reduced. This correction vanishes if the lattice clustering approaches unity.

In order to calculate eq. (5.17), it is necessary to express the unknown densities of motors and cargos in the cluster and the liquid phase by their known total densities ρ_u and ρ_c. Both are connected via the clustering probability,

$$\rho_u = P_{\mathrm{cl}}(\rho_m)\rho_u^{\mathrm{cl}} + (1 - P_{\mathrm{cl}}(\rho_m))\rho_u^{\mathrm{li}}, \tag{5.20}$$

$$\rho_c = P_{\mathrm{cl}}(\rho_m)\rho_c^{\mathrm{cl}} + (1 - P_{\mathrm{cl}}(\rho_m))\rho_c^{\mathrm{li}}. \tag{5.21}$$

For empty lattice spaces this can be done easily, since they only occur in the liquid zone,

$$\rho_0^{\mathrm{cl}} = \frac{\rho_0}{1 - P_{\mathrm{cl}}(\rho_m)}. \tag{5.22}$$

Unfortunately, for the remaining densities of unloaded motors and cargos in the clustered and liquid phases, such an expression can not be given. The corresponding normalization and conservation equations (5.15), (5.16), (5.20) and (5.21) yield a linear system of equations that is underdetermined. Hence we need further input

to attempt its solution. We do this by formulating another phenomenological relationship. From numerical simulations we observe that the ratio of the clustered densities of unloaded motors and CMCs is a near linear function, that maps onto the interval $[0, 1]$. Hence in a similar approach to the clustering probability we set

$$\frac{\rho_u^{\mathrm{cl}}}{\rho_c^{\mathrm{cl}}} = \frac{1-\rho_c}{\rho_c}\left(\frac{\rho_u}{1-\rho_c}\right)^{\beta}. \tag{5.23}$$

In Fig. 5.6.**a** a least square fit of this function to the simulation data is shown, from which we determine $\beta = 0.85$, again in good agreement. With both phenomenological fitting curves eqs. (5.6) and (5.23), it is possible to express the liquid and clustered densities in terms of the given total motor and cargo densities, ρ_m and ρ_c, as well as the density of unloaded motors ρ_u as auxiliary variable. This yields the expressions

$$\begin{aligned} \rho_u^{\mathrm{cl}} &= \frac{\frac{1-\rho_c}{\rho_c}\left(\frac{\rho_u}{1-\rho_c}\right)^{\beta}}{1+\frac{1-\rho_c}{\rho_c}\left(\frac{\rho_u}{1-\rho_c}\right)^{\beta}}, & \rho_c^{\mathrm{cl}} &= \frac{1}{1+\frac{1-\rho_c}{\rho_c}\left(\frac{\rho_u}{1-\rho_c}\right)^{\beta}}, \\ \rho_u^{\mathrm{li}} &= \frac{\rho_u - P_{\mathrm{cl}}(\rho_m)\rho_u^{\mathrm{cl}}}{1-P_{\mathrm{cl}}(\rho_m)}, & \rho_c^{\mathrm{li}} &= \frac{\rho_c - P_{\mathrm{cl}}(\rho_m)\rho_c^{\mathrm{cl}}}{1-P_{\mathrm{cl}}(\rho_m)}. \end{aligned} \tag{5.24}$$

In Fig. 5.6.**b** the densities obtained from simulations are compared with the analytical formulas (5.22) and (5.24). We see a good agreement between both, especially for the clustered particles. For an overcrowded microtubule $\rho_m \to 1$ the deviations in the liquid phase become significant, especially for the unloaded motors and the empty sites. However, this problem is mostly compensated for, since the liquid phase's weight scales with $1 - P_{\mathrm{cl}}$. Hence on a crowded microtubule the deviations do not contribute much to the total cargo flux.

If we plug the phenomenological formulas of the densities (5.22) and (5.24) into the cargo flux eq. (5.14), and divide by the cargo density, an expression for the average cargo velocity within our approximation is obtained. The results are shown in Fig. 5.7. We see a good qualitative agreement with the values obtained by numerical simulations, Fig. 5.3. Both the U-shape of the velocity as a function of ρ_m and the behavior for increasing ρ_c are reproduced. Particularly, for small enough cargo densities $\rho_c \lesssim 0.2$ there are reversals in the average transport direction. Also, the reversal of the most beneficial cargo density for high transport velocities reverses with the motor density in both the numerical and the analytical plot. For $\rho_m \lesssim 0.8$ the transport velocity increases with ρ_c, whereas $\rho_m \gtrsim 0.8$ it falls with ρ_c.

5.6. Summary and Outlook

The slow transport of cytosolic cargos in the axon has only recently been attributed to the action of molecular motors. It features some unusual properties: short phases of rapid motion together with longer rather inactive periods, a transport speed that

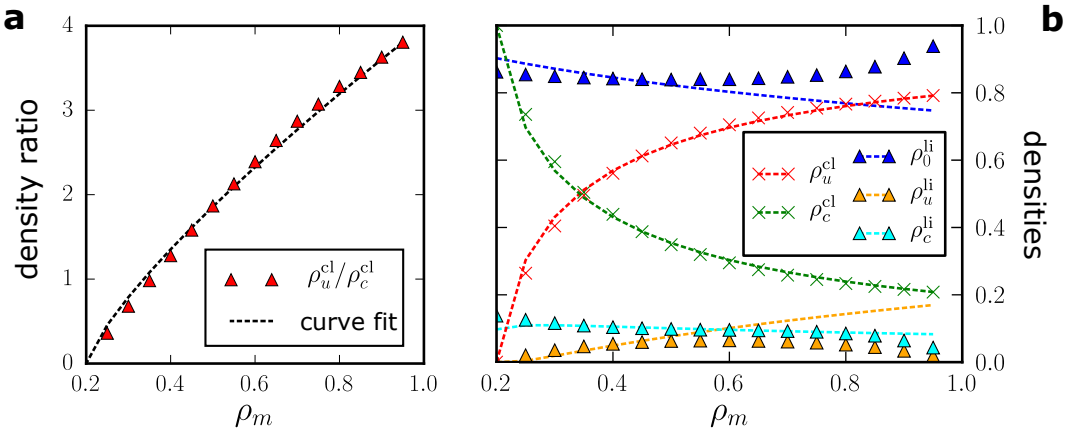

Figure 5.6.: a Least square fit of phenomenological density ratio eq. (5.23) to numerical data. For $\rho_c = 0.2$, we obtain $\beta = 0.85 \pm 0.01$. For other cargo densities the β shows only small deviations from this value. **b** Densities in the clustered and liquid phase for $\rho_c = 0.2$. Numerical Simulations (symbols) against the analytical expressions (dashed lines) eqs. (5.22) and (5.24), for which the phenomenological formulae (5.6) and (5.23) were used.

depends on the density of motors, an increasing number of which leads to more cargos showing a reversal in their transport direction.

To account for these characteristics, we proposed a novel model with loaded and unloaded motors, in which a loosely bound cargo can attach to neighboring motors. An additional cargo movement takes place on top of the TASEP for the motors. The behavior of our system was investigated by means of numerical simulations. In addition, we treated the system in a mean-field approximation that was refined by taking into account the clustering of motors, together with phenomenological assumptions about the cluster distribution.

Three distinct phases of the cargos' transport modi could be distinguished: First, in a low density phase the hopping of uninterrupted CMCs determines the transport speed, which accordingly is given by their forward stepping rate κ_{cmc}. Second in an intermediate density phase, the jamming of motors causes the formation of clusters, which coexist with the low density liquid phase. With accumulation on one side and evaporation on the other, the clusters move oppositely to the motors. The cargos can attach to these cluster-quasiparticles and reverse their average direction of motion. Third, in a high density phase the motors are mostly jammed and the bias in the cargo hopping determines the transport.

Hence, we have covered key attributes of slow axonal transport in a minimal agent based model with a cargo exchange interaction. Both numerics and a phenomenological mean-field treatment reproduced experimental results, in which cargo transport speed and direction are controlled by the motor density. Especially, we recovered

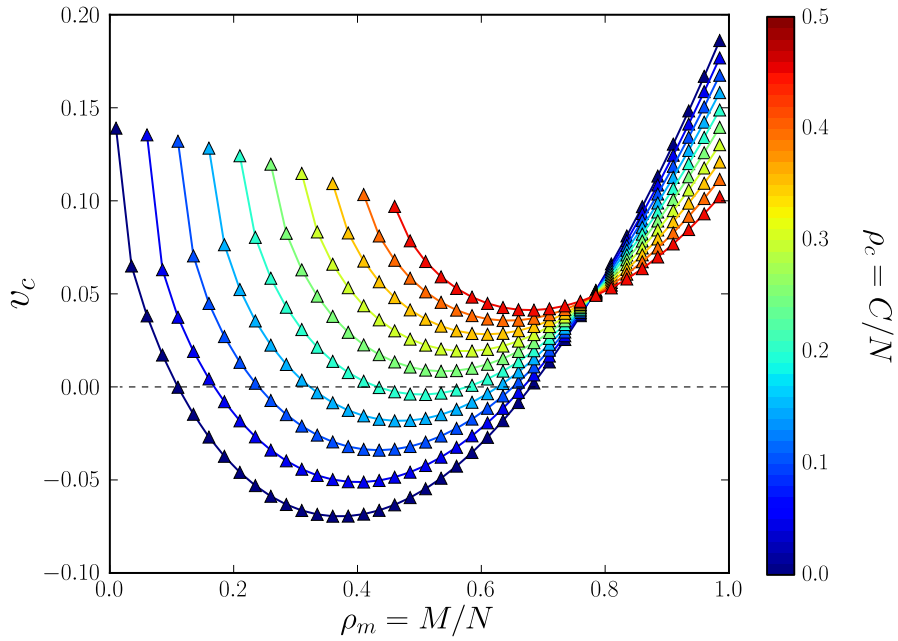

Figure 5.7.: Average cargo transport velocity v_c as given in eq. (5.17), calculated with the analytical expressions of the densities in the clustered and liquid phase gained in our phenomenological approach. Results can be compared to the corresponding numerical simulations of Fig. 5.3. The qualitative course in both is similar, a U-shape with transport direction reversals for small cargo densities below $\rho_c \lesssim 0.2$ within the phenomenological approximation, compared to $\rho_c \lesssim 0.1$ from the numerical simulations. Also, the values of the cargo velocities are in fair agreement, especially for extremal motor densities: $v_c(\rho_m \to 0) \longrightarrow \kappa_{cmc} = 0.14$ and $v_c(\rho_m \to 1) \longrightarrow (\kappa_f - \kappa_b)(1 - \rho_c)$. The latter evaluates to 0.16 for $\rho_c = 0.2$ as an example. In Fig. 5.3 we obtained $v_c \simeq 0.14$ in both cases.

that the bidirectionality of the cargo motion is controlled by the motor density alone, a result that exceeds the explanations by the *stop-and-go hypothesis*. The backward transport in our model is due to the transient attachment to backward moving clusters of jammed motors that were considered as quasiparticles.

In the present work, we have used $\kappa_f > \kappa_b$ to show that the cargo attachment to the backward moving clusters-quasiparticles is strong enough to overcome even a bias in their hopping exchange motion. Further investigations may include a deeper understanding of the influence of different hopping rates. Of special interest here is the unbiased or diffusive case $\kappa_f = \kappa_b$, for which our model predicts a more pronounced backward transport in the intermediate case and a cessation of transport for completely crowded tracks, see Fig. 5.8. Also, other ratios in the forward hopping rates of motors and CMCs, κ_{cmc}/κ_m are worth considering. They will severely affect the jamming dynamics. It is left up to future studies how the clustering mechanism

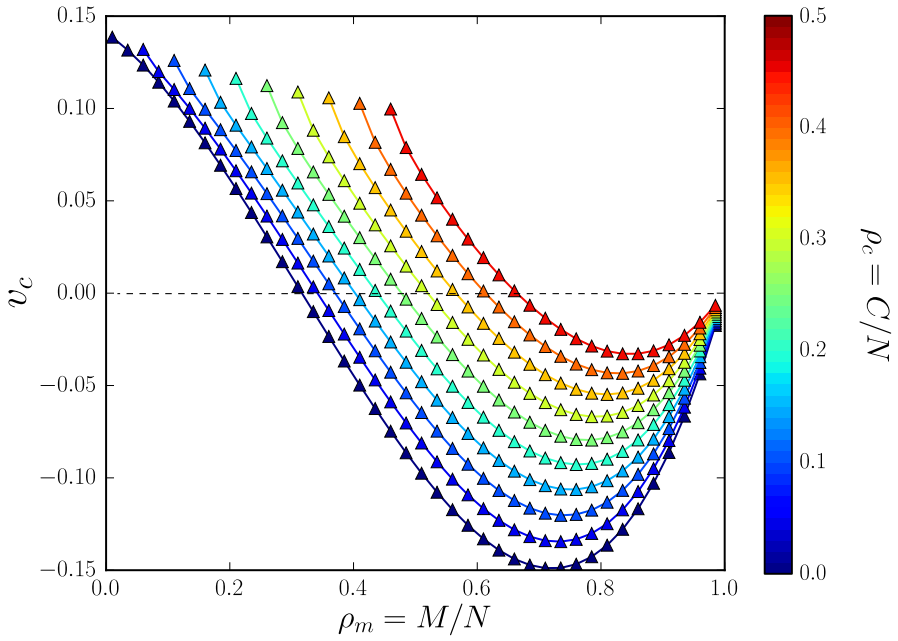

Figure 5.8.: Cargo transport velocity in the diffusive case with unbiased rates $\kappa_f = \kappa_b = 0.4$. $\kappa_m = 0.7$ and $\kappa_{cmc} = 0.14$ remain unaltered. For this small alteration in κ_f, the phenomenological fitting parameters $\alpha = 1.3$ and $\beta = 0.85$ are still valid. The behavior switches from forward transport in the low density case, to a more pronounced velocity reversal compared to Fig. 5.7 for intermediate densities. On a completely jammed track ($\rho_m \to 1$), cargo transport ceases.

and its description by means of the phenomenological approximation formulas is altered by the different rates. It will be of particular interest, if the rates can be tuned so that experimental results showing short phases of rapid motion together with longer rather inactive periods can be reproduced by the cargo hopping model as well.

Part III.

Resistive Switching

6. Resistive Switching

In this section, we lay the foundation for the investigations in the following chapters. At first, we will explain the concept of resistive switching (RS), and introduce its terminology. Out of the vast field of different types, we will elaborate mostly on the bipolar RS for the valence change mechanism (VCM) and electrochemical metalization cells (ECM). Afterwards, we will introduce its main application, the non-volatile resistive random access memory (ReRAM), and explain its use in 3d stackbars and for neuromorphic computing. Further, we will elucidate the idealized theoretical background behind resistive switching, the memristor, the illusive fourth basic passive circuit element. Finally, we will introduce the HP-memristor, a titanium dioxide based resistive switching device, for whose description a phenomenological model with memristor properties is presented.

6.1. Occurrence and Mechanisms of Resistive Switching

Resistive switching refers to a change in the resistance of a dielectric due to the action of an external electric field or an electric flux. Thereby, the resistance depends on the history of the field or flux passing through the system, hence it has a memory, which can be considered as a hysteretic effect. The basic layout for resistive switching is a two terminal device, in which the dielectric is sandwiched in between the two electrodes. An applied voltage toggles its resistance between a high and low resistive state. The nature of the underlying mechanism is complex, and varies a lot in between different materials and switching regimes.

RS has been observed in a various **transition metal oxides** (**TMO**'s), in which the transport is typically described by the motion of oxygen vacancies [150, 184]. The underlying effect are redox reactions that usually go along with a change in the valence state of the metal ion, hence the name **valence change mechanism** (**VCM**). RS also occurs in solid electrolytes, where an active electrode donates cations that are then traveling through the system. In this case we speak of **electrochemical metalization cells** (**ECM**'s)[108, 179, 180, 184, 196].

The VCM occurs in a wide range of transition metal oxides, such as manganites MnO(OH) [22, 70, 140, 150], perovskites $CaTiO_3$ [7, 13, 48] and titanium dioxide TiO_2 [53, 98, 173, 191]. It is triggered by the migration of anions, although models normally describe the motion of the corresponding oxygen vacancies. Accompanying their motion is a change in the stoichiometry. That leads to a redox reaction resulting into a valence change of the cation sublattice and the conductivity. The polarity

of the voltage pulse determines the direction of the change, i.e. either reduction or oxidation.

The ECM cell consists of an electrochemically active electrode like copper or silver, an inert electrode, usually platinum, and a solid electrolyte in between [180, 196]. The effect has been observed for a plethora of different solid electrolytes [179]. In an initial forming step, the active electrode donates highly mobile cations that are travelling through the solid electrolyte, and discharge at the inert counter electrode. This leads to the growth of a highly conductive filament, that is finally bridging both electrodes. The device is then in the low resistive state. Upon reversal of the applied voltage's polarity, these filaments dissolve again electrochemically and the ECM returns to the high resistive state. As the cations are now already in the electrolyte, for the next build up of the conductive bridge and hence switch to the low resistive state a smaller voltage pulse is needed then for the initial forming step.

Both for the VCM and ECM, the different resistive states are reached by voltage pulses with opposing polarities. Hence, their switching is called **bipolar**. Due to the strong electrical fields required for the switching, Joule heating also plays a role. While it enters mainly as a nuisance here, for other materials it can even be the dominating mechanism in the switching behavior [184]. For thermochemical cells, the high electric fields in a TMO cause a large temperature gradient around the small conducting filament. This results in the thermophoresis of the oxygen vacancies, and thereby a change in the resistive state [172, 192]. Such a cell shows **unipolar** switching behavior, meaning that its different resistive state are reached by subsequent pulses of the same polarity. However, the bipolar and unipolar operation modes are not mutually exclusive, since most materials display both to some degree, depending on the operational parameters [190].

Entirely different realizations of resistive switching are possible as well. For example, in phase change memory a chalcogenide glass switches between an amorphous and a crystalline phase, with different optical and resistive properties [26, 95, 100, 125, 189]. Optical data storage in phase change memory is the basis of the CD-RW and the Blue-Ray disc [100, 189].

Finally, a remark on the terminology: in this work, we will generally use the term resistive switching to denote the underlying physical mechanism and resistive switch for a device based on it, and memristor to denote the idealized concept, which is introduced in section 6.3. However, the use in the literature is ambiguous, and both terms are often employed interchangeably.

6.2. Applications: ReRAM in 3d Stackbars and Neuromorphic Computing

In the relentless endeavor of the semiconductor industry to increase performance, the quest for novel technologies and materials is ubiquitous. Among the most promising

candidates is the non-volatile **resistive random access memory** (**ReRAM**). The nonvolatility means that the memorized content is retained even after power is switched off. Current memory designs are either RAM, which is fast, expensive and volatile, or flash memory, which is inexpensive, slow and retains information. ReRAM is expected to combine the beneficial properties of both, to provide a highly scalable, fast, non-volatile, low power consumption and low cost memory [72, 184, 192].

But what is computer memory? Basically, it is the storage of information. The unit of the binary Boolean logic of the computer is the bit. It can have only two states, 0 and 1. In order to store information (and also to process or transmit it), information always needs a physical carrier. The information is mapped onto a physical property of the carrier, its so-called state variable, by structuring the carrier in space and time. The most simple possible carrier is a binary switch, that takes only either of the binary states. On it, the basic write and read operations can be performed. Write sets a specified state in the switch, and read detects this state. In case of resistive switching, the high resistance off-state corresponds to a logical 0, whereas the low resistive on-state corresponds to a logical 1. The logical states of a binary resistive switch are illustrated schematically in Fig. 6.1.**a**.

For relevance on an industrial scale, additional features have to be met: low production costs, low power consumption and together with it low heat dissipation, as well as stability against erroneous read-outs. Typical implementations of ReRAM for industrial use aim for enormous integration densities and stack RS elements into a nanocrossbar, layered grids of wires with RS cells in between [77, 84, 182, 192]. Here, conducting wires cross in a two or three dimensional grid, with a resistive switch placed at each intersection. In Fig. 6.2 a 3 x 3 x 3 design is depicted. Prototypes of such designs contain memories of terabyte size that fit on the area of the nail of the thumb [122].

To actually read or write information, a voltage V is applied to two orthogonal wires. Upon measuring the resulting current, we will not only gain the desired current I_{element} through the RS element that is connecting these wires, but also contributions from sneak paths around it. Assuming a ratio $R_{\text{on}}/R_{\text{off}} = 10^{-3}$ and that the red and black resistive switches of Fig. 6.2 are in the off-state, while the cyan resistive switches are in the on-state, this gives $I_{\text{sneak}} = 333 I_{\text{element}}$ and $I_{\text{read}} = I_{\text{element}} + I_{\text{sneak}} \approx V/3R_{\text{on}}$, the sneak path actually dominates the readout. On the other hand, with the red resistive switch in the on-state $3I_{\text{sneak}} = I_{\text{element}}$ and $I_{\text{read}} \approx 4V/3R_{\text{on}}$. Hence total resolution $I_{\text{on}}/I_{\text{off}} \approx 4$. Orders of magnitudes difference in the resistance lead to a small ratio in the current.

For highly integrated circuits, this memory leakage is a major problem leading to high power consumption and thermal heating as well as reading errors. It has been proposed to reduce the influence of sneak paths by changing the logical 0 and 1 from states with different resistances to states with the same high resistance, albeit with different reactions to a voltage pulse. To this end, two RS-elements are combined

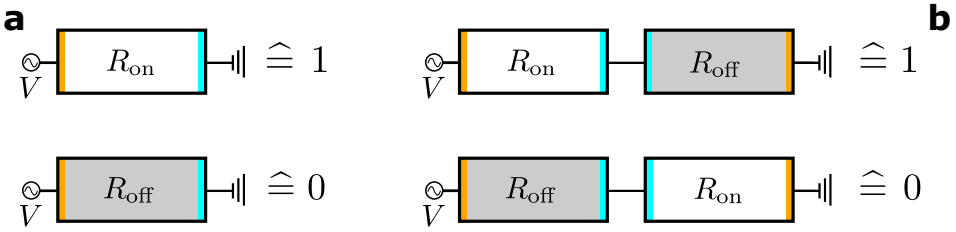

Figure 6.1.: a Logical states of a basic binary resistive switch. The dielectric is either in a low resistance on-state, corresponding to the logical 1, or in the high resistance off-state, corresponding to the logical 0. It is read and written with help of the applied voltage V. **b** Logical states of a complementary memory switch. Two binary switches are combined anti-serially, meaning that the internal order of the second is reversed with respect to the external voltage. This is indicated by an exchange of the electrodes (represented by colored rectangles). The logical state is determined by which of the switches composing the CRS is in the on- or off-state. Both the 0 and 1 have the same resistance, but will react differently to an applied signal. on-on and off-off configurations have no logical equivalent.

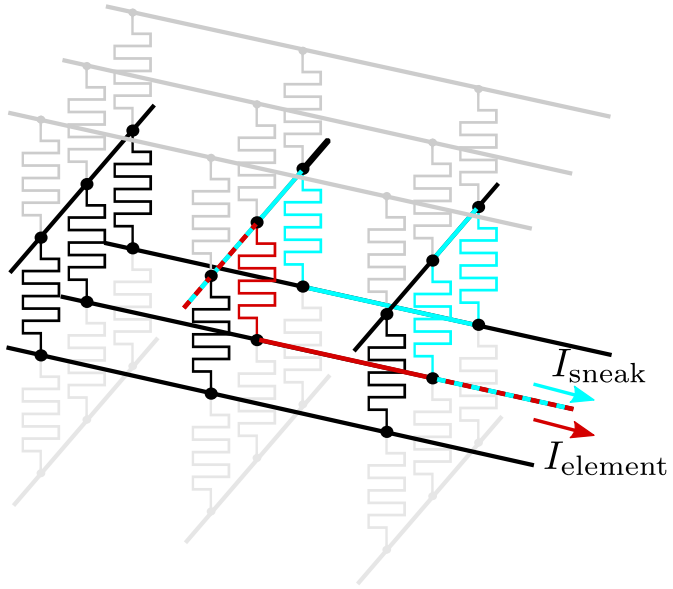

Figure 6.2.: Crossbar layout for realization of ReRAM memory element, as principally realized for relevant applications [77, 84]. Several layers of intersecting conduction wires are stacked onto one another. At each intersection, an RS element is placed. To read or write an element, a voltage is applied to two orthogonal wires, which induces a current. The total readout current is then comprised of the currents through the element that we want to determine (red path), and the sneak paths around it (one of which is given by the cyan colored path).

anti-serially, meaning that the internal order of the second element is reversed with respect to the first. This design has been referred to as **complementary memory switch** (**CRS**) by Linn et al [108]. Now, both logical states have a high resistance, albeit with differing internal states of the constituent elements. One chooses $R_{\text{off}}^{(1)} \oplus R_{\text{on}}^{(2)} \widehat{=} 0$ and $R_{\text{on}}^{(1)} \oplus R_{\text{off}}^{(2)} \widehat{=} 1$, where the superscript indicates the first and second RS-element respectively. Other combinations have no binary equivalent. In Fig. 6.1.**b** a schematic of the CRS setup is shown.

The CRS is read by sending a reading pulse through it. Depending on its state, the reading pulse will put the switch either in an on-on configuration or not change it. The resulting current then gives away its initial state. Due to the lower voltage drop along the longer paths, the surrounding elements are not switched.

Let us assume the switch is in 0-state, and a reading pulse shifts it into an on-on configuration. For the exemplary numbers used before, this results in the reading current $I_{\text{read}}^0 = I_{\text{element}} + I_{\text{sneak}} = V/2R_{\text{on}} + V/3R_{\text{off}} \approx V/2R_{\text{on}}$. If on the other hand, it is in the 1-state initially, the reading pulse does not change the configuration and the resulting current is $I_{\text{read}}^1 = V/R_{\text{off}} + V/3R_{\text{off}} = 4/3R_{\text{off}}$. This yields a resolution $I_{\text{read}}^1/I_{\text{read}}^0 \approx R_{\text{off}}/R_{\text{on}}$, the ratio between the off and on-state of a single element. Hence, the reading resolution for the CRS is far better than for the basic binary switch, and the current and associated energy dissipation through sneak paths around it are drastically reduced. This enhancement of stability and power consumption makes the CRS feasible for the realization of large memory arrays. As such, the concept has since been picked up by various works, see e.g. [3, 20, 98, 183, 193], and will be an important ingredient in the models of our subsequent investigations.

Another very interesting application of resistive switching is so called **neuromorphic computing**. Artificial neural networks are increasingly used to solve complex machine learning tasks such as pattern recognition. They use massive parallel processing in a way that is resembling neural networks in animals. A recent approach is to implement such processes directly in hardware, a task for which ReRAM elements are well suited for [71, 76, 169].

The human and animal nervous system represents the most successful physical realization for processing information, far more powerful and efficient than any digital computer based system[1]. It is a network of interconnected neurons, each of which is basically made up out of three parts: a soma, an axon and the dendrites. The soma contains the cell nucleus, the highly branched dendrites collect signals by other neurons, and the axon receives the signal produced by the soma and transmits them to other neurons. Synapses form the connections in between neurons, they propagate spikes, or action potentials, from a presynaptic neuron to a postsynaptic neuron.

[1] Depending on the task at hand of course, computers are better at fast calculations with floating point numbers. Or at beating their human opponents in the television quiz show *Jeopardy!*. For that task IBM's Watson computer had a power consumption of about $85kW$ however, compared to a humans brains' frugal $20W$ [60].

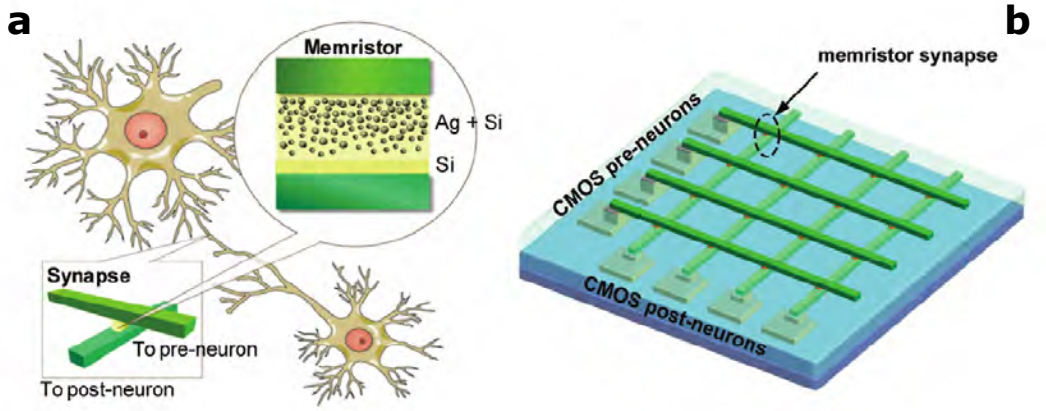

Figure 6.3.: Emulating synaptic plasticity with ReRAM. **a** Conceptual illustration of using ReRAM as synapses between neurons. The insets show the schematics of the two-terminal device geometry and the layered structure of the resistive switch (therein labelled memristor). **b** Schematic of a neuromorphic pattern with CMOS neurons and memristor synapses in a crossbar configuration. Graphic taken from [76].

This means, that the neuron before the synapse transmits the signal to its axon, and the spike is received by the dendrites of the neuron after the synapse. Now, learning is performed by changing the synaptic weight between neurons, i.e., the strength of their coupling. These operations are performed on a massively parallel and distributed scale.

The underlying idea of neuromorphic computing is to consider ReRAM elements or small circuits of them as artificial synapses [169], cf. Fig. 6.3. It makes use of the non-volatility as well as a property of RS devices that is called multilevel switching [2, 10, 117, 151], in which the resistive state can take several values. This tunable resistive state of the ReRAM cell can then be used to emulate the synaptic weight. Updating the weight of the synapses changes the communication between the pre-neuron (before the synapse) and the post-neuron (after the synapse). This way, learning processes such as pattern recognition can be modeled [76].

6.3. Theoretical Background: the Memristor as the Fourth Basic Passive Circuit Element

The conceptual background behind resistive switching is the memristor, an element whose resistance is determined by its memory of the current that has flown through it. Hence its name, a portmanteau of memory and resistor. The existence of

the memristor as the fourth basic passive circuit element, besides the resistor, the capacitor and the inductor, has been proposed by L. O. Chua in his seminal paper [25] almost 50 years ago.

The already known circuit elements are defined by differential relation; the ideal capacitor relates the charge $q(t)$ and the voltage $V(t)$ by $\mathrm{d}V = \mathrm{d}q/C(q)$ with the capacity $C(q)$. The resistor relates the current $I(t)$ and the voltage: $\mathrm{d}V = R(I)\mathrm{d}I$. Finally, the ideal inductor relates the voltage flux[2] $\phi(t)$ to the current via $\mathrm{d}\phi = L(I)\mathrm{d}I$. Additionally, the charge and current are connected as a time derivative, $\mathrm{d}q/\mathrm{d}t = I$, and so are the voltage flux and the voltage $\mathrm{d}\phi/\mathrm{d}t = V$.

So far, a connection between the charge and the voltage flux is missing. To preserve the symmetry of this structure, Chua proposed that the electric charge and voltage flux should constitute a fourth relationship $\mathrm{d}\phi = M(q)\mathrm{d}q$ via the corresponding new circuit element which he called **memristor**. Obviously, the memristance has the dimension of electrical resistance. These connections can be seen in Fig. 6.4. Alternatively, they can be expressed by implicit relations [52],

$$f_R(V, I) = 0 \qquad \text{for the resistor,} \tag{6.1}$$
$$f_C(V, q) = 0 \qquad \text{for the capacitor,} \tag{6.2}$$
$$f_L(\phi, I) = 0 \qquad \text{for the inductor,} \tag{6.3}$$

and

$$f_M(q, \phi) = 0 \qquad \text{for the memristor.} \tag{6.4}$$

Hence the memristor is a two terminal electronic device defined by the relationship between charge and flux, which will determine the input-output behavior of the voltage and current. The latter quantities do not characterize the memristor, but are more easily accessible experimentally.

We proceed by showing that although the left- and right-hand-side of the resistor relation $\mathrm{d}V = R(I)\mathrm{d}I$ are time derivatives of the memristor relation $\mathrm{d}\phi = M(q)\mathrm{d}q$, both quantities are fundamentally different. We assume an **ideal** and **passive** memristor, meaning that its $q - \phi$ curve has the attributes: unique, nonlinear, continuously differentiable and strictly monotonically increasing.

[2] The voltage flux, also called the flux linkage, is a property of a two terminal device, defined as $\phi(t) = \int^t V(\tau)\mathrm{d}\tau$, where $V(t)$ is the potential difference between the two terminals. It is not precisely identical to the magnetic flux ϕ_B, a point of much confusion in the literature. The magnetic flux is defined as the total magnetic field $\boldsymbol{B}$ passing through a surface S around the device, $\phi_B(t) = \int_S \boldsymbol{B}(t) \cdot \mathrm{d}\boldsymbol{S}$, according to Faradays law of conduction. While both are identical for simple systems such as the inductance in a loop of wire, in case of the memristor they are not [35]. Its internal electric field is not negligible, and the flux linkage related energy is dissipated in form of Joule heating instead of being stored in a magnetic field.

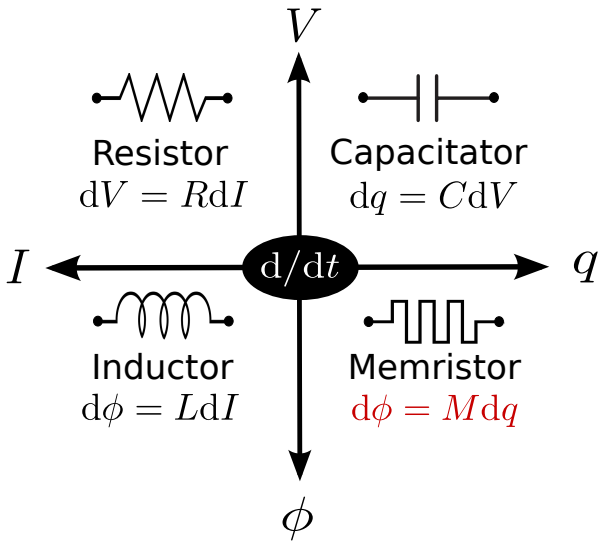

Figure 6.4.: The basic electric quantities current I, voltage V, charge q and voltage flux ϕ and their connections via the four elementary passive circuit elements: resistor, capacitor, inductor and memristor.

For a memristor without explicit time dependence, the time derivative of the constitutive relation eq. (6.4) yields

$$\frac{\mathrm{d}f_M}{\mathrm{d}t} = \left(\frac{\partial f_M}{\partial \phi}\right)_q \frac{\mathrm{d}\phi}{\mathrm{d}t} + \left(\frac{\partial f_M}{\partial q}\right)_\phi \frac{\mathrm{d}q}{\mathrm{d}t} = 0. \tag{6.5}$$

This is used to obtain the expression

$$V = -\frac{\left(\partial f_M/\partial q\right)_\phi}{\left(\partial f_M/\partial \phi\right)_q} I(t) =: M(q,\phi)I(t), \tag{6.6}$$

which defines the memristance in terms of its constitutive function f_M. Due to the assumed passivity of the device, the q-ϕ curve must be a strictly monotonically increasing function. This is seen by looking at the dissipated power, $\mathrm{d}P = \mathrm{d}VI = M(q,\phi)\mathrm{d}I^2/2$, which is only always larger or equal to zero, if M has those properties (cf. [25] for details). Hence, q and ϕ each can be expressed as a function of the other, i.e., $q = q_M(\phi)$ and $\phi = \phi_M(q)$. This delivers the distinction between current and voltage driven memristor. In the current driven case, we express ϕ in terms of q and, with only one free variable remaining, eq. (6.6) can be rewritten

$$V = M\left(q_0 + \int_0^t I(\tau)\mathrm{d}\tau\right) I(t). \tag{6.7}$$

The memory of the memristance is expressed via the time integral in its argument. On the other hand, from the resistor's constitutive relation we gain

$$\mathrm{d}V = -\frac{(\partial f_R/\partial I)_V}{(\partial f_R/\partial V)_I}\mathrm{d}I(t) =: R(I,V)\mathrm{d}I(t), \tag{6.8}$$

and therefore

$$V = R_0 + \int_0^I R(\iota)\mathrm{d}\iota. \tag{6.9}$$

Comparison of eqs (6.6) and (6.9) shows that both are clearly different, while the memristance depends on the past course of the current, as indicated by the time integral, the resistance does not. Nonlinearities are allowed though; in case of a linear dependence it reduces to Ohm's law $V = RI$.

Hence the memristor is governed by the equations $V(t) = M(w(t))I(t)$ and $\mathrm{d}w(t)/\mathrm{d}t = I(t)$. Since the direction of the current will follow that of the voltage, we generally expect a Lissajous figure for the $V - I$ characteristics. However, nobody has been able to propose a model device which follows these simple equations [173].

Later on Chua and Kang [27] generalized their initial proposal to **memristive systems**, in which the requirement of a sole dependence of the memristance of the charge is loosened, and a further internal dynamics is allowed. Such a system is characterized by

$$V(t) = M(t)\left(w(t), I(t)\right) I(t) \tag{6.10}$$

$$\frac{\mathrm{d}w(t)}{\mathrm{d}t} = f\left(w(t), I(t)\right), \tag{6.11}$$

where $w(t)$ describes a set of internal state variables and f is a yet unspecified function of the internal state variable and the electric current. As we will see in the following chapter, a phenomenological approach that satisfies eq. (6.11) has been proposed since then for titanium dioxide based resistive switching.

6.4. The HP-memristor

The 'standard' model of the memristor was introduced by Strukov et. al. at Hewlett Packard (HP) Labs together with the experimental realization [173]. It is composed as follows: a transition metal oxide, titanium dioxide, is sandwiched between two electrodes. Due to the electric field that is induced in the device by the external voltage $V(t)$, oxygen vacancies acting as dopants begin to drift within the device. This way, they change the resistance of the area they are in. Following the established terminology of the field, this device is a bipolar memristor. Due to the activation by an electroforming mechanism, only of the electrodes constitutes the area where the resistive switching process occurs.

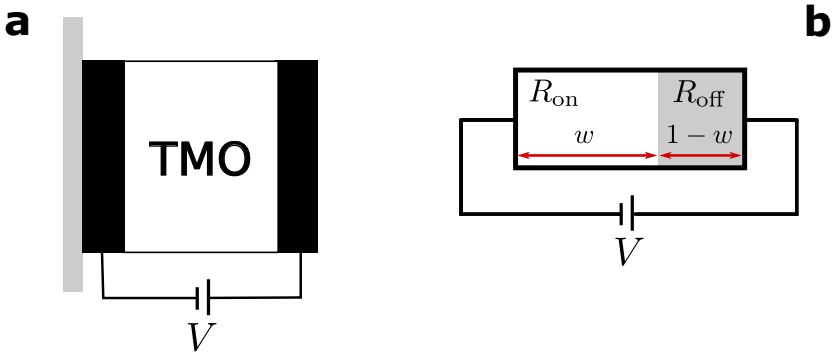

Figure 6.5.: a Basic layout of a resisting switching device. It is composed of two metal electrodes (black), between which a TMO (or solid electrolyte) is sandwiched. An external voltage can be applied. The device is grafted onto a substrate (grey), with no influence on the function. **b** The HP-memristor is modeled as a linear interpolation between two resistors with low (R_{on}) and high (R_{off}) resistance. The position w of the variable boundary between them moves proportionally to the applied current. Depicted for memristor of unit length $D = 1$.

For its description, a linear interpolation of two resistors with resistances R_{on} and R_{off} connected in series is assumed. The movable boundary w between them determines the influence of both parts on the total resistance. We solve this for the time dependent expressions of the charge q and voltage flux ϕ. The memristance[3] is given by

$$R(w) = \frac{w}{D} R_{\text{on}} + \left(1 - \frac{w}{D}\right) R_{\text{off}}, \tag{6.12}$$

where D is the size of the device and accordingly $0 \leq w \leq D$. The extremal values of the boundary position w set the memristor in the on- or in the off-state. Hence, w is the state variable of the HP-memristor, it determines the logical state and represents the memory of the system. The basic setup is illustrated in Fig. 6.5.**b**

We can further divide eq. (6.12) by R_{off}, revealing that the reduced memristance $R(w)/R_{\text{off}}$ in this model depends only on two values: the resistance ratio $R_{\text{on}}/R_{\text{off}}$ and the reduced position w/D. The position of the boundary is determined by the charge, its motion accordingly by the current,

$$\frac{\mathrm{d}w(t)}{\mathrm{d}t} = \frac{\mu_D R_{\text{on}}}{D} I(t) = \frac{D}{q_0} I(t). \tag{6.13}$$

Here, μ_D denotes the ion mobility. It is collateralized with the material constants into

$$q_0 = \mu_D R_{\text{on}} / D^2, \tag{6.14}$$

[3] In order to maintain the convention in [173], which is also generally used in the literature, we use the abbreviation R for the memristance from now on. Also, we will use the term resistance interchangeably with memristance.

which is interpreted as the maximum charge that can assemble in the device before saturation (i.e. by moving w from 0 to D).

We remark that this expression needs to be thought of as supplemented by an additional window function, $f(w)$, which incorporates the limitation of w. Once w reaches either 0 or D, it is no further incremented until the motion reverses. Also, the memristor variables do not change anymore, if w is not incremented, neither is ϕ or q. In the original implementation [173]

$$f(w) = \Theta(w) - \Theta(w - D) \tag{6.15}$$

is chosen, where $\Theta(x)$ denotes the Heaviside step function. Various investigations have been devoted to suggesting alterations of eq. (6.15) [14, 15, 30, 78, 137, 162]. The effect of these different window functions is a differentiation of the boundary variable's movement speed in the bulk and near the electrodes, or additionally for the direction of the driving. See also [8, 109] for comparisons of simulations with the different window functions.

With the initial boundary position value w_0, integration of eq. (6.13) yields

$$\frac{w(t)}{D} = \frac{w_0}{D} + \frac{q(t)}{q_0}. \tag{6.16}$$

By entering eq. (6.16) into eq. (6.12), we obtain an explicit expression of the memristance in terms of the charge,

$$R(q) = R_0 - (R_{\text{off}} - R_{\text{on}})\,\frac{q}{q_0}, \quad \text{with} \quad R_0 = \frac{w_0}{D} R_{\text{on}} + \left(1 - \frac{w_0}{D}\right) R_{\text{off}}. \tag{6.17}$$

Using $\mathrm{d}\phi/\mathrm{d}t = R(q)\mathrm{d}q/\mathrm{d}t$, we pull the derivation operator in front of the right hand side and after time integration with the boundary conditions $q(t = 0) = 0$ and $\phi(t = 0) = 0$ follows

$$q(t) = \frac{q_0 R_0}{R_{\text{off}} - R_{\text{on}}} \left(1 - \sqrt{1 - \frac{2(R_{\text{off}} - R_{\text{on}})}{q_0 R_0^2}\phi(t)}\right), \tag{6.18}$$

and

$$I(t) = \left(1 - \frac{2(R_{\text{off}} - R_{\text{on}})}{q_0}\phi(t)\right)^{-\frac{1}{2}} \frac{1}{R_0} V(t). \tag{6.19}$$

From the expression (6.18) we can tell that the underlying $q(\phi)$-relation is not affected by the signal form, amplitude or frequency of the voltage driving. However, different ranges of the set of (q, ϕ) values may be visited. Especially, if the signal is strong enough to bring the memristor variable w to either boundary, the initial value R_0 is forgotten.

In contrast to that, eq. (6.19) implies that the hysteresis in the implicit current-voltage curves increases with the period and amplitude of the voltage signal.

In order to simulate the dynamics of this device, we employ the parameter set used by [173]. Hence we have an ion mobility of $\mu_D = 10^{-14} m^2/Vs$, a resistance ratio $R_{\text{on}}/R_{\text{off}} = 0.05$, so for example $R_{\text{on}} = 100\Omega$ and $R_{\text{off}} = 20k\Omega$, and a device size of $D = 10^{-8} m$. Further parameters are the period $T = 10ms$ and amplitude $V_0 = 1V$ of the driving signal. These parameters give a maximal charge of $q_0 = 10^{-4} C$ that the device can hold.

In Fig. 6.6 the systems dynamics is shown in response to a sinusoidal voltage input,

$$V(t) = V_0 \sin(\omega_0 t) = V_0 \sin\left(\frac{2\pi}{T} t\right). \tag{6.20}$$

The time dependence is depicted for T_{c}, which is the characteristic period for which the device is just completely charged (i.e., from 0 to q_0) during the positive voltage half-cycle. It follows by $\phi_{\max} = \int_0^{T_c/2} V(t) = V_0 T_c/\pi$ and demanding for eq. (6.18) $q(T_c/2) = q_0$. One obtains

$$T_{\text{c}} = \frac{\pi q_0}{2V_0} \left(R_0 - \frac{1}{2}\left(R_{\text{off}} - R_{\text{on}}\right)\right). \tag{6.21}$$

Equivalently, we can say that this is where w extends to its full range of motion between both boundaries if $R_0 = R_{\text{off}}$ and hence $w_0 = 0$. The current reply in this case has the form of a ratchet like curve, with a sharp reversal when the sign of the voltage changes from plus to minus, and a smoother transition the other way around.

The current over voltage plot reveals the expected Lissajous figure with zero crossing. For $T < T_{\text{c}}$, these figures are point symmetrical to the origin, and the area under the curves increases with T. Put differently, we can say that the hysteric effect of resistive switching vanishes with large frequencies $\omega = 2\pi/T$, because the system is too sluggish to reply. For $T > T_{\text{c}}$ on the other hand, the system reaches its extremal position before the voltage reverses. Here, the window functions eq. (6.15) cuts off any further iteration, the system will no longer reply and the symmetry is lost. This loss of symmetry is mirrored in the resistance over voltage plots, Fig. 6.6.**d**.

Also, the predicted $q - \phi$ curves emerge. They do not differ for the different periods T, but the interval run on the curves increases with T, until T_{c} is reached, from where on the window function cuts iteration again. We remark that these curves would not coincide perfectly if we had started with $R_0 < R_{\text{off}}$.

Summary

In the current chapter, we have introduced the physical background and applications of resistive switching for non-volatile resistive memory. ReRAM can be used as a

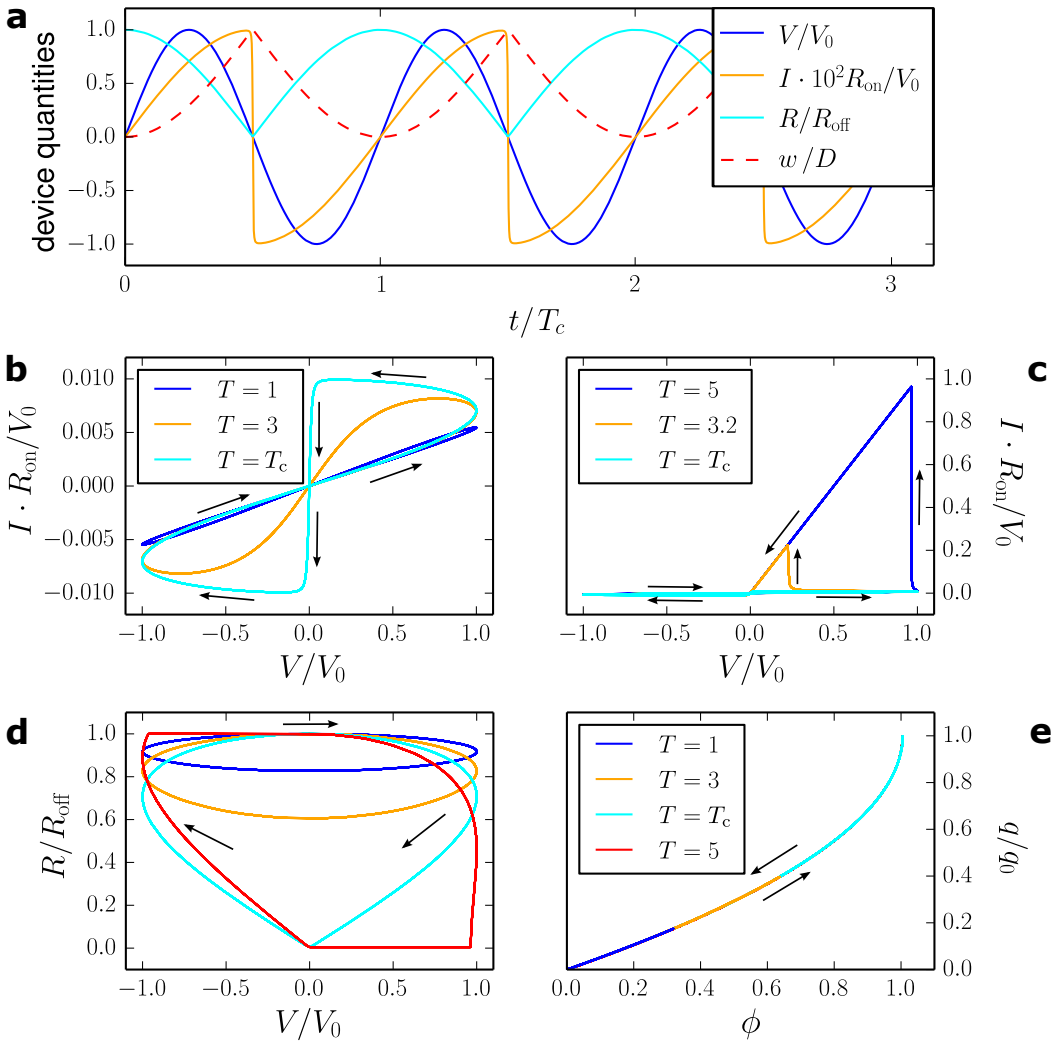

Figure 6.6.: Dynamics of the HP-memristor driven by a sinusoidal voltage **a** time evolution of V, I, R and w for $T = T_c$. For this driving period, the interpolation variable w just reaches both ends, 0 and 1 and we recognize a ratchet-like shape of the current. **b** Current over voltage plot for driving periods below the characteristic period T_c and **c** above it. The arrows indicate in which direction the curves proceed with increasing time. Once $T > T_c$, the current magnifies by several orders of magnitudes. All curves have the form of a Lissajous figure. **d** Resistance over voltage. Once $T > T_c$, the curves loose their left-right symmetry. **e** Charge over voltage flux. For all T, the curves coincide, albeit for $T < T_c$, their length is shorter. $T = 5$ is concealed by $T = T_c$, since the window function cuts of further increments in the range of ϕ. All simulation results overlap with the analytical expressions eqs. (6.16)-(6.19) in perfect accordance.

CRS in highly integrated memory stackbars; or to model artificial synapses. Also, the concept of the memristor was explained, and a model for a RS-device exhibiting memristive properties was presented: the HP-memristor. In the following chapters we will investigate more complex models of RS, first by expanding upon the HP-memristor to account for the CRS, and afterwards by considering a mesoscopic model which incorporates fluctuations of its state variables.

7. A Nonlinear HP-Type Complementary Resistive Switch

The realization of memory elements in 3d stackbars leads to high integration densities. In order to prevent the occurrence of sneak paths therein, the anti-serial combination of two RS-elements to a single cell is feasible, the complementary resistive switch. However, this cannot be done for the standard HP-memristor, as both elements behavior would cancel each other out. Motivated by the irregular shape of the filament that is protruding into the device after the initial electroforming, and in which the switching process takes places, we suggest a nonlinearity in the resistance-interpolation function, characterized by a single parameter p. Thereby the original HP-memristor is expanded upon. We numerically simulate and analytically solve this model. Further, the nonlinearity allows for its application to the CRS.

7.1. Introduction

As we have established in section 6.2, the main application of resistive switching is ReRAM. On an industrial scale, it is implemented by stacking upon one another 2d grids of wires to multiple levels, with an RS element connecting each wire pair of two subsequent levels. This way, enormous integration densities can be reached. Alongside high integration however, sneak paths arise and become a major problem due to read failures and heat dissipation. To address these issues, an anti-serial alignment of two RS-elements to a CRS was introduced. This greatly reduces the sneak currents, as one of the elements is always in a high resistive state.

It is however not possible to describe such an element by the HP-memristor of section 6.4. Effectively, the HP-memristor can be regarded as two different resistors in a row, whose interpolation weights are determined by the border position w. The border moves proportionally to the current that flows through the device[1], cf. eq. (6.13). In an anti-serial alignment of two HP-memristors in a CRS scheme, both of its elements behavior will neutralize each other. This can be easily seen by adding the resistances eq. (6.12) for one element with the boundary at $w(t)$ and one at

[1] A nonlinear contribution of the current in the switching kinetics eq. (6.16) enables the realization of a CRS as well, without the need for a nonlinear interpolation of the resistances as proposed in this chapter. See for example nonlinear ion drift models [99, 144, 163] or tunnel barrier models [135, 164]. However, generally such models are not analytically treatable. Or the memristor properties are lost, since the device is not switched only by the area under the voltage curve, but by its course.

$D - w(t)$, $R(w(t)) + R(D - w(t)) = R_{\text{on}} + R_{\text{off}}$, in which the dynamic variable $w(t)$ does not appear anymore.

Physically, a single RS-cell consists of a transition metal oxide (TMO) like titanium dioxide [53, 98, 173, 191] or manganites [22, 70] sandwiched in between two electrodes, or electrochemical metalization cells [108, 180, 184, 196], for which one of the electrodes must be electrochemically active. Prior to normal operation, a conducting filament that permeates the cell is created during an electroforming process [72], it may be build either by a metallic filament made up of the atoms of the active electrode or by a well-conducting oxygen deficient region. The final bridge to the opposite electrode is the active zone where the switching occurs, it is opened and closed depending on the sign of the applied voltage.

Classically, a sheet resistance of a flat conductor with length D, breadth B and resistivity R_{on} is given by $R = R_{\text{on}} \cdot D/B$. We cannot expect the bridge to be a rectangle however, rather it might be some ill-defined wedge-like or pyramidal structure [53, 101, 184, 192, 196], see Fig. 7.1 or consist of several fused channels [49].

Motivated by this background, we aim to extend the original HP-memristor to gain an analytically solvable memristor model for the CRS. Therefore we first introduce a nonlinearity in the weighting of the high and low resistance parts of the HP-memristor in section 7.2. Its behavior under a sinusoidal voltage driving is investigated in detail, and solved analytically. In section 7.3 we serially connect two of these novel memristors with counter oriented polarities to a CRS. We will simulate and analytically calculate its response to the voltage driving, and investigate its dissipative loss with regard to the nonlinearity parameter p.

7.2. A Nonlinear HP-Memristor.

Accounting for the geometric structure of the bridge, we regard the sheet resistance as an integral over the various slices, whose breadth depends on their position. With the boundary w running from 0 up to the device length D, the bridge resistance is given by $R(w) = R_{\text{on}} \int_0^w 1/B(x)\mathrm{d}x$, some general non-linear function. We accordingly set for our model

$$R\Big(w(t)\Big) = R_{\text{on}} \left(\frac{w(t)}{D}\right)^p + R_{\text{off}} \left(1 - \left(\frac{w(t)}{D}\right)^p\right), \tag{7.1}$$

with the parameter of nonlinearity p. The schematics is shown in Fig. 7.1 for $p < 1$, corresponding to a filament that is narrowing towards the passive electrode. In this case, as the filament builds up, the broad base is created first, resulting in a lower resistance at identical length compared to the rectangular filament ($p = 1$). This is reflected by eq. (7.1). On the other hand $p > 1$ corresponds to a filament that is widening towards the passive electrode. Here, the narrow parts of the filament

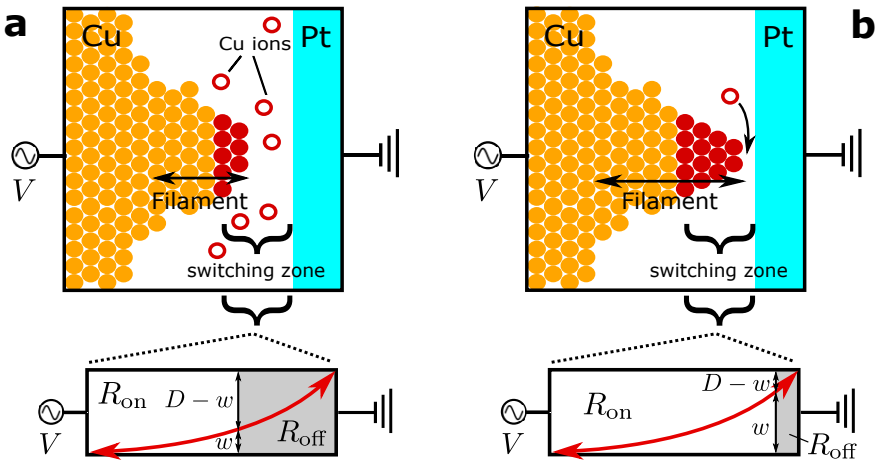

Figure 7.1.: 2D schematic of the atomic bridge in a cuprate RS-device at different stages (top panels), and its connection to the boundary variable w in the nonlinear HP-memristor (bottom panels). After electroforming a filament of Cu-Atoms protrudes from the cuprate to the platinum electrode. At its end, near the platinum electrode, the switching occurs (indicated by red colored Cu atoms and ions). **a** The bridge is disrupted by the ionization of its cuprate atoms in the switching zone, hence only a small distance w of the gap is still brigded and has low resistance, while the larger part has high resistance. **b** The conducting bridge is rebuilt by the last copper ion condensating into the gap. Accordingly, most of the distance has low resistance. The red line in the nonlinear HP-type memristor, indicates how the position w determines the relative sizes of the areas with low (white, $\propto (w/D)^p$) and high (grey, $\propto 1-(w/D)^p$) resistance, which correspond to the areas with condensed and free ions of the switching zone.

with a higher resistance contribution are build first. As for the HP-memristor, cf. eq. (6.13), the internal variable reacts to the applied current

$$\frac{\mathrm{d}w(t)}{\mathrm{d}t} = \frac{D}{q_0} I(t). \tag{7.2}$$

Here q_0 denotes the total charge accumulated while moving $w = 0$ to $w = D$, it is connected to the material constants by $1/q_0 = \mu_D R_{\mathrm{on}}/D^2$ with the ion mobility μ_D. Also identical to section 6.4, this expression needs to be thought of as being supplemented by an additional window function, $f(w)$, cf. eq. (6.15). It incorporates the limitation of w. Once w reaches either 0 or D, it is no further incremented until the motion reverses, neither are the memristor variables q and ϕ.

The advantage of our nonlinearity modification is that it remains simple enough to be solvable. Analogous to the solution of the HP-memristor, we obtain for a single nonlinear element

$$R\Big(q(t)\Big) = R_{\text{on}} \left(\frac{q(t)}{q_0}\right)^p + R_{\text{off}} \left(1 - \left(\frac{q(t)}{q_0}\right)^p\right), \tag{7.3}$$

with the initial position $w_0 = 0$ as boundary condition. Other w_0 can be incorporated into eq. (7.3) by substituting the charge $q \to q + q_0 w_0 / D$.

Using Ohm's law

$$V = R\mathrm{d}q/\mathrm{d}t, \tag{7.4}$$

the time derivation operator is put in front of the entire right hand term according to $(a+q)^p \mathrm{d}q/\mathrm{d}t = \mathrm{d}(a+q)^{p+1}/(p+1)\mathrm{d}t$, yielding

$$V\left(q(t), \dot{q}(t)\right) = \frac{\mathrm{d}}{\mathrm{d}t}\left(R_{\text{off}} q(t) + \frac{R_{\text{on}} - R_{\text{off}}}{p+1} q_0 \left(\frac{q(t)}{q_0}\right)^{p+1}\right), \tag{7.5}$$

which by time integration gives the voltage flux of the device as a function of the time dependent charge. With the boundary condition $\phi\left(q = 0\right) = 0$ we gain

$$\phi\Big(q(t)\Big) = R_{\text{off}} q(t) - \frac{R_{\text{off}} - R_{\text{on}}}{p+1} q_0 \left(\frac{q(t)}{q_0}\right)^{p+1}, \tag{7.6}$$

the bijective relationship constitutive for memristive systems.

Let us investigate the behavior of the system. For the purposes of the simulation, we choose the same parameters as in section 6.4.

Fig. 7.2 depicts the system properties for several nonlinearity parameters p and driving periods T. The latter is chosen to be the characteristic period $T_c^{(p)}$ for some p, which is defined analogously to that in of the HP-memristor eq. (6.21) as the characteristic driving period that is needed to fully charge the memristor. Then together with the initial boundary position $w_0 = 0$ one obtains from eq. (7.6)

$$T_c^{(p)} = \frac{\pi q_0}{V_0} \left(\frac{p}{p+1} R_{\text{off}} + \frac{1}{p+1} R_{\text{on}}\right). \tag{7.7}$$

Apparently, the characteristic period (cf. Fig. 7.2.**a**) increases monotonously with p, hence for nonlinearities $p \to 0$ the device switches fastest. This corresponds to the physical case of a filament with a large base getting thinner near the end, presumably also the relevant physical case [49, 196]. As special case for $p = 1$, eq. (6.21) follows.

As we see in Fig. 7.2.**b** for several nonlinearities, while all describe slightly different memristors, the $\phi - q$ relation remains bijective, as also implied by eq. (7.6). For small p less voltage flux is needed to reach q_0.

In Fig. 7.2.**c** the time courses of the electrical properties are shown for an characteristic driving $T = T_c^{(p=1)}$. At the end of the positive voltage half-cycle w just reaches its extremal position, associated with a minimum of the resistance. In case of

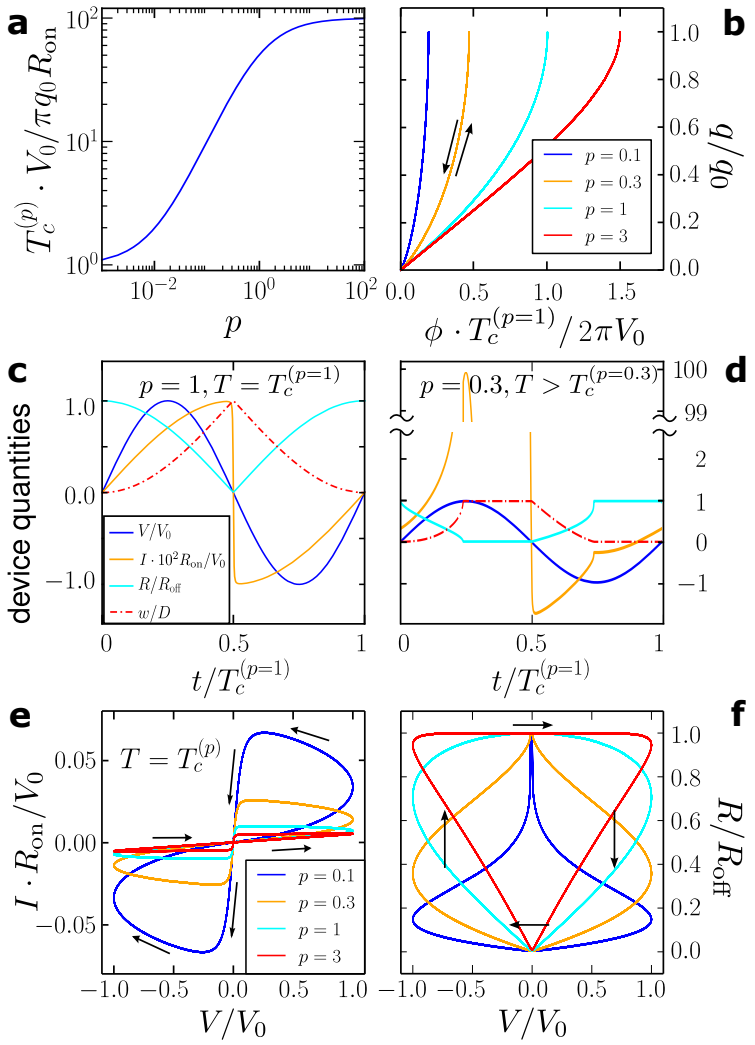

Figure 7.2.: Dynamic behavior of a single nonlinear HP-type memristor. **a** Characteristic driving time as a function of the nonlinearity. **b** Associated charge over voltage flux plots. **c** , **d** Time course of the device quantities R, I, w and V. **e** Current over voltage plots, driven by signal with period $T = T_c^{(p)}$. **f** Resistance over voltage plot for various p, each for driving period $T = T_c^{(p)}$. Shared legends for (**a**, **b**), (**c**, **d**) and (**e**, **f**).

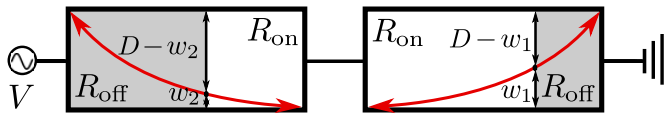

Figure 7.3.: Setup to realize bipolar resistive switching with two nonlinear HP-type memristors in anti-serial order.

driving times beyond the characteristic period $T = T_c^{(p=1)} > T_c^{(p=0.3)}$, Fig. (7.2.**d**), w saturates before that, and consequently the current spikes as the voltage still increases.

In the $V - I$ diagram for $T = T_c^{(p)}$ (Fig. 7.2.**e**), i.e. at each respective characteristic time, we see the pinched hysteresis loops that are the fingerprint of memristive systems [26]. The area enclosed by the hysteresis cycles increases with smaller p. This shows in the $R - V$ diagram of Fig. 7.2.**f** by a curve that transforms from being triangularly shaped to one resembling an onion, with the average resistance falling with smaller p.

7.3. The CRS Composed of Two Nonlinear HP-Memristors

In the next iteration, we consider two memristors connected in a row with counter oriented polarities. This setup is rendered possible only by the nonlinearity in the w-dependence of the resistance (cf. eq. (7.1)), since otherwise (i.e. $p = 1$) both elements' behavior just cancels each other out. Conceptually, this represents realizations with both an implementation of two RS-elements with one active zone each and one element that has active zones near both electrodes [98, 108, 191]. Let the two domain boundaries be denoted by w_1 and w_2. The resistance is now simply given by the sum of the individual contributions,

$$R_{\text{CRS}}\Big(w_1(t), w_2(t)\Big) = R\Big(w_1(t)\Big) + R\Big(w_2(t)\Big). \tag{7.8}$$

The response of each memristor to the current flow is not altered, i.e. still governed by eq. (7.2), albeit with a minus sign for the second element. This layout is illustrated in Fig. 7.3. Since we have two elements in a row, the voltage drop at each is proportional to its resistance and in extension, so is the voltage flux ϕ.

For the first element $\phi_1(q)$ is given by eq. (7.6), whereas for the second we have to incorporate the reversed polarity as well as the boundary conditions $w_0^{(2)} = D$ and $\phi(q = 0) = 0$, yielding the flux $\phi_2(q) = \phi(q_0) - \phi(q_0 - q)$. Addition of both gives the total flux,

$$\phi_{\text{CRS}}\Big(q(t)\Big) = 2R_{\text{off}}q(t) - \frac{R_{\text{off}} - R_{\text{on}}}{p+1} q_0 \left(\left(\frac{q(t)}{q_0}\right)^{p+1} + 1 - \left(1 - \frac{q(t)}{q_0}\right)^{p+1} \right). \tag{7.9}$$

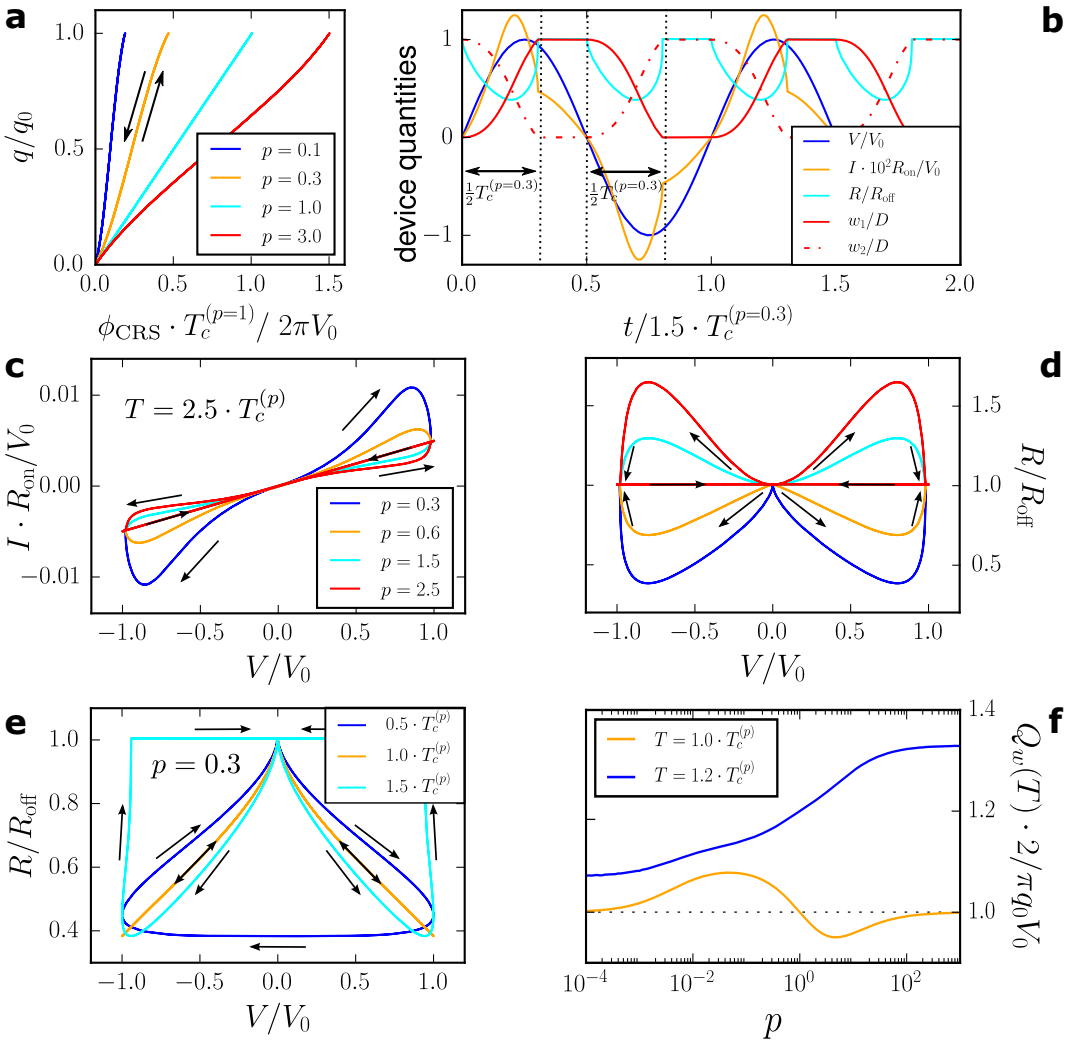

Figure 7.4.: Dynamic behavior of CRS composed of nonlinear HP-type memristors. **a** Charge over voltage flux for several nonlinearity parameters. **b** Time dependence of system quantities for $p = 0.3$ and driving period $1.5 \cdot T_c^{(p=0.3)}$, the two half cycles of the corresponding characteristic period are indicated by the double headed arrow. **c** Current over voltage and **d** resistance over voltage plots for various nonlinearities p, each driven by signal with period $2.5 \cdot T_c^{(p)}$, shared legend for (**c**, **d**). **e** Current over voltage plot for $p = 0.3$ and various driving periods. **f** Heat dissipation Q_w during one switching operation.

The term in parentheses of eq. (7.9) has a functional dependence on the charge q of the order p. Hence for $p = 1$, this gives $\phi_{\text{CRS}}(t) = (R_{\text{off}} + R_{\text{on}})q(t)$, the linear $q - \phi$ relation of a constant resistor. We note that from the functional form of eq. (7.9) that the $\phi - q$ relation remains bijective. This is straightforward, since the combination of memristors must yield another one [25]. As expected, each nonlinearity parameter describes a different memristive system with a relation complying to eq. (7.9), Fig. 7.4.**a**. For smaller p less voltage flux ϕ is needed to charge the memristor. We can hence see it as more reactive with smaller p, or put differently, its average resistance over a voltage cycle is lower, cf. Fig. 7.4.**e**.

In comparison with the characteristic period for a single nonlinear element eq. (7.7), we find that for the CRS it simply doubles, since the voltage flux counts separately for each of the elements. Hence

$$T_c^{(p)} = \frac{2\pi q_0}{V_0}\left(\frac{p}{p+1}R_{\text{off}} + \frac{1}{p+1}R_{\text{on}}\right). \tag{7.10}$$

In Fig. 7.4.**b** some system reply properties are shown for a single value of p. Within each half cycle of the driving, somewhere before the voltage peak the resistance drops once, accompanied by a spike in the current. This is due to the inherent symmetry of the device. Assuming that the first element is in the off-state and the second in the on-state, a positive voltage will now move the first switch in the on-state and the second in the off-state, with both configurations having the same resistance. However, in the course of that both will be in an intermediate state in which the resistance drops (for $p < 1$). The same happens the other way around with the negative voltage half cycle. Hence the doubling of the frequency of the reply quantity R. It is mirrored in the $R - V$-plots shown in Fig. 7.4.**c** and Fig. 7.4.**e** by the axis symmetry with respect to the driving voltage.

Further investigating the resistance course for various driving periods, Fig. 7.4.**c**, reveals a behavior resembling a single element for $T < T_c^{(p)}$, cf. Fig. 7.1.**e**. For the characteristic driving $T = T_c^{(p)}$ on the other hand the course is given by two bidirectional paths without hysteretic spread. This can be attributed to the symmetry of the device and the voltage signal. At $V(t = T_c^p/4) = V_0$ both borders are in the middle position $w_1 = w_2 = D/2$ meaning that the nonlinear curves governing the resistance (cf. Fig 7.3) look the same for the forward and backward motion. Finally, for $T > T_c^{(p)}$ a two-legged figure appears, mirroring the frequency doubling in the reply properties already noticed in the $R(t)$-plot. It has clearly distinguished zones of high and low resistance. In compliance with experimental results for the bipolar resistive switching [22, 70, 150], this is the case of interest.

The impact of several nonlinearities on the $V - I$- and $V - R$-plots is shown in Fig. 7.4.**d-e**. We observe the pinched hysteresis loops for all. In comparison to a single element Fig. 7.2.**e**, not only are the curves symmetric to the point of origin, but also their directionalities. The area enclosed by the hysteresis loops drops for increasing

p. In the resistance plots this shows by an inversion of the legs, the symbolic legs point skywards.

Finally, we turn our attention to the dissipative loss accumulated by the system. To that end, we regard the Joule heat Q_w generated during a switching operation $0 \leftrightarrow 1$, $Q_w = \int_0^{T/2} P(t)\mathrm{d}t = \int_0^{T/2} V^2(t)/R(t)\mathrm{d}t$. Driven by the characteristic time, the result is shown in Fig. 7.4.**f**. Except for a slight variation in the middle, the heat loss for vanishing and huge p approach the same value. This asymptotic can be understood in view of the fact that for $p \to 0$, the resistance goes to $2R_{\mathrm{on}}$ (cf. Eqs. (7.1), (7.8)), whereas the characteristic time eq. (7.10) approaches $2\pi q_0 R_{\mathrm{on}}/V_0$. For $p \to \infty$ we have $R_{\mathrm{cms}} \to 2R_{\mathrm{off}}$ and $T_c^{(\infty)} = 2\pi q_0 R_{\mathrm{off}}/V_0$. Hence for both cases the integral evaluates to $Q_w = \pi q_0 V_0/2$. Given the size of the difference in Q_w, the nonlinearity is fairly secondary to the heat loss. For longer driving periods $T = 1.2 \cdot T_c^{(p)}$ on the other hand, the heat loss increases continuously with p and small p seem most beneficial.

7.4. Summary

The composite resistive switch is an essential concept for the application of resistive switches in memory. However, the HP-memristor cannot account for its behavior. Hence the goal of this section was to develop a analytically solvable CRS model. To that end we proceeded in two steps:

At first, we have developed a nonlinear alteration of the original HP-memristor. The nonlinearity reflects the irregularity of the filament structure that bridges both electrodes. For a single element we are able to reproduce all the characteristic curves and predict an increased efficiency in the switching times for nonlinearity parameters p far below 1.

In the second part, we extended this model by the anti-serial combination of two such elements. We are now able to reconstruct the reply curves of the CRS without losing analytical tractability and we can predict the behavior of the CRS with a memristive model. Thereby, the cases $p < 1$ and $T > T_c^{(p)}$ are of most physical relevance, for they reproduce the two-legged structures seen in experimental data for anti-serial bipolar switching [22, 150]. Further, here we have the advantage of faster switching and reduced dissipative heat loss in case of driving times beyond $T_c^{(p)}$.

8. Stochastic Dynamics of Resistive Switching with Two Active Zones

Any practical implementation of a resistive switching based memory cell calls for a strong miniaturization, at which point fluctuations start playing a role that cannot be neglected. A detailed understanding of switching mechanisms and reliability is essential. For this reason, we formulate a particle model based on the stochastic motion of oxygen vacancies. It allows us to investigate fluctuations in the resistance states of a switch with two active zones. The vacancies' dynamics is governed by a master equation. Upon the application of a voltage pulse, the vacancies travel collectively through the switch. By deriving a generalized Burgers' equation we can interpret this collective motion as nonlinear traveling waves, and numerically verify this result. Further, we define binary logical states by means of the underlying vacancy distributions, and establish a framework of writing and reading such memory element with voltage pulses. Considerations about the discriminability of these operations under fluctuations together with the markedness of the resistive switching effect itself lead to the conclusion, that an intermediate vacancy number is optimal for performance.

8.1. Introduction

Fluctuations in a resistive switch can appear externally and internally. They have been studied for phenomenological memristor models, such as the HP-memristor of section 6.4 whose resistance is determined by a single internal scalar variable that denotes the relative sizes of a low and high resistivity area. Internal fluctuations can be incorporated by adding white noise to this variable, [132, 171], with beneficial effects on the RS-effect, like increasing the contrast between the resistive states. External fluctuations were studied in the form of noisy impulses switching the states, and depending on the setup can either have a positive [131, 133] or detrimental effect [132]. As yet, no study of fluctuations has been conducted for a mesoscopic particle based model.

Such an approach is essential to address many characteristics of resistive switching. From experimental observations it is known that the functionality of a RS device is determined by the electrode-TMO interface and the distribution of oxygen vacancies [123, 174, 177]. In this setting, a one dimensional lattice model in which a probability distribution of the vacancies evolves depending on the external voltage and the

local resistance of each lattice site is proportional to its density of vacancies has been proposed in [150] for manganites, termed the **voltage enhanced oxygen-vacancy migration model** (**VEOV**-model) by the authors. The Schottky barriers are incorporated by enhancing the vacancies effect near the interfaces compared to their influence in the bulk, resulting effectively in a two active switching zones. Further investigation of this model showed shock-wave like behavior, [175], made plausible by the formulation of a generalized Burgers' equation for the time evolution of the vacancy distribution, which was used to predict the commutation speed of an RS-element.

Conceptually, these two active switching zones together with a more inert bulk in the middle is similar to the CRS introduced in section 6.2 and discussed in chapter 7 for the nonlinear HP-memristor. The device is symmetrical, with either half representing one of the memristors composing the CRS. Depending on the polarization of the driving pulse, the vacancies will be shifted to one interface or the other, realizing configurations with a high resistance in either state, while the drainage of one half to the other is hindered by the sluggishness of the bulk.

Hence, our goal is to describe a complementary resistive switch based on this mesoscopic model for discrete particles. We elaborate on the requirements to implement such a device, namely as a large contrast between the resistive states, and the reliability against fluctuations. For very small systems, the fluctuations will be driven by the inherent stochasticity in the motion of just a few oxygen vacancies. This lets us determine a lower limit for the possible level of miniaturization and we can predict an optimal system size for the resistive switch. We proceed as follows:

In section 8.2 we will formulate the VEOV-model for discrete particles, i.e. the oxygen vacancies. It is governed by a multivariate master equation with nonlinear transition rates. This allows us to consider not only the system dynamics depending on the parameters of the external driving, but also to further examine the fluctuations, whose magnitude is determined by the number of vacancies in the system.

Subsequently, we investigate the stochastic dynamics of the oxygen vacancies in section 8.3. Hereby, we pay special attention to the hysteretic effects, which we will quantify by the area of the corresponding hysteresis loops, and on the minimum and maximum resistances the system visits within a cycle of the periodic driving (cf. section 8.3.1). Further, we introduce continuous space and derive a nonlinear continuity equation governing the evolution of the oxygen vacancy distribution (cf. section 8.3.2). This equation can also be considered a generalized Burgers' equation, and hence the dynamics of the oxygen vacancies are interpreted as nonlinear traveling waves. Also, we successfully numerically integrate said equation to compare it with the results gained in the discrete particle picture, and show how these wave processes affect the electric properties of the device.

In section 8.4, we define the logical states of the a resistive switch with two active zones in terms of the underlying particle distributions. This allows us to express the actions of the driving voltage in these terms and develop a framework of how to

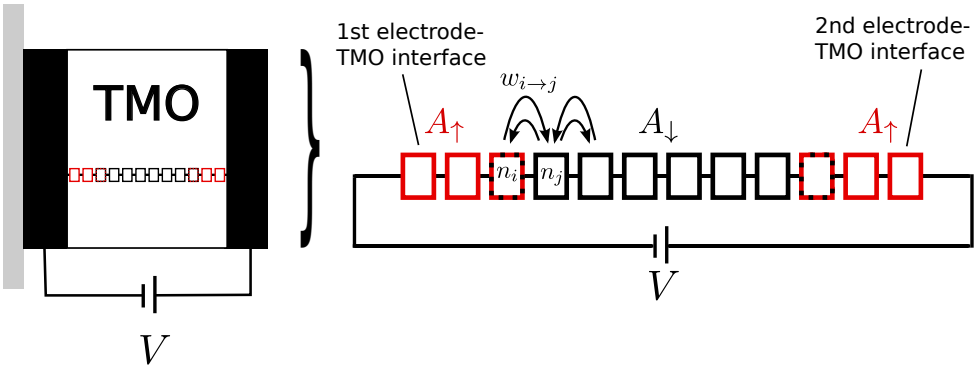

Figure 8.1.: Single RS-element consisting of a transition metal oxide electrodes on a substrate material (grey), connected to an external voltage source V. The right electrode is defined as having zero voltage. Crossing through the device is a filament of high conduction, whose behavior is responsible for the state. It is modeled as a 1d lattice with three different zones, the bulk (B) which has a small resistance factor $A_i = A_\downarrow$, and the interface zones to the electrodes on the left and right, which have large resistance factors $A_i = A_\uparrow$, with $A_\downarrow \ll A_\uparrow$. The individual sites are filled with n_i vacancies, that can hop to neighboring positions.

write and read information in the system (cf. 8.4.1). The resulting read operation is finally considered for its stability with regard to fluctuations (cf. section 8.4.2). Together with the previous results, this allows us to an predict an optimal vacancy number for the operation of the resistive switch.

8.2. A Stochastic Vacancy Hopping Model for Bipolar Resistive Switching

We base our considerations on the phenomenological VEOV-model. It focuses on the oxygen vacancy defects together with the influence of the electrode-TMO interface on bipolar switching [150]. Justified by experimental measurements showing filamentary paths of high conductance [49], the memristor is modeled as a one dimensional lattice, i.e. a network of resistors in serial order.

In transition metal oxides the oxygen vacancies affect the resistance in a complex way. On the one hand, they provide dopants and thereby facilitate conductance. On the other hand, they disrupt the TM-O-TM bonds. In order to minimize the energetic cost of the vacancies, their place is filled by free electrons from the conduction band, that are localized now in this place and have an energy level below the conduction band [126]. This resistance effect is more pronounced at the boundary of the TMO, because at a metal-insulator transition the TMO is depleted of freely moving charges, an effect that is also known as Schottky-barrier. Hence taking electrons of the

conduction band leads to a higher impact on the local resistance here.

For our investigations, the disrupting influence of the vacancies is considered, as it occurs for example in manganites [22, 70]. We assume that a specific lattice site i has N_i vacancies, every lattice site can hold a total of N_0 vacancies (with, in general, $N_i \ll N_0$), and that the resistance of that each site is proportional to its density of vacancies,

$$n_i := N_i / N_0. \tag{8.1}$$

The depletion zones at the electrode interface are taken into account by further multiplication with a resistivity factor A_i, where A_i in the bulk is small against A_i near the boundaries of the domain. As a result, the local resistance is given by

$$R_i = A_i \frac{N_i}{N_0}, \tag{8.2}$$

from which we gain the total resistance of the lattice by summation over all sites, $R = \sum_i A_i N_i / N_0$. The analytical form of A_i is given by

$$A(x) = \begin{cases} A_\uparrow, \text{ if } x < x_0 \text{ or } x > D - x_0, \\ A_\downarrow + (A_\uparrow - A_\downarrow) \left(\frac{1}{2} + \frac{1}{2} \cos\left(2\pi \frac{x - x_0}{D - 2x_0} \right) \right)^k \text{ else,} \end{cases} \tag{8.3}$$

its actual course can be seen in Fig. 8.2.**b**, where it is indicated by the dash dotted lines, for a discrete lattice of length D with $L = 100$ sites at the positions $i(x) = \text{floor}(100 \cdot x / L)$. Therein, the parameters used are $k = 20$, $x_0 / D = 0.1$ and $A_\uparrow / A_\downarrow = 100$. See also appendix A.1 for more details.

Let a configuration of lattice vacancies $(N_1, N_2, \cdots, N_L)$ be denoted by $\mathcal{N}$, and by $\{\mathcal{N}'\}$ the set of configurations that arises from $\mathcal{N}$ through a single particle hopping to a neighboring site. This results in the following master equation

$$\frac{\mathrm{d}}{\mathrm{d}t} P(\mathcal{N}, t) = \sum_{\{\mathcal{N}'\} \neq \mathcal{N}} \Big(- W_{\mathcal{N} \to \mathcal{N}'} P(\mathcal{N}, t) + W_{\mathcal{N}' \to \mathcal{N}} P(\mathcal{N}', t) \Big). \tag{8.4}$$

An external voltage at the electrodes will induce an electrical current I through the system. It can be used to determine the voltage drop over a lattice site, ΔV_i. Agitated, oxygen vacancies now move with a certain probability from one site to another, limited by the number of possible free spaces at their respective target sites. Also, the vacancy requires an activation energy E_A to leave its place in the lattice, that needs to be weighted against its thermal energy $k_B \theta$, with the temperature θ and the Boltzmann constant k_B. As a quasiparticle holding a charge q_{dop} it is agitated by the external voltage, leading to the hopping rate

$$w_{i \to i \pm 1} = \left(1 - \frac{N_{i \pm 1}}{N_0} \right) \exp\left(\frac{-E_A \pm q_{\mathrm{dop}} \Delta V_i}{k_B \theta} \right). \tag{8.5}$$

The total rate $W_{i\to j}$ of a particle hop from lattice site i to j is proportional to the number of vacancies at the starting place, $W_{i\to j} = N_i w_{i\to j}$. This basic setup is visualized in Fig. (8.1).

From here, the external voltage is changed according to some time protocol. We will investigate the system for a sinusoidal voltage driving

$$V(t) = V_0 \sin(2\pi t/T), \tag{8.6}$$

with amplitude V_0 and period T, the latter setting the scale for all system times. The voltage drop over a lattice site is proportional to its resistance,

$$\Delta V_i = V(t) R_i / R = I(t) R_i. \tag{8.7}$$

Here, the electrical current $I(t)$ is, just as the total resistance R. This system shows similarities to the zero-range process (ZRP) chapter 4.3 with an arbitrary number of vacancies on a single lattice site and transition rates proportional to that number. Unlike simple cases of the ZRP, eqs. (8.5) and (8.7) describe a system with nonlocal transition rates, that do not only depend on the occupation numbers of the adjacent lattice site where the reaction takes places, but on the configuration of the entire lattice. Eq. (8.6) further modulates these rates temporally.

Simulation results for this dynamics are obtained via the Gillespie algorithm [36, 42, 55, 56], which was also used in the simulations of the molecular motors in chapter 5, cf. section 5.3 for a brief description. For the stochastic RS model it provides a feasible performance since it scales with the transition rates, which themselves are exponentially dependent on the external voltage.

For convenience, we introduce reduced units in which all quantities will be given,

$$\hat{V} = V \cdot q_{\mathrm{dop}} / k_B \theta, \qquad \hat{R} = R / R_0 \tag{8.8}$$

$$\hat{I} = I \cdot q_{\mathrm{dop}} R_0 / k_B \theta, \qquad \hat{t} = t/T \tag{8.9}$$

$$\hat{E}_A = E_A / k_B \theta, \qquad \hat{x} = x/L. \tag{8.10}$$

Thereby $R_0 \equiv 1.76\Omega$ follows by a resistivity weighted equidistribution of the vacancies, which is explained in Appendix A.1. Henceforth, all hats are dropped and the voltage is given normalized to its maximum amplitute V_0. Unless stated otherwise, we choose for the simulations parameters $E_A = 1$, $T = 1$, $V_0 = 500$ and $N_0 = 10^4$.

8.3. General Dynamics

The time evolution of a system governed by eqs. (8.2-8.7) is depicted in Fig. 8.2. The electrical current I follows the voltage input, until at a certain threshold value above or below zero the resistance suddenly drops significantly and the current spikes. Hereby, the course of I and R is periodic within each half-cycle of the voltage driving, due to the symmetry of the device.

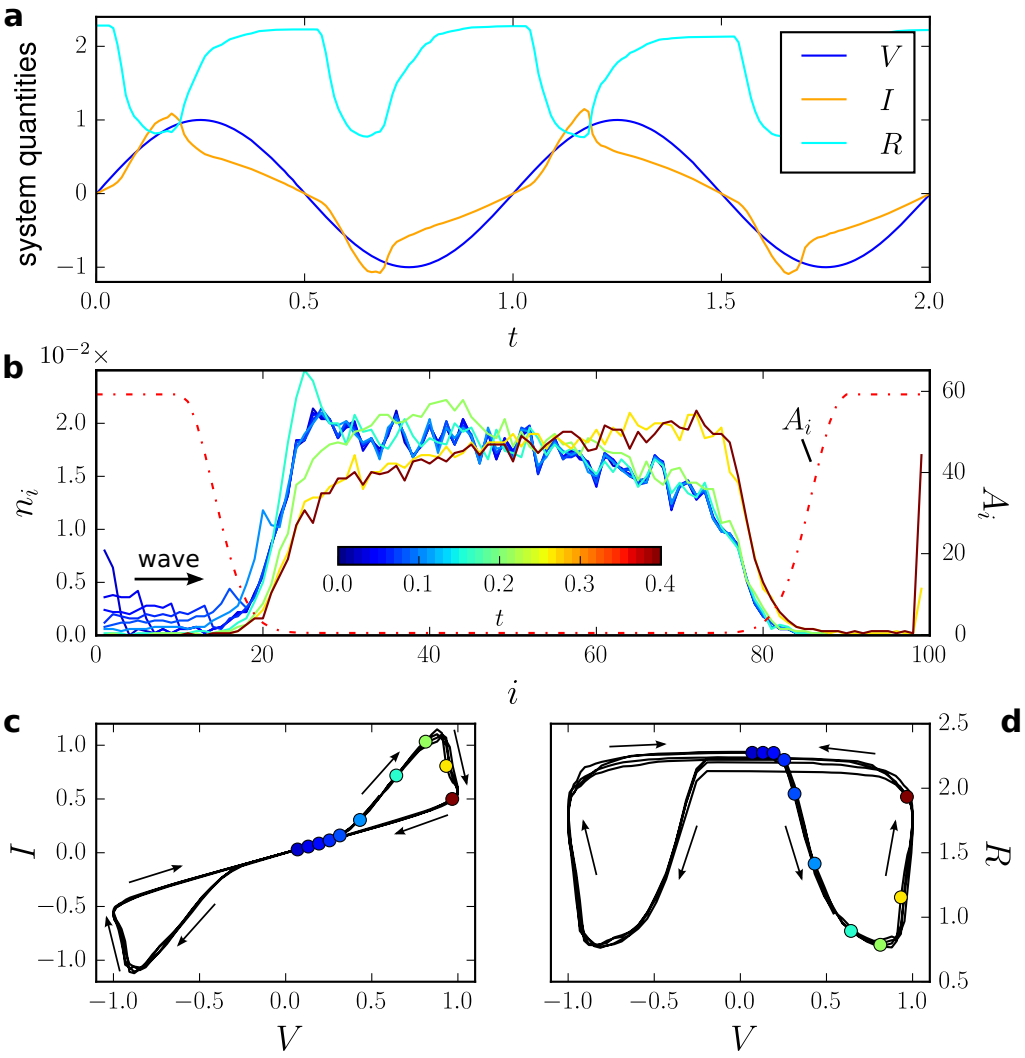

Figure 8.2.: Simulation of stochastic RS-device with sinusoidal voltage driving. Parameters are $\langle N_i \rangle = 10^2$, $N_0 = 10^4$. **a** Time behavior of the electrical quantities **b** Occupation of the individual lattice sites at different times (indicated by the color scale). Local resistivity A_i is indicated by the red dash-doted line **c** Hysteresis in the $I - V$ and **d** $R - V$ planes, the colored circles indicate the states for the various occupation distributions of the middle panel, the arrows show the curves' directionality with increasing time.

Looking at the time dependent vacancy occupation distribution Fig. 8.2.**b** for the positive half-period of the voltage driving, we see that this corresponds to vacancies moving from the left boundary region of A_i to the bulk. The form of this motion reminds us to a dispersing wave, as also noted in [175], until it reaches the bulk. From there some vacancies finally reach the right boundary region. In the final panels the hysteresis loops in the $I-V$ plane and a two-legged structure in the $R-V$ plane are depicted, cf. [150]. It reveals that the wave reaching the bulk corresponds to a drop in the device resistance, and a corresponding spike in the current. As soon as the vacancies reach the right side, the resistance increases again.

As the transport from an accumulation on the sides to the bulk differs in its dynamics from the transport from the bulk to the side, we see the emergence of hysteresis loops in the $I-V$ and $R-V$ diagrams. Also we note that the voltage drop ΔV_i depends on both the external voltage V and the N_i-configuration of the entire lattice, and as a consequence so does $w_{i\to j}$. Hence the distribution of the vacancies plays the role of the inherent memory variable of this resistive switching device, much as the boundary positions w does in the HP-memristor [173]. While a transition of oxygen vacancies between lattice sites with different form factors A_i exerts a global influence on all reaction rates, jumps between lattice sites with the same A_i only affect local rates.

We further want to investigate the system dependence on the sinusoidal driving, particularly on its period T as well as its amplitude V_0. To that end we study two different quantities. Firstly the maximum and minima of the resistance during a switching cycle, $R_{\min}$ and $R_{\max}$, and their ratio $R_{\max}/R_{\min}$. Secondly, the area of the hysteresis loops in the RV-diagram, F_{hyst}.

The results are shown in Fig. 8.3. Therein we see that for very small T the system has no time to react to the sudden changes of the voltage. The minimum and maximum resistances do not differ and the vacancy distribution approaches a state in which, besides fluctuation, every lattice site contributes equally to the resistance, $n_i \propto 1/A_i, R \to 1$. The corresponding hysteresis loops vanish. For longer periods, $R_{\max}$ and $R_{\min}$ start to spread, and the area of the hysteresis loops increases. This is mainly due to the increment in $R_{\max}$ when the vacancies accumulate near the interface; however, when the wave reaches the bulk, $R_{\min}$ reaches values considerably lower than in the equilibrium distribution also.

The picture for the amplitudes is somewhat different. Specifically, for very small V_0, the system has a high resistance. The diffusive motion that is counteracting the external driving is dominant and pushes the vacancies into a uniform distribution. We have $\langle n_i \rangle_t = 10^{-2}, R \to \langle n_i \rangle_t \sum A_i \simeq 17.5$. From a certain threshold above $V_0 \simeq 75$, the resistance suddenly drops and the switching dynamics sets in, with corresponding spreads in $R_{\max}$ and $R_{\min}$ and in the hysteresis loops. Now, the external driving dictates the dynamics. With increasing amplitudes V_0 more vacancies can gather in the high resistance regions near the boundaries, which results in a larger maximal resistance $R_{\max}$. Hence there is a connection between amplitude and period so that

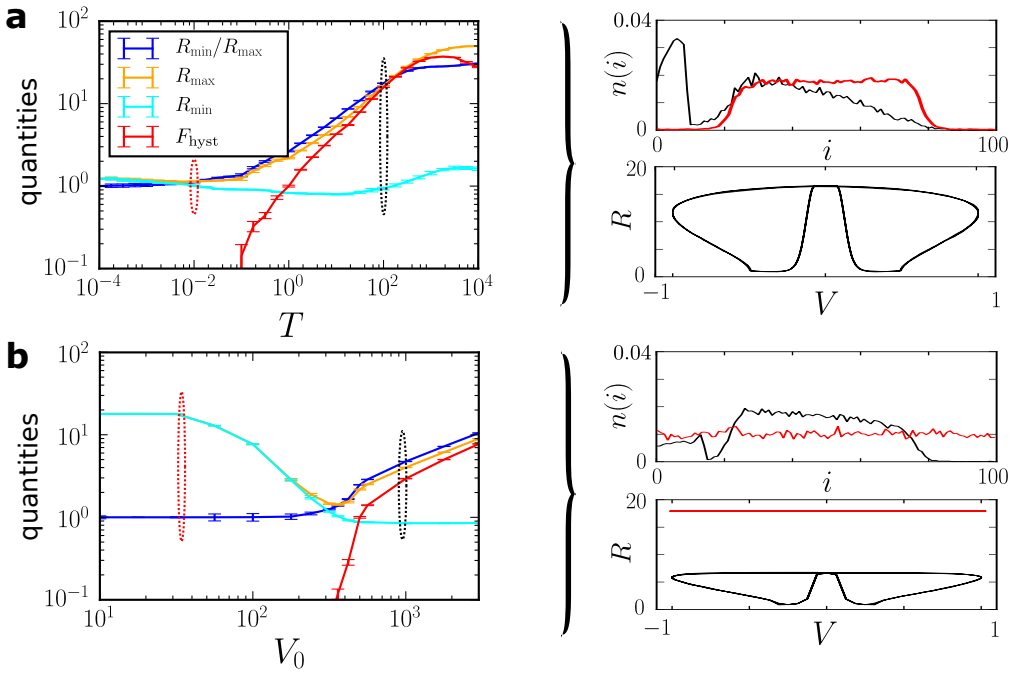

Figure 8.3.: Resistance minima and maxima, their respective ratio and hysteresis loops in the $R-V$ diagram, varied over several cycles of sinusoidal voltage driving. The area of the hysteresis loops F_{hyst} is normalized to that at $V_0 = 500, T = 1$. **a** Variation of the driving period T at $V_0 = 500$. **b** Variation of voltage amplitude V_0 at $T = 1$. Shared legend for **a** and **b** , all parameters as in Fig. 8.2. The right panel shows sample distributions at $t = 0.01$ and resistance over voltage plots for the encircled values of the plot to the left, with curve colors matching the color of the circles.

the system shows meaningful switching behavior.

For the relevant time scale, we remark that the transition rates are proportional to the activation energy, $w_{i\to j} \propto \exp(-E_A)$, cf. eq. (8.5). The larger E_A is, the slower all reactions take place. The other element that sets the time scale of the dynamics, is the external voltage $V(t)$. Since we assume a periodically driven system, the length of the period must increase exponentially to offset the delay due to an increased E_A.

8.3.1. Effects of Fluctuations

The influence of stochasticity is investigated by changing the number of vacancies per lattice sites, while keeping the average vacancy density $n_i = \langle N_i \rangle / N_0$ and the other parameters constant. This means, that for a reduced total number of vacancies $\sum_i N_i$ each individual one bears a larger fraction of the total resistance R and hence

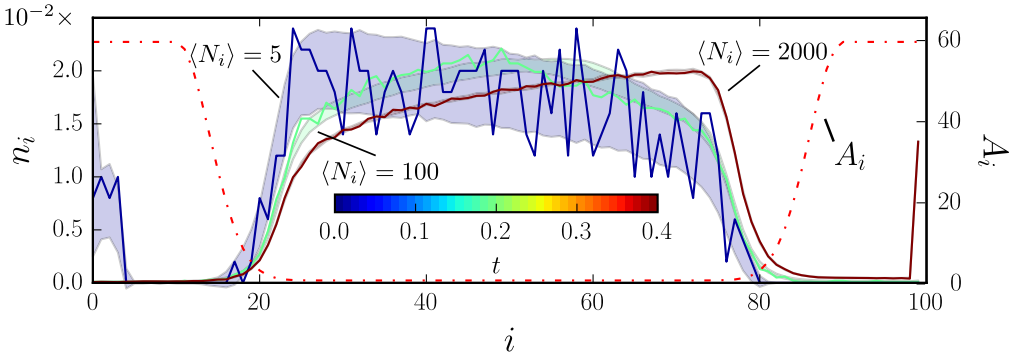

Figure 8.4.: RS dynamics with enhanced fluctuations due to decreased average vacancy number at constant $\langle N_i\rangle / N_0 = 0.01$. Colored faces are the standard deviation around the mean value, inside which one sample distribution for each $\langle N_i\rangle$ is shown. Curves given at different time points of the driving cycle, as indicated by the color scheme.

causes a larger change in the system properties if it hops in between lattice sites with different A_i, while the electrical quantities do not differ in principal, since only the ratio N_i/N_0 enters (cf. eqs. (8.2-8.7)). For large vacancy numbers on the other hand, each individual vacancy barely affects the system and its dynamics will approach the deterministic behavior described by the corresponding master's equation eq. (8.4). In Fig. 8.4 results for various numbers of vacancies per lattice site are depicted at different time points in the switching cycle. Clearly, the fluctuations in the occupation distributions increase for smaller $\langle N_i\rangle$.

The area of the hysteresis curves of the implicit $V - R$ plot are depicted in Fig. 8.5 for varying average particle numbers per lattice site $\langle N_i\rangle$, together with the maxima and minima of the resistance and their respective ratio. We see that for small $\langle N_i\rangle$, the spread in between R_{max} and R_{min} monotonically increases, which also implies an increase in the size of the corresponding hysteresis loops. Also, we see that the variation between individual cycles are larger for small average particle numbers, which can be seen in form of the larger statistical deviations in this case.

These observations are confirmed in the $R - V$ diagram, where we indeed see that both the size of the loops and their fluctuations are bigger for smaller $\langle N_i\rangle$, whereas for many particles fluctuations barely play a role and the results approach the values we gain by direct numerical integration of the corresponding master equation (8.4). Hence we conclude that the resistive switching effect becomes more pronounced with increasing fluctuations. In this sense, the results mirror investigations of the HP-memristor, where it was found that an additional noise increases the memristive response of the system [171].

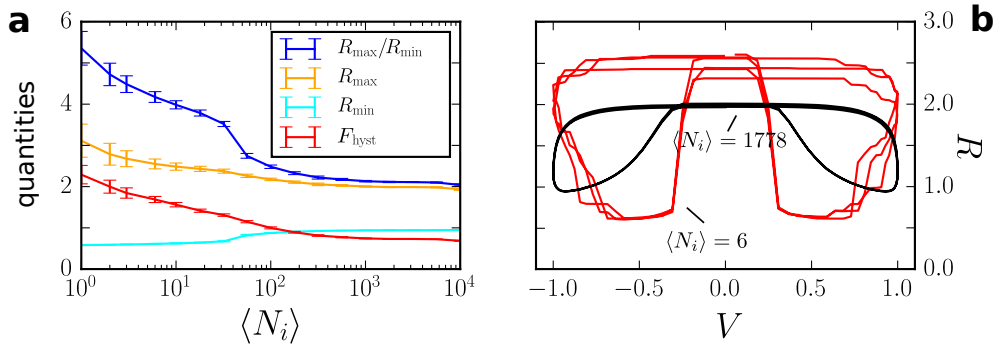

Figure 8.5.: Effects due to enhanced stochasticity caused by different mean number of particles per lattice site $\langle N_i \rangle$. **a** Resistance minima and maxima, and hysteresis loops in the R-V diagram as in Fig. 8.3, albeit as a function of $\langle N_i \rangle$. **b** Sample R-V plots for various $\langle N_i \rangle$. All parameters as in Fig. 8.2.

8.3.2. Continuum Limit and Generalized Burgers' Equation for Wave Transit

In this part, we want to introduce a continuum limit of the master equation in a mean field approximation (MFA). Here, only the outline of the calculations is given. A detailed derivation is shown in the appendix A.2. For the time derivative of the mean occupation density at lattice site i, cf. eq. (8.1), we have

$$\frac{\mathrm{d}}{\mathrm{d}t} \langle n_i(t) \rangle = + \langle n_{i-1} w_{i-1 \to i} \rangle - \langle n_i w_{i \to i+1} \rangle + \langle n_{i+1} w_{i+1 \to i} \rangle - \langle n_i w_{i \to i-1} \rangle \,. \quad (8.11)$$

This expression follows from the master equation (8.4) and is derived in the appendix. The MFA decouples the two point and higher order correlations, resulting in

$$\langle n_i w_{i \to j} \rangle = \langle n_i \rangle \left(1 - \langle n_j \rangle\right) e^{-E_A} \left\langle e^{\Delta V_i} \right\rangle \quad (8.12)$$

Next, we introduce the lattice spacing ϵ between neighboring sites and define $x := i\epsilon$. Formally, the continuum limit is taken by letting the lattice spacing become infinitesimal while the number of lattice sites N runs to infinity, in such a way that the product of both remains the constant lattice length $\lim_{\epsilon \to 0, N \to \infty} \epsilon N = L$. The hopping rates that formerly depended upon the density of neighboring lattice sites now depend on those at an infinitesimal distance ϵ, which will obviously introduce a derivative. The whole approach is quite similar to the derivation of the Burgers' equation for the ASEP model in section 4.3. From here, we will use the rescaled length $\tilde{x} = x/L$ and drop the tilde.

Let the averaged density profile be denoted by $\rho(x)$, from the connection

$$\langle n_i \rangle (t) = \frac{1}{\epsilon} \int_{i\epsilon}^{(i+1)\epsilon} \mathrm{d}x \rho(x,t) \quad (8.13)$$

we obtain $\rho(x,t) = \langle n_i \rangle (t)$. Recall that our previous choice of a lattice with 100 sites corresponds to $\epsilon = 0.01$. The continuous voltage $V(x)$ is introduced analogously to eq. (8.13). Entering this into the MFA hopping rate eq. (8.12) and developing the resulting expression to the second order yields the equation

$$\frac{\partial}{\partial t}\rho(x,t) = e^{-E_A}\cosh\left(\partial_x V\epsilon\right)\epsilon^2\partial_x^2\rho - 2e^{-E_A}\sinh\left(\partial_x V\epsilon\right)\epsilon\partial_x\rho. \tag{8.14}$$

As the electrical current through the system is not position dependent, we express local voltage in the following way (cf. eq. (8.7))

$$\partial_x V(x,t) = \frac{V(t)}{\int \mathrm{d}x' A(x')\rho(x',t)} A(x)\rho(x,t) =: I(t)A(x)\rho(x,t), \tag{8.15}$$

thereby splitting it in a nonlocal and local component. Bearing in mind the continuity equation $\partial_\tau \rho + \mathrm{div} j = 0$, eq. (8.14) is recast into

$$\frac{\partial}{\partial t}\rho(x,t) = \partial_x\Big[e^{-E_A}\cosh\left(IA\epsilon\rho\right)\epsilon^2\partial_x\rho\Big] - \partial_x\Big[2e^{-E_A}\sinh\left(IA\epsilon\rho\right)\epsilon\rho\Big], \tag{8.16}$$

Here, the term in braces is the oxygen vacancy flux. Since ρ can be considered a probability density with the normalization $\int_0^1 \mathrm{d}x\rho(x) = 1$, this constitutes nonlinear continuity equation for the probability. By rescaling the time, the prefactor $\epsilon^2\exp(-E_A)$ can be eliminated. By further, expanding the hyperbolic function to the first order, we are left with

$$\frac{\partial}{\partial t}\rho(x,t) = \partial_x^2\rho(x,t) - 2I(t)\partial_x\left(A(x)\rho^2(x,t)\right). \tag{8.17}$$

This equation can be formally compared to the viscous Burgers' equation. With the viscosity denoted by ν, it reads $\partial_t u = \nu\partial_x^2 u - 1/2\partial_x u^2$. So eq. (8.17) is a generalized Burgers' equation with a current and resistance profile dependent prefactor. Following the wave-like motion of the vacancies, this connection has also been noted in [175].

To validate the derived result, we aim at numerically integrating eq. (8.17) and compare the thereby obtained results with the original numerical results. The integration is done with Neumann boundary conditions, there is no density flux out of the system. The traveling wave solution is shown in Fig. 8.6. Similar to the results seen in Fig. 8.2.**b**, at the beginning of a period there is a surplus of vacancies stored at the left hand side of the RS-device, near $x = 0$, which increases significantly with the driving period T. Upon being agitated by a voltage, these vacancies set in motion in form of a wave with decreasing peak height, until it reaches the bulk. For $T = 1$ the distribution in the bulk is almost flat, the incoming wave forms a hump that moves further to the right with time. Meanwhile, before the second bulk interface around $x = 0.7$ there is initially a hump that flattens and finally disappears as the distribution shifts further to the right. For $T = 10$ on the other hand, the initial distribution in the bulk looks like an inclined plane. The incoming wave rushes

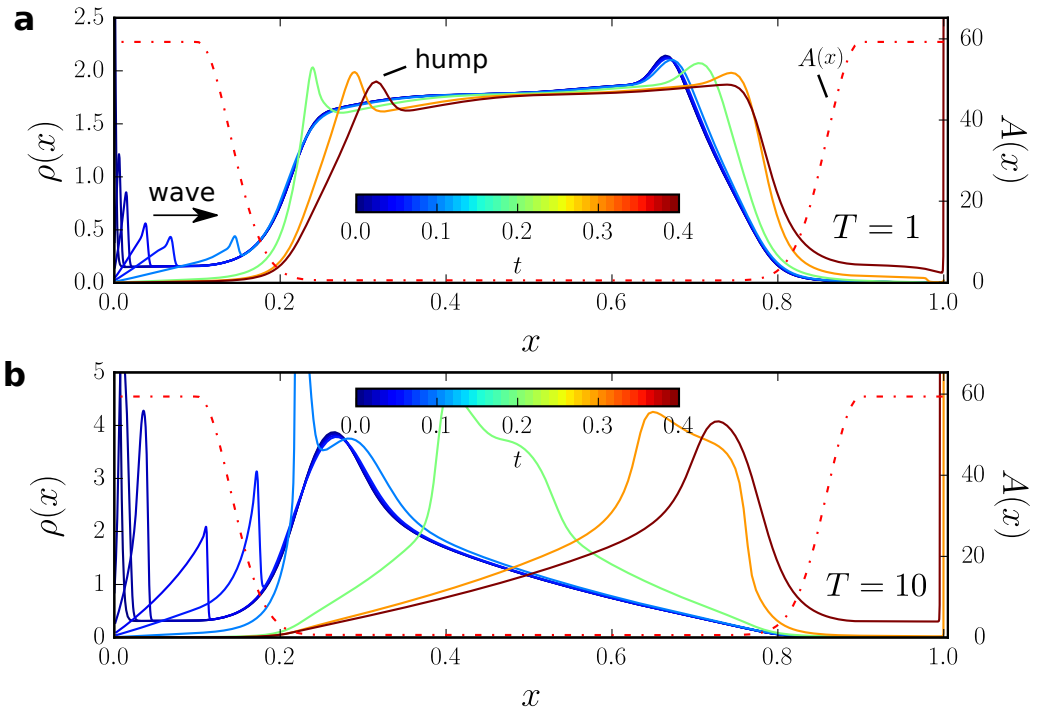

Figure 8.6.: Vacancy distribution of resistive switching modeled by numerical integration of the corresponding Burgers' equation (8.17). Various time points of the switching cycle indicated by the color-coding. Parameters as in Fig. 8.2, for driving periods **a** $T = 1$ and **b** $T = 10$.

through the bulk here, reversing the orientation of the inclined plane on its way through it.

As we can see, the traveling wave reproduces the previous results with good principal agreement, as shown exemplary in the $R - V$ for two different driving periods in Fig. 8.7 superimposed on the corresponding diagrams gained by integration of the particle picture. For all driving periods T, we see some alteration of the two-legged structure.

8.4. Logical States

As we have seen in the previous sections, the resistance of the system depends on how many vacancies are stored within the bulk versus in one of the two boundary regions. Principally, this configuration is similar to two serial switches with counter oriented polarities and one active switching zone each, which we have introduced as the CRS in section 6.2. To that end, we think of the lattice as cut in half and each

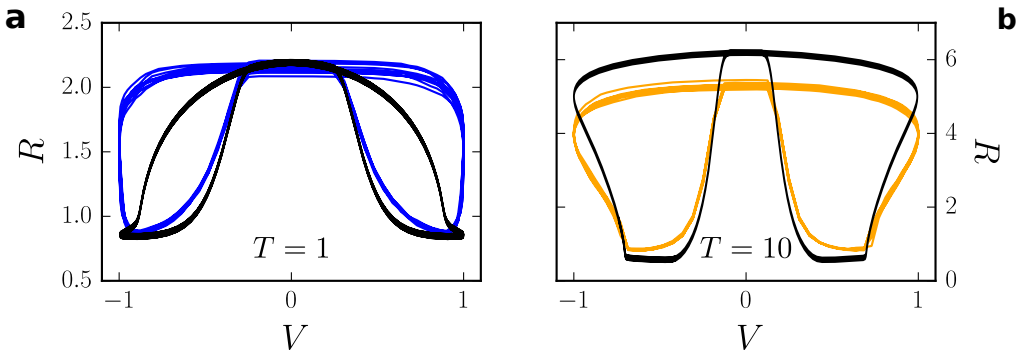

Figure 8.7.: Resistance over voltage of particle simulation (colored, cf. eq. (8.4)) vs numerical integration of Burgers' equation (black, cf. eq. (8.17)) for several cycles of the driving periods **a** $T = 1$ and **b** $T = 10$.

site constituting one resistor that can be either in a high resistive or low resistive state, depending on the distribution of vacancies. This also determines the logical state of the device, as indicated in Fig. 8.8. A gathering of vacancies near one of the electrodes, i.e. in an area with $A_i \gg 0$, leads to a large resistance, whereas in the bulk vacancies only marginally contribute to the resistance, since here $A_i \simeq 0$. Hence, a gathering of vacancies near the first electrode-TMO interface corresponds to a setting $R^{(1)}_{\text{high}} \oplus R^{(2)}_{\text{low}} \widehat{=} 0$, the logical zero, and a gathering near the second interface corresponds to $R^{(1)}_{\text{low}} \oplus R^{(2)}_{\text{high}} \widehat{=} 1$, the logical one. Other configurations, namely an on-on state, $R^{(1)}_{\text{low}} \oplus R^{(2)}_{\text{low}}$, can occur during a read or in the transient of a switching operation, but has no logical equivalent, whereas a vacancy gathering near both electrode interfaces, i.e. $R^{(1)}_{\text{high}} \oplus R^{(2)}_{\text{high}}$ does not occur during the operation of the device [108].

8.4.1. Reading and Writing Operations

Now that we have defined the logical states, we can express the actions of the driving voltage in these terms and develop a framework of how to write and read information in our system.

In Fig. 8.2 we have seen how the positive half-cycle of the external voltage driving acts upon an initial vacancy accumulation near the left interface. Namely, by pushing it to the right interface. During its course, the resistance drops when the vacancy wave hits the bulk, but returns to its initial value once the voltage pulse ends and enough vacancies have accumulated near the right interface. In terms of the logical states, this corresponds to an initial 0-state, onto which the positive voltage pulse acts. Afterwards, the system is in a 1-state. Hence the process is the write 1 operation. It is again displayed in Fig. 8.9.**a**.

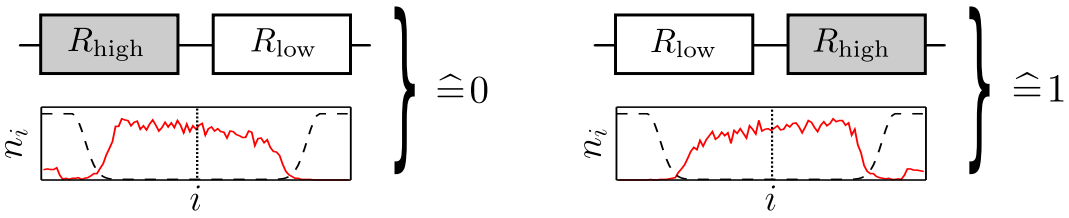

Figure 8.8.: Logical states of the RS device. The top panels illustrates how the lattice can be thought of as two serial resistors, one in a high and one a low resistive state. Their order then determines the logical state. The bottom panels feature a sample vacancy distribution (red color) in the lattice according to the respective states, together with the dashed resistivity profile A_i. A further dotted line cuts the lattice in two halves, each of which corresponds to one of the serial resistors above. An accumulation of vacancies near the left side results in a high resistance of that part, and vice versa with a mirror inverted accumulation near the right side.

In Fig. 8.9.**b** the antagonistic process is shown, where the negative voltage half-cycle acts on a 1-state, resulting in a 0-state. Mirror reversed, the vacancies move from the right interface to the left one. Hence the negative voltage pulse performs the opposing write 0 operation. During its course, the resistance has the same dynamics. We note that the initial states here and for the read operation are prepared by several switching cycles $0 \to 1 \to 0 \to \ldots$.

Let us turn to the reading operation. The state of the system is determined by sending a reading pulse through it and monitoring the reaction. The reading pulse itself is is the positive voltage half-cycle, albeit with half the amplitude of the writing signal $V_{\text{read}} = V_0/2$.

If the reading pulse acts on an initial 0-state, the resistance drops to its minimum level, R_{min}. For the oxygen vacancy distributions we see that the initial vacancy accumulation near the left interface dissolves and moves to the bulk. But unlike for the write case, there is no subsequent buildup of vacancies near the right interface. Hence when the reading pulse has passed, the system remains in the low resistive state $R^{(1)}_{\text{low}} \oplus R^{(2)}_{\text{low}}$. The process is shown in Fig. 8.9.**c**.

On the other hand, if the system is prepared in the 1-state, the reading pulse leads to a slight increase in the resistance above the value R_{max} that is obtained for the switching cycle $1 \to 0 \to 1$. For the distribution, there are virtually no vacancies near the left interface that can be transported to the bulk, while the accumulation near the right electrode already exists and only slightly increases in size. Hence in this case we have only a small effect on the resistance; cf. Fig. 8.9.**d**.

This means that two logical states are distinguished by their differing reactions to the reading pulse. Only when it acts upon the 0-state there is a distinct drop in the resistance. Obviously, the reading pulse has changed the initial distribution, hence a reversely oriented reset pulse need to restore the original configuration in either case.

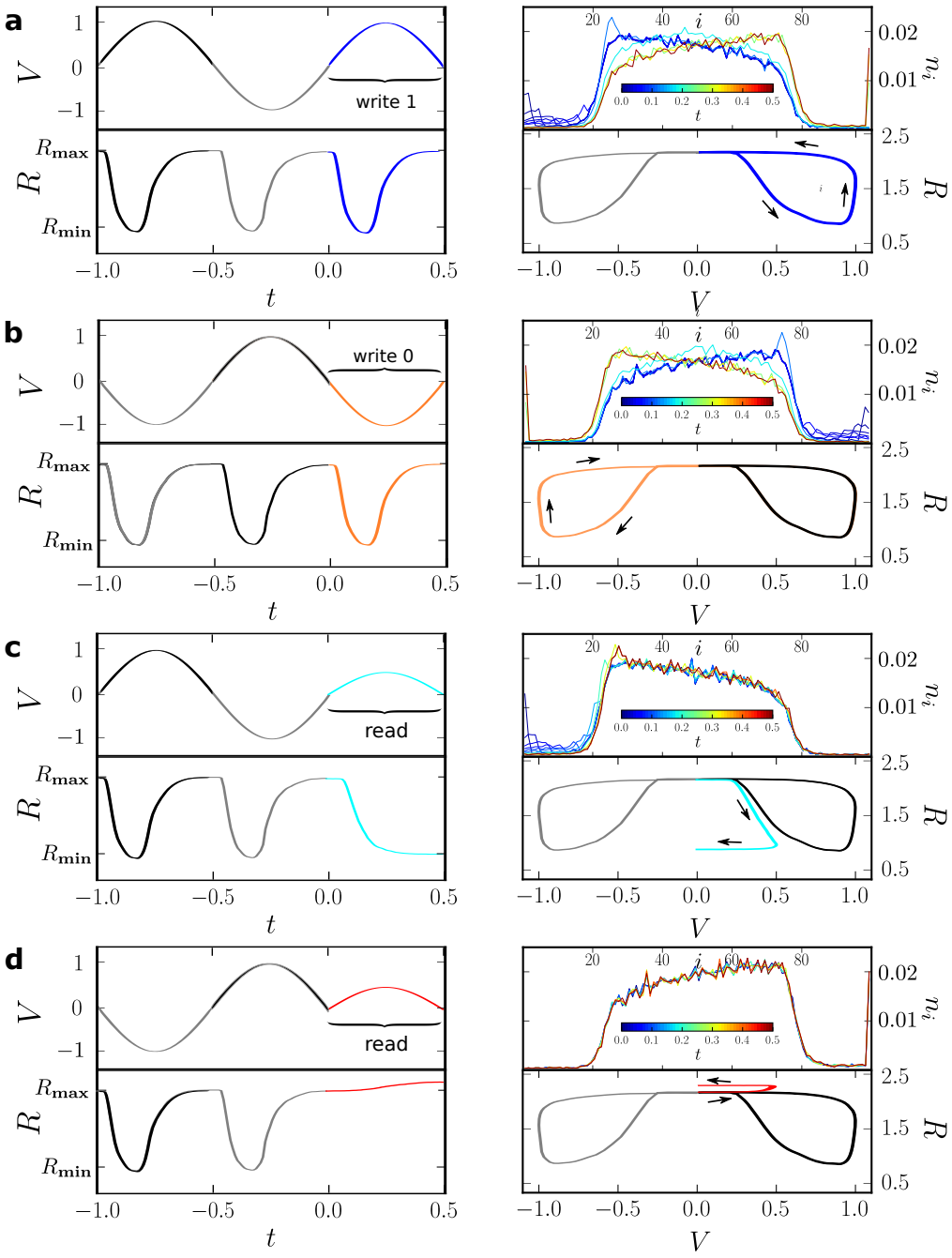

Figure 8.9.: Writing and reading operations in the stochastic RS device. The left panels depict the resistance and voltage over time diagrams, and the right panels depict vacancy distributions at several time points of the specific operation as indicated by the color coding; and the implicit R over V plot. **a** System prepared in state 0 by several writing cycles $0 \to 1 \to 0$, then write 1 operation. **b** System prepared in state 1 by several writing cycles $1 \to 0 \to 1$, then write 0 operation. **c** System prepared in state 0, then reading operation. **d** System prepared in state 1, then reading operation. Writing operations with $V_0 = 500$, reading operation with $V_0 = 250$, all other parameters as in Fig. 8.2.

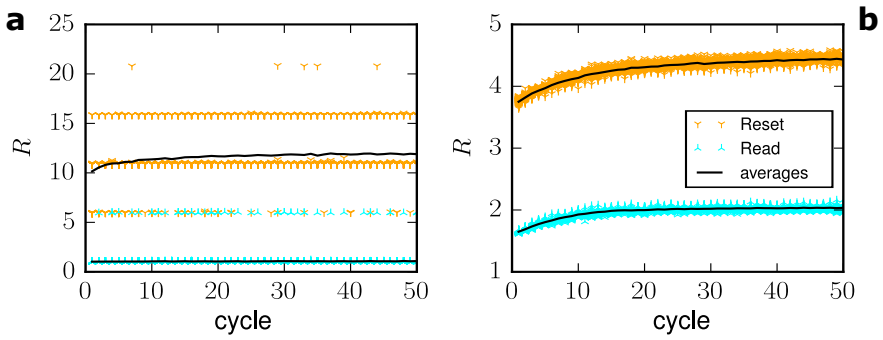

Figure 8.10.: Resistances after several repeats (=cycles) of read and reset operations, for different average particle numbers per lattice site, **a** $\langle N_i \rangle = 0.2$ and **b** $\langle N_i \rangle = 178$. Other parameters as in Fig. 8.2.

8.4.2. Clarity and Stability of the Reading Operation

As noted in section 8.3.1, the resistance drop increases with lower particle numbers and so do the statistical fluctuations associated with it. To be able to correctly determine the state of the device, we must assure that the respective resistances after a read pulse and the corresponding reset pulse do not overlap. This property is demanded for a single read-reset cycle as well as for several.

In Fig. 8.10 various such cycles are shown for two different average particle densities $\langle N_i \rangle$. As we can see, for $\langle N_i \rangle = 0.2$, the possible outcomes for the resistances fall almost perfectly onto discrete levels, one of which is overlapping. Here, we cannot determine in which state the system actually is. For $\langle N_i \rangle = 178$ on the other hand, the ratio of $R_{\text{reset}}/R_{\text{read}}$ is much smaller, but so are the fluctuations accompanying them. Hence both states can be distinguished easily.

In order to quantify the effect, we employ the measure of the discriminability. Originally defined as the difference between the signals with and without noise [39], we adapt it to our current situation by setting

$$d = \frac{|\langle R_{\text{reset}} \rangle - \langle R_{\text{read}} \rangle|}{\sigma} \tag{8.18}$$

with the standard variations of the respective resistances denoted by σ. As such, it is closely related to the signal to noise ratio, which simply is its square: $SNR = d^2$. We approximate that the results fall onto a normal distribution, with peaks at $\langle R_{\text{reset}} \rangle$ and $\langle R_{\text{read}} \rangle$ and the standard deviation σ. This is justified since we are interested only in an estimate of the error.

In Fig. 8.11 this measure is depicted as a function of the average particle number $\langle N_i \rangle$. With increasing $\langle N_i \rangle$, the discriminability of the output improves, since fluctuations largely vanish. Moreover, it drops with the number of read-reset cycles, a spread which is more pronounced for large $\langle N_i \rangle$. In view of Fig. 8.10, this

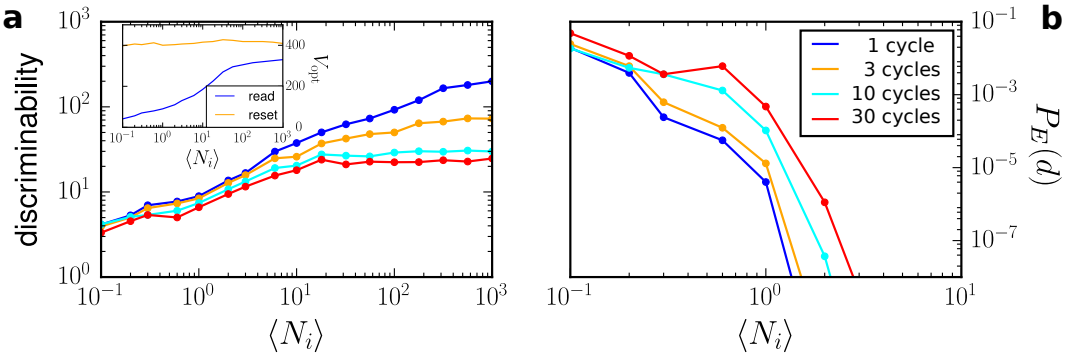

Figure 8.11.: Discriminability and associated probability of a reading error as a function of the average particle number for various numbers of read-reset-cycles. The inset denotes the optimal reading and reset voltages, i.e., those for which the reading resistance drops to a minimum and the reset resistance is close to the value reached in the writing cycle, respectively. Other parameters as in Fig. 8.2.

can be attributed to the transient of the average resistance values. The optimal $V_{\text{read/reset}}$ (shown in the inset of Fig. 8.11) was determined after a writing operation, $1 \rightleftharpoons 0 \rightarrow$ read, and apparently differs slightly from the value that is obtained after a read/reset cycle, read $\rightleftharpoons$ reset $\rightarrow$ read, thereby increasing the interval of the possible outcomes.

To interpret the discriminability measure, we check on how many values will be falsely attributed. The measurements of the read and reset resistances fall onto two normal distributions whose peaks are $\sigma \cdot d$ apart. All measured values $x \leq R_{\text{read}} + \sigma d/2 =: x_{\text{mid}}$ are then assigned to the distribution of R_{read}, all larger values to R_{reset}. Hence the probability of an erroneous attribution is given by those reset values smaller than $\langle R_{\text{read}} \rangle + \sigma d/2$ plus the reading values larger than it. Expressed as a formula

$$\begin{aligned} P_E =& \frac{1}{2} \frac{1}{\sqrt{2\pi\sigma^2}} \int_{x_{\text{mid}}}^{\infty} dx e^{-(x-\langle R_{\text{read}} \rangle)^2/2\sigma^2} + \frac{1}{2} \frac{1}{\sqrt{2\pi\sigma^2}} \int_{-\infty}^{x_{\text{mid}}} dx e^{-(x-\langle R_{\text{reset}} \rangle)^2/2\sigma^2} \\ =& \frac{1}{2} \text{erf}\left(\frac{d}{2\sqrt{2}} \right), \end{aligned} \tag{8.19}$$

where $\text{erf}(x)$ denotes the error function. The corresponding results are plotted in Fig. 8.11. We conclude that for an average vacancy occupation per lattice site of $\langle N_i \rangle \geq 10$ we are secure independently of the number of cycles. Hence, the unambiguity of the reading establishes a lower boundary for the optimal particle number, while the clarity of the resistive switching effect is emphasized with lower particle numbers. This favors a intermediate range of the optimal average particle number of about $N_{\text{optimal}} = \sum_i N_i = 100 \cdot \langle N_i \rangle = 1000$ particles.

We note that the number of vacancies scales with the size of the device. Hence the risk of erroneous read-outs limits the possible degree of miniaturization.

8.5. Conclusion

Resistive switching is a topical and high current interest field in condensed matter physics and a prototype of a nonlinear stochastic switching event. Its main application, the non-volatile resistive random access memory, is a promising candidate for future memory technologies. The scaling to small elements however, leads to an increasing role of fluctuations. It is therefore required, to have an understanding of the switching mechanism and the reliability under the influence of these fluctuations. Here we develop a mesoscopic particle model based on the distribution of oxygen vacancies. Fluctuations caused by the stochasticity of their motion both enhance the resistive contrast and reduce the reliability of the resistive switch. These counteracting tendencies enable us to predict a limit to miniaturization and an optimal system size.

We have introduced a setup to describe a complementary resistive memory switch based on a discrete particle hopping model. Hereby, the spatial distribution of oxygen vacancies plays the vital part in determining the state of the system, which switches between a high and low resistive state. The vacancies' dynamics is given by a master equation with transition rates depending on the vacancy distribution and an external voltage driving.

The application of voltage pulses led to an accumulation of vacancies near the electrode-TMO interface. An antagonistic pulse then sets these accumulations in motion and they collectively wander through the system, thereby affecting the resistance. By formulating the problem in a particle picture, we gained a tool to vary the accompanying fluctuations: less vacancies, more fluctuations. We looked at the characteristics that define an RS element, such as the spread between the high and low resistance, and discovered that they become more pronounced with increasing fluctuations.

The nature of this collective vacancy motion could be elucidated by deriving a nonlinear continuity equation in a MFA from the master equation in continuum space. It has the structure of a Burgers' equation with an additional nonlocal factor, that also incorporates the influence of the driving. We succeeded at numerically integrating this equation to find good agreement with the results gained by particle simulations. Hence we interpreted the motion of the vacancies as a nonlinear traveling wave.

Further, we defined binary logical states in terms of the underlying particle distributions. By linking the actions of voltage pulses to switches between these states, we have established the reading and writing operations necessary to run a memory element. Interestingly, investigations in the stability and discriminability of these operations let us gain a lower limit for the possible number of vacancies in the system, a quantity that is connected with the possible level of miniaturization.

Together with the finding of enhanced RS-characteristics for fewer vacancies, this results in an optimal performance for about 1000 oxygen vacancies.

9. Comparison of the Resistive Switching Models and Outlook

In the previous chapters, a nonlinear deterministic and a stochastic model for RS have been established. In the former, the state of the device is represented by two scalar variables, in the latter by an oxygen vacancy distribution. By also condensing the vacancy distribution into two scalar variables, both descriptions can be linked. The connection variables are chosen to be the normalized centre of mass of the oxygen vacancies of the left and right half of the RS-device, x_1 and x_2. We discuss their behavior with regard to the memristor equations ruling the deterministic system. They apply to x_i fairly well, albeit with a spread in the forward and backward motion. A similar spread appears also in the $q(\phi)$-curves of the stochastic resistive switch. We conclude that the stochastic resistive switch does not constitute a memristive system in the strict sense, as defined in section 6.3. Finally, we will give an outlook how the oxygen vacancy dynamics can be modeled in yet more detail, employing a particle picture with noisy trajectories on a crystal lattice.

9.1. Comparison of the Deterministic and Stochastic RS-Models

We want to discuss the connection between the deterministic CRS model of chapter 7 and the stochastic switching model of chapter 8. In the former, two scalar variables w_1 and w_2 represent the system's memory. They describe the interpolations between a low and high resistivity area, R_{on} and R_{off} respectively, their increment of w_i is proportional to the electric flux through the switch. The resistance of each of the elements constituting the nonlinear HP-type CRS was given by

$$R\Big(w_i(t)\Big) = R_{\text{on}} w_i^p(t) + R_{\text{off}} \left(1 - w_i^p(t)\right), \tag{9.1}$$

with the parameter of nonlinearity p and $w_i \in [0, 1]$. The dynamics of the interpolation variable follows

$$\frac{\mathrm{d}w_{1/2}(t)}{\mathrm{d}t} = \pm \frac{1}{q_0} I(t). \tag{9.2}$$

It is driven by the current flowing through the device, q_0 denotes the charge corresponding to driving the system from $w_1 = 0 \to w_1 = 1$. The total resistance of the

CRS is the sum of its parts, $R_{\mathrm{CRS}}(w_1, w_2) = R(w_1) + R(w_2)$ (compare for equations (7.1), (7.2) and (7.8)).

In case of the stochastic resistive switching, the memory is represented by the distribution of oxygen vacancies, whose configuration $\mathcal{N}$ determines its resistance. The time evolution of the distribution is described by a master equation (8.4), with jumping rates depending on an external voltage signal and the distribution itself, cf. eq. (8.5).

To link this picture to the deterministic model, we connect the memory variables of both systems. As discussed in chapter 8, due to its mirror symmetry the stochastic RS-device with two active zones can be regarded as two devices in anti-serial order as well. Hence, we have one connection variable for each half. The corresponding oxygen distributions are condensed into two scalar variables x_1 and x_2, which are then governing the internal state of the stochastic resistive switch, just as w_1 and w_2 do for the HP-memristor. To this end we propose the centre of mass position of the oxygen vacancies,

$$x_1 = \sum_{i=1}^{L/2} \frac{2i}{L} \frac{N_i}{N_0}, \qquad x_2 = \sum_{i=L/2+1}^{L} \frac{2(L-i)}{L} \frac{N_i}{N_0}, \tag{9.3}$$

and further disallow vacancy hopping from one half to the other, $W_{L/2 \to L/2+1} = W_{L/2+1 \to L/2} = 0$. The split into two halves is possible because the bulk experiences weaker electric fields and is hence less active than the boundary regions. Also vacancy hopping within the bulk does not change the electrical properties of the switch. This separation is valid as long as the driving times are not too large compared to the systems dynamics, after which vacancies will move from one halve to the other in greater numbers (cf. the flat $T = 1$ versus inclined plane $T = 10$ vacancy distributions in Fig. **??**. In the latter case, a considerable amount of oxygen vacancies moves within the bulk).

As the next step, we investigate whether the connection variables x_i can mimic the behavior displayed by the interpolation variables w_i of the deterministic model. To that end, its time course $x(t)$ is compared to $w(t)$, and we check if the increment in $x(t)$ is proportional to the current, as it is the case in the deterministic system, eq. (9.2). Also, we check if the value of x_i can predict the the resistance of the stochastic switch in a way similar to eq. (9.1).

The time dynamics of $x_1(t)$ is depicted in Fig. 9.1.**a** for several driving periods. The connection variable goes forward and backward within a cycle, with the direction as expected dictated by the sign of the external voltage. Also, we notice that the total range within that x_1 changes increases with T, a bigger accumulation of vacancies can build up for longer periods, increasing the range of values that x_1 visits. Following from the inherent symmetry of the device, the course of x_2 is identical to x_1, albeit with a time shift: $x_1(t) = x_2(t + 1/2)$. Also, there is qualitatively a good similarity between the course of these variables and that of x_i we have seen for the nonlinear CMS of chapter 7.

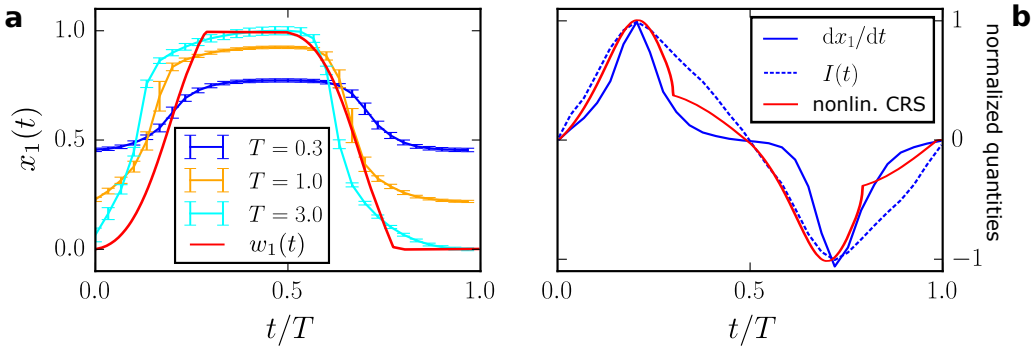

Figure 9.1.: a Time course of the connection variable eq. (9.3) for various periods of the sinussoidal voltage driving, and comparison to the course of $w_1(t)$ for the nonlinear HP-type CRS. All curves normalized so that for $T = 3$, x_1 maps onto the interval $[0, 1]$. **b** Numerical time derivative of $x_1(t)$ and electric current $I(t)$ for $T = 0.3$ of the stochastic CRS, and comparison to $I(t)$ of the nonlinear HP-type CRS. The curves have a similar course, yet for the connection variable, $\mathrm{d}x_1/\mathrm{d}t$ and $I(t)$ differ markedly. Thus eq. (9.2) is only approximately correct for the connection variable. Curves scaled to unit size.

The corresponding time derivative of the connection is shown in Fig. 9.1.**b** alongside the electric current. Both follow each other qualitatively, but the peak in the current is much more narrow, suggesting a complex relation between the two. This contrasts to the mere proportionality in the HP-picture, whose curve runs mostly in between $\mathrm{d}x(t)/\mathrm{d}t$ and $I(t)$. Obviously, eq. (9.2) is not fulfilled faithfully by the connection variable.

Next, we take a look at which resistances correspond to the values of the connection variable; see Fig. 9.2.**a**. It shows a divergence in the $R(x_1)$ dependence for the forward ($V > 0$) and backward motion ($V < 0$). This divergence reflects the fact that the condensed distributions for positive and negative voltages differ fundamentally, which we have seen in the wave motion pictures Fig. 8.2.**b** and Fig. 8.6. An accumulation of vacancies near the interface moves in a wave like motion to the bulk, whereas it is build up more like a constant trickling towards the electrode interface. Moreover, we notice that the range of resistances increases with the period, and so does the range of x_i, which could already be seen in Fig. 9.1.**a**.

In Fig. 9.2.**b** the $R(x)$ plot is shown for the nonlinear HP-CRS (cf. 9.1). We notice, despite the different range of x-values, a similar course for the $R(x)$ in both systems. Especially, the difference in the forward wave and backward trickle motion in the particle picture can be accounted for by different nonlinearity parameters p in the deterministic picture.

Summarizing, we wanted to demonstrate the link in between the deterministic and stochastic RS models, by connecting their respective memory variables. To

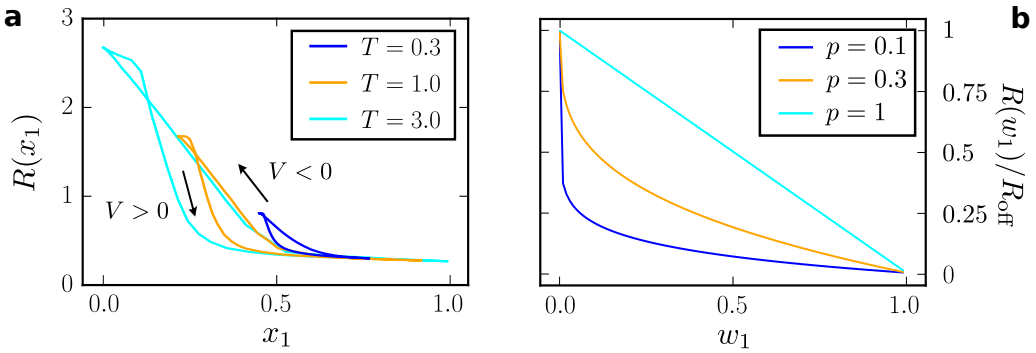

Figure 9.2.: a Dependence of the resistance on the connection variable x_1 of the stochastic RS-device. For several driving periods T; arrows indicate direction of passing with increasing time. A single value of x_1 maps onto different resistances, depending on sign of the driving voltage. **b** Dependence of the resistance of the deterministic CRS for various nonlinearities p, eq. (9.1). In the picture of the nonlinear CRS, the forward and backward $R(x_1)$ functions correspond to different nonlinearities p.

this end we have proposed the normalized centre of mass of the oxygen vacancy distribution as a means to reduce the vacancy distribution into two scalar variables x_i. We proceeded to demonstrate, that these connection variables reproduce the behavior of the boundary variables w_i of the deterministic CRS reasonably well. However, the different particle motions towards and from the bulk lead to a split in the $R(x_i)$ curves, that can be accounted for by introducing different nonlinearities in the deterministic picture.

9.2. Is the Particle Based RS-Device a Memristor?

An ideal memristor is defined by the bijective relation of the charge and the voltage flux, so that the value of either determines the internal state of the device (cf. section 6.3). In this section, we want to investigate $q(\phi)$ characteristics of the stochastic resistive switch.

The corresponding curves are displayed in Fig. 9.3. We see a spread in the forward ($V > 0$) and backward ($V < 0$) curves. Likewise to the spread in the $R(x_i)$ dependence of Fig. 9.2, it can be attributed to different vacancy hopping modes in both directions. While at first glance it may seem that the curves for various parameters can be rescaled so that they are congruent, this is indeed not the case.

As can be seen from comparison of the orange and cyan curves, the same voltage flux leads to different charges, depending on whether it is caused by a longer period or a higher driving voltage. This behavior is referred to as the *voltage-time dilemma* [102, 158]. Actually, the huge nonlinearity of the switching behavior depending on

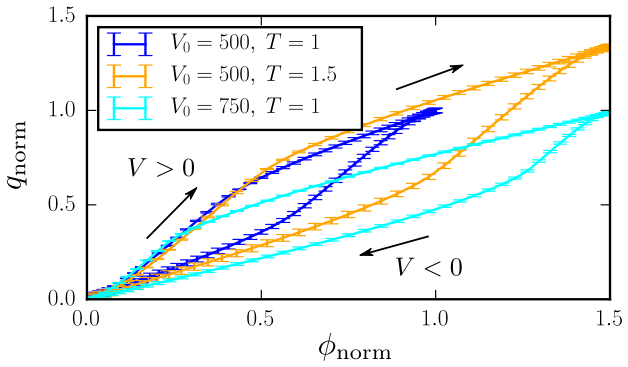

Figure 9.3.: Charge against voltage flux for stochastic RS-device. The $q(\phi)$-curves differ for the forward ($V > 0$) and backward ($V < 0$) motion. The axes cannot be rescaled so that for different parameters the contours overlap. All curves normalized to the maximum flux and charge of the blue curve.

the voltage is desired for RS-devices, as this capability allows for large data retention times versus short switching operations. In case of the stochastic RS it is realized by the exponential dependence of the switching rates on the driving voltage, cf. eq. (8.5), and was also used by us to distinguish between reading and writing operations in section 8.4.

Hence, the stochastic resistive switch does not fulfill the properties of an ideal memristive system as they were introduced in section 6.3. We conclude, that an ideal memristor, if it existed at all, would not make for a very good memory element whereas devices satisfying the demands of memory are not ideal memristors.

9.3. Outlook: A Langevin Model of Resistive Switching

We have introduced a stochastic model based on the random and biased hopping of oxygen vacancies in chapter 8. It is possible to investigate the motion of the oxygen vacancies in yet more detail by considering them as noisy Brownian particles. Such a model has been studied in the references [152–154]. We will outline the Langevin model of resistive switching and propose further investigations based on it.

The system is composed of an ensemble of N interacting vacancies at the positions $\boldsymbol{r_i}(t)$. They are moving on a periodic crystal lattice, whose potential is described by $U(x, y) = U(x + \varepsilon, y) = U(x, y + \varepsilon)$. The pairwise vacancy-vacancy interactions are handled by a potential $W(\boldsymbol{r}_i - \boldsymbol{r}_j)$, and an additional external force $\boldsymbol{F}(\boldsymbol{r}_i, t) = q_{\text{dop}} V(t)/D \cdot \mathbf{e}_y$ is due the applied voltage $V(t)$. Moreover, the noisy environment exerts a random force $\sqrt{2\mathcal{D}_\xi}\boldsymbol{\xi}_i(t)$ on each of the vacancies, which is given by a white Gaussian noise $\boldsymbol{\xi_i}$ with zero mean and independent components in the x- and y-direction, and the noise intensity $\mathcal{D}_\xi$.

In the overdamped limit, the vacancies' stochastic equations of motion can be written

$$\frac{\mathrm{d}\boldsymbol{r}_i(t)}{\mathrm{d}t} = \frac{1}{\gamma}\Big[\boldsymbol{F}_i(\boldsymbol{r}_i,t) - \sum_{j\neq i}\frac{\partial U(\boldsymbol{r}_i)}{\partial \boldsymbol{r}_i} - \sum_{j\neq i}\frac{\partial W(\boldsymbol{r}_i-\boldsymbol{r}_j)}{\partial \boldsymbol{r}_i}\Big] + \sqrt{2\mathcal{D}_\xi}\boldsymbol{\xi}_i(t), \tag{9.4}$$

where γ denotes the friction constant. The interaction potential of the oxygen vacancies in TiO_2 is given by a Lennard-Jones potential modified with an additional Coulomb interaction,

$$W(\mathbf{r}) = \frac{1}{|\mathbf{r}|}\left(12E_{\mathrm{LJ}}\left[\left(\frac{r_{\min}}{|\mathbf{r}|}\right)^{12} - \left(\frac{r_{\min}}{|\mathbf{r}|}\right)^{6}\right] + E_c\frac{r_{\min}}{|\mathbf{r}|}\right). \tag{9.5}$$

Its parameters are chosen so that it fits a microscopically founded interaction potential of the oxygen vacancies in TiO_2 [116, 152], $E_{\mathrm{LJ}} = 2.16\,\mathrm{eV}$, $E_c/E_{\mathrm{LJ}} = 2$ and $R_{\min} = 0.125\,\mathrm{nm}$. The lattice potential is given by

$$U(\mathbf{r}) = U_0 \sin\left(\frac{2\pi x}{\epsilon}\right)\sin\left(\frac{2\pi y}{\epsilon}\right), \tag{9.6}$$

with $U_0 = 4E_{\mathrm{LJ}}/3$ and the lattice spacing $\epsilon = R_{\min}/10$. The external force F_i is due to an external voltage driving that induces an electrical field. It is oriented towards the electrodes.

As a result, the individual vacancies have noisy trajectories, the lattice potential leads to the localization around these potential minima. The parameters are chosen in such a way, that without external voltage, the thermal energy does not suffice to leave the potential minima except for rare events. With additional external driving $V \neq 0$ however, the minima can be left. The electrical field then leads to a preferential motion towards it, while the oxygen-oxygen interactions lead to an additional clustering of vacancies.

So far, no mechanism is introduced to backcouple the positions of the oxygen vacancies to the resistance of the device. Establishing a device resistance based on the positions of the oxygen vacancies is essential to conduct further studies on the Langevin model of RS. If done so, investigations along the following lines will be of interest:

- How does the system react to a sinusoidal voltage driving, can the implicit $R(V)$ and $I(V)$ curves of the previous chapters be reproduced?
- Will a collective motion of vacancies set in, and if so does the accompanying density follow a generalized Burgers' equation as in chapter 8?
- Is there a hysteretic spread in the $q(\phi)$ characteristics?
- Can the geometrical structure of the connecting filament of chapter 7 be reproduced and is it possible to derive values of the nonlinearity parameter p from it?

Part IV.

Conclusions

The goal of this thesis was to show the relevance of mesoscopic stochastic models for the description of transport phenomena in different fields of physics. We demonstrated how the concepts and methods employed, such as ratchets, Langevin and master equations, can be applied to various biological and artificial systems. In **part I** (chapters 2 and 3), we have investigated the persistent motion of active Brownian particles with an additional torque confined to a channel geometry with varying width. In **part II** (chapters 4 and 5) we have developed a model for cargo transport in the axon of nerve cells based on the asymmetric simple exclusion process. In **part III** (chapters 6-9) we have investigated resistive switching, for which a nonlinear deterministic and a stochastic model based on the hopping of oxygen vacancies were elaborated on. The individual parts are connected by the overall goal of achieving directed transport, the influence of noise and by means of the methods used. In this final part, we will summarize the major results of the individual parts, and shed light on the connections in between.

In **part I** we were interested in directed transport of unbiased Brownian particles. They can be either biological or artificial agents, in whose movement a noisy random force plays a vital role. It can be implemented in thermal equilibrium (think for example of pollen or heavy ions), where a fluctuation-dissipation theorem (FDT) connects the noisy drive and the dissipation of their inertia, and outside of equilibrium (think of sperm cells or nanorods), where without FDT the agents can draw energy from an internal energy supply. Ratchet mechanisms can be used to rectify noise outside of thermal equilibrium, by violation of spatio-temporal symmetries. We have briefly introduced two types, the Feynman-Smoluchowski ratchet as its archetypical variant, and the flashing ratchet, in which switching on and off a potential landscape can be used to transport Brownian particles.

In **chapter 3** we have realized a novel kind of ratchet [142], in which correlated noise is rectified and leads to the emergence of directed transport. Brownian particles were equipped with a persistent noisy drive, modeled by the Ornstein-Uhlenbeck process. It was implemented both in thermal equilibrium, where a FDT is satisfied by introducing a memory kernel, and as noisy drive outside of equilibrium. Further, the particles have an additional nonzero mean torque, leading to a circular motion, and are confined to an asymmetric channel geometry with varying width.

In case of the nonequilibrium process, the motion of the Brownian particles gets biased and transport emerges. The mechanism of this symmetry breaking was traced back to the particle hopping along the even boundaries contrasted to a scattering at the uneven ones. Optimal transport is reached for intermediate values of the torque and the persistence length. We interpreted this as a time scale merging between the period due to the torque, which is proportional to $1/\Omega$, and the two relaxation times τ_c and $\tau_{\text{inertia}} = 1/\gamma_0$ that characterize the persistence of the motion.

Due to the general settings of the propulsion, particles, and geometry, this investigation might be the starting point for more precise application oriented modeling of

noisy active particles. Also, it will be interesting to introduce a position dependent mean torque, which can be used the mimic bacterial replies to a chemoattractive gradient [38, 96]. Further studies might involve a moving wall, to which the Brownian agents can transfer inertia in collisions. Such systems have been studied experimentally with bacteria propelling microgears [34, 170].

One of the foremost applications of stochastic transport is the intracellular transport of cargos by molecular motors walking on filaments of the cytoskeleton, which was investigated in **part II**. As a first step, the motors were considered as Brownian particles in a potential landscape induced by the filamentous track. They can move forward due to conformational changes in which they experience the potential landscape differently. Once detailed balance is broken outside of thermal equilibrium by the influx of chemical energy, a bias in their motion appears. This way, a conformation ratchet is realized. By neglecting the internal stepping dynamics, a stepping process with a forward and backward rate results. This simplification allows for new complications: the motion of the motors takes place on a crowded microtubule, where other motors can obstruct the way. This is taken into account by the exclusion processes. We have covered the asymmetric exclusion process (ASEP) and the Langmuir process, for which we derived a Burgers' equation describing the jamming of motors.

In **chapter 5**, we were concerned with the slow transport of cytosolic cargos in the axon of nerve cells. It has only recently been attributed to the action of molecular motors, and features some unusual properties: short phases of rapid motion together with longer rather inactive periods, a transport speed that depends on the density of motors, an increasing number of cargos reversing their transport direction for higher motor densities [29]. Slow axonal transport is generally described by the *stop-and-go hypothesis* [19], a stochastic reaction network that can be fitted well to experimental data, but does not provide an explanation of how the backward motion is realized with a single motor species.

Based on previous work with cargo exchange [57, 148], we have proposed a model with loaded and unloaded motors. In it, cargo transiently connects with a motor to a cargo-motor complex (CMC) that is dissolved if the cargo attaches to a neighboring motor instead. Hence an additional cargo movement takes place on top of the exclusion process for the motors. The behavior of this system was investigated by means of numerical simulations, in which we observed the separation in a high density clustered phase and a low density liquid phase. Additionally, we treated the system in a mean-field approximation that was refined by taking into account the motor clustering, together with phenomenological assumptions about the cluster distribution. The analytical approach was shown to reproduce the numerical results.

Three distinct phases of the cargos' transport modi could be distinguished: First, in a low density phase the hopping of uninterrupted CMCs determines the transport speed, which accordingly is given by their forward stepping rate κ_{cmc}. Second in an

intermediate density phase, the jamming of motors causes the formation of clusters, which coexist with the low density liquid phase. With accumulation on one side and evaporation on the other, the clusters move oppositely to the motors. The cargos can attach to these cluster-quasiparticles and reverse their average direction of motion. Third, in a high density phase the motors are mostly jammed and the bias in the cargo hopping determines the transport.

Concluding, we have covered key attributes of slow axonal transport in a minimal motor hopping model. In particular, we can explain how the bidirectionality of the cargo transport is controlled by the density of forward moving motors alone. It does not require an additional motor species, but is due to the transient attachment to backward moving cluster-quasiparticles.

Further investigations may include a deeper understanding of the influence of different hopping rates and how they affect the jamming dynamics and the clustering mechanism. It will be of particular interest, if the rates can be tuned so that experimental results showing short phases of rapid motion together with longer rather inactive periods can be reproduced by the cargo hopping model as well.

In **part III** we investigated resistive switching (RS), the hysteretic change in the resistance of a dielectric due to the action of an external electric field or an electric flux. Thereby, the resistance depends on the history of the field or flux passing through the system, hence it has a memory. The mayor application of RS is the non-volatile ReRAM, which can be used in highly integrated memory stackbars or as synaptic weights of artificial neural networks [76]. The concept of composite resistive switches (CRS) [108] was featured, which is vital to enhance ReRAM's resilience against read failures and to reduce heat dissipation due to sneak paths. Further, we elaborated on the memristor, the fourth basic passive circuit element, as the theoretical background of RS, and have discussed how it is implemented for the HP-memristor [173].

However, the HP-memristor cannot account for the behavior of the CRS. Hence in **chapter 7** we expanded upon the HP-memristor to gain an analytically solvable CRS model [143]. To that end we proceeded in two steps: First, we have developed a nonlinear alteration of the original HP-memristor. With each switching operation, a filamentous structure that bridges the electrodes is build up or dissolved. Its irregular, conical structure is reflected by the nonlinearity in the resistance interpolation function. Second, we extended this model by the anti-serial combination of two such elements. We are now able to reconstruct the reply curves of the CRS without losing analytical tractability and we can predict the behavior of the CRS with a memristive model, which also reproduces the two-legged structures seen in experimental data for anti-serial bipolar switching [22, 150].

The downscaling of resistive switches to small elements leads to an increasing role of fluctuations. It is therefore required, to have an understanding of the switching mechanism and the reliability under the influence of these fluctuations. In **chapter**

8 we have introduced a mesoscopic model to describe a complementary resistive memory switch based on the hopping of oxygen vacancies on a lattice [141]. Hereby, the spatial distribution of oxygen vacancies plays the vital part in determining the state of the system, which switches between a high and low resistive state. The vacancies' dynamics is given by a master equation with transition rates depending on the vacancy distribution and an external voltage driving. Formally, this is a variant of the zero-range process (cf. section 4.3), albeit with complex non-local and time dependent rates.

The application of voltage pulses led to an accumulation of vacancies at one of the switches' boundaries. An antagonistic pulse then sets these accumulations in motion and they collectively wander through the system, thereby affecting the resistance. The nature of this collective vacancy motion could be elucidated by deriving a nonlinear continuity equation in a MFA in continuum space from the master equation. It has the structure of a Burgers' equation with an additional nonlocal factor, that also incorporates the influence of the driving. We succeeded at numerically integrating this equation to find good agreement with the results gained by particle simulations. Hence we interpreted the motion of the vacancies as a nonlinear traveling wave.

By formulating the problem in a particle picture, we have gained a tool to vary the accompanying fluctuations: less vacancies, more fluctuations. We looked at the characteristics that define an RS element, such as the spread between the high and low resistance, and discovered that they become more pronounced with increasing fluctuations. Further, we defined binary logical states in terms of the underlying particle distributions. By linking the actions of voltage pulses to switches between these states, we have established the reading and writing operations necessary to run a memory element. Strikingly, investigations in the stability and discriminability of these operations let us gain a lower limit for the possible number of vacancies in the system, a quantity that is connected with the possible level of miniaturization. Together with the finding of enhanced RS-characteristics for fewer vacancies, we could predict for the first time an optimal system size: the switches' performance is best for about 1000 oxygen vacancies.

To connect both the deterministic and stochastic RS models, we have condensed the oxygen distribution of the stochastic resistive switch into two scalar variables in **chapter 9**. We discussed their behavior with regard to the memristor equations ruling the deterministic system. These equations apply to the condensed variables fairly well, albeit with a spread in their forward and backward motion, which appears in the $q(\phi)$-function also.Hence, the stochastic resistive switch does not fulfill the properties of an ideal memristive system, for which a bijective $q(\phi)$ relation is required (cf. section 6.3).

Finally, we have proposed further research on a detail-oriented RS model, in which the oxygen vacancy dynamics can be modeled as Brownian particles on a crystal lattice [152–154].

Also, we point out a formal similarity of the stochastic model for RS and the slow axonal transport model of chapter 5: in both, two transport processes take place on top of one another. For slow axonal transport, the cargo transport takes place on top the motor hopping process, and the resulting cargo current hence depends on the motor distribution. The resistive switch is read and written by electron flux, whose strength is determined by the underlying distribution of the vacancies.

A. Appendix

A.1. Simulation Details of the VEOV-Model

We need to specify our assumptions for the form of the resistance profile $A(x)$. While Rozenberg et. al. [150] used a step profile, for simulation it is feasible to smoothen out the regions between the steps. Also, from a physical point of view, a smoother conduit seems reasonable, since both regions are essentially of the same material. For x defined on the interval $[0, 1]$ we set

$$A(x) = \begin{cases} A_\uparrow, \text{ if } x < x_0 \text{ or } x > D - x_0 \\ A_\downarrow + (A_\uparrow - A_\downarrow)\left(\frac{1}{2} + \frac{1}{2}\cos(2\pi\frac{x-x_0}{D-2x_0})\right)^k \text{ otherwise.} \end{cases} \tag{A.1}$$

The higher k is, the more rapid the transition from high to low resistivity. For all simulations, we choose the parameter set $k = 20$, $D = 1$ and $x_0 = 0.1$. Curves for several k are depicted in Fig. A.1. Obviously, the limit $k \to \infty$ yields a step profile for $A(x)$. For the discretized simulation, the number of lattice sites is set to $L = 100$.

If we want to say that we have a device of length D that has a certain total resistance R_{tot}, the resistance profile cannot be independent of the number of lattice sites we choose, but scales with it. If for example we reduce the number of lattice sites, A_i scales accordingly. In fact, we should think of the resistance profile that is introduced in eq. (8.2) as a resistance per length,

$$R_{\text{tot}} = \frac{D}{L}\sum_i \tilde{A}_i \frac{N_i}{N_0}, \qquad A_i = \frac{D}{L}\tilde{A}_i. \tag{A.2}$$

We then choose $A_\downarrow$ and $A_\uparrow$ according to the resistances we want to have, whereas the length D plays no role. For a rough comparability of the results with the HP-memristor, choosing $A_\downarrow = 100$ and $A_\uparrow = 10000$ seems appropriate. Concerning the dynamics, the relative differences in A_i are more important than its absolute value, whose influence can just as well be scaled with other parameters, such as the strength of the driving signal, V_0.

The initial distribution of vacancies is chosen in such a way, that all the lattice site contribute equally to the resistance. This choice minimizes the necessary thermalization time of the system. As the individual sites' resistance is proportional to A_i (cf. eq. (8.2)), the individual vacancies are placed at site i according to the probability

$$P_i = \frac{1}{A_i \sum_i \frac{1}{A_i}}. \tag{A.3}$$

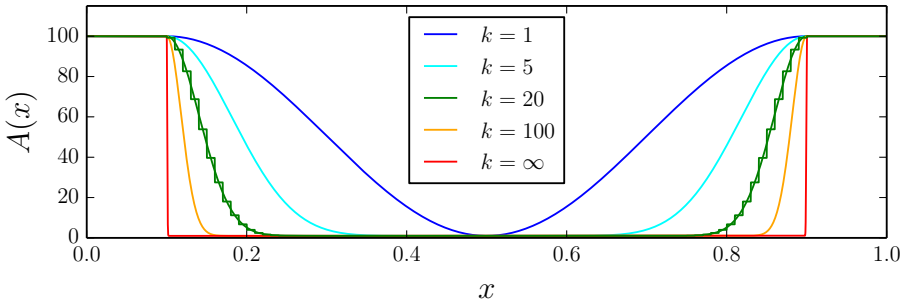

Figure A.1.: Resistance profile $A(x)$ for $A_\downarrow = 1$, $A_\uparrow = 100$ and $x_0 = 0.1$ for various k, compare with eq. (A.1). For $k = 20$, the stepped course of A_i is superimposed for a discretization with 100 lattice sites.

The maximal possible number of vacancies per lattice site N_0 must by no means be identical to the total number of vacancies in the system, although we choose this setting. Hence if we start with on average N_{av} vacancies per site for $L = 100$ sites, then N_0 is set to $N_0 = N_{\mathrm{av}} L$.

A.2. Derivation of the Burgers' Equation

In this appendix, we want to derive the Burgers' equation from the master equations that governs our system. The approach is twofold: at first, we manipulate the discrete master equation to gain the time derivation of the average occupation of a lattice site. With this result, we introduce the continuous limit and expand it to the second order to derive the generalized Burgers' equation. In the master equation

$$\frac{\mathrm{d}}{\mathrm{d}t} P(\mathcal{N}, t) = \sum_{\{\mathcal{N}'\} \neq \mathcal{N}} \Big(- W\left(\mathcal{N} \to \mathcal{N}'\right) P(\mathcal{N}, t) + W\left(\mathcal{N}' \to \mathcal{N}\right) P(\mathcal{N}', t) \Big), \quad \text{(A.4)}$$

a configuration of lattice occupations is denoted by $\mathcal{N} = (N_1, N_2, \cdots, N_L)$ and $\{\mathcal{N}\}$ is the set of all possible configurations. With it, we can express the time dependence of an individual lattice site $\langle \dot{N}_k \rangle$ as

$$\frac{\mathrm{d}}{\mathrm{d}t} \langle N_k \rangle = \frac{\mathrm{d}}{\mathrm{d}t} \sum_{\{\mathcal{N}\}} N_k P(\mathcal{N}, t) \quad \text{(A.5)}$$

$$= \sum_{\{\mathcal{N}\}} N_k \sum_{\{\mathcal{N}'\} \neq \mathcal{N}} \Big(- W\left(\mathcal{N} \to \mathcal{N}'\right) P(\mathcal{N}, t) + W\left(\mathcal{N}' \to \mathcal{N}\right) P(\mathcal{N}', t) \Big). \quad \text{(A.6)}$$

Since only hopping between neighboring sites is allowed, the number of reactions is vastly reduced. By $\mathcal{N}' = (\cdots, N_i', N_{i+1}', \cdots)$ we denote a configuration, that differs

from $\mathcal{N}$ only at the i-th and $i+1$-th position, where it takes the values N_i' and N_{i+1}' respectively. The remaining transitions of the second sum of eq. (A.6) can now be written explicitly, yielding

$$\begin{aligned}\frac{\mathrm{d}}{\mathrm{d}t}\langle N_k\rangle = \sum_{\{\mathcal{N}\}} N_k \Bigg[&- \sum_{i=2}^{L} W\left(\mathcal{N} \to \ldots, N_{i-1}+1, N_i-1, \ldots\right) P(\mathcal{N},t) \\ &- \sum_{i=1}^{L-1} W\left(\mathcal{N} \to \ldots, N_i-1, N_{i+1}+1, \ldots\right) P(\mathcal{N},t) \\ &+ \sum_{i=2}^{L} W\left(\ldots, N_{i-1}+1, N_i-1, \cdots \to \mathcal{N}\right) P(\ldots, N_{i-1}+1, N_i-1, \ldots, t) \\ &+ \sum_{i=1}^{L-1} W\left(\ldots, N_i-1, N_{i+1}+1, \cdots \to \mathcal{N}\right) P(\ldots, N_i-1, N_{i+1}+1, \ldots, t) \Bigg]\end{aligned} \tag{A.7}$$

In this we seek to collect the terms in the angular braces by performing an index shift $N_i \pm 1 = N_i'$, such that the probability function depends on a configuration $\mathcal{N}'$ that is not altered by subtraction or addition of a particle. This substitution can either affect N_k or not. Firstly, the terms of eq. (A.7) which do not:

$$\begin{aligned}&\sum_{\{\mathcal{N}\}} N_k \Bigg[- \sum_{i\neq k,k+1} W\left(\mathcal{N} \to \ldots, N_{i-1}+1, N_i-1, \ldots\right) P(\mathcal{N},t) \\ &\qquad - \sum_{i\neq k-1,k} W\left(\mathcal{N} \to \ldots, N_i-1, N_{i+1}+1, \ldots\right) P(\mathcal{N},t) \Bigg] \\ &+ \sum_{\{\mathcal{N}'\}} N_k' \Bigg[\sum_{i\neq k-1,k} W\left(\mathcal{N}' \to \ldots, N_i'+1, N_{i+1}'-1, \ldots\right) P(\mathcal{N}',t) \\ &\qquad + \sum_{i\neq k,k+1} W\left(\mathcal{N}' \to \ldots, N_{i-1}'-1, N_i'+1, \ldots\right) P(\mathcal{N}',t) \Bigg] = 0\end{aligned} \tag{A.8}$$

Since the summation is done over all possible configurations in both sums, we can rename $\mathcal{N}'$ to $\mathcal{N}$ and see that all summands vanish. The remaining terms involve a

substitution of the prefractor N_k in eq. (A.7),

$$\begin{aligned}\frac{\mathrm{d}}{\mathrm{d}t}\langle N_k\rangle = \sum_{\{\mathcal{N}\}} N_k \Big[&- W\left(\mathcal{N} \to \ldots, N_{i-1}+1, N_i-1, \ldots\right) P(\mathcal{N},t) \\ &- W\left(\mathcal{N} \to \ldots, N_i+1, N_{i+1}1, \ldots\right) P(\mathcal{N},t) \\ &- W\left(\mathcal{N} \to \ldots, N_{i-1}-1, N_i+1, \ldots\right) P(\mathcal{N},t) \\ &- W\left(\mathcal{N} \to \ldots, N_i-1, N_{i+1}+1, \ldots\right) P(\mathcal{N},t)\Big] \\ + \sum_{\{\mathcal{N}'\}} \Big[&(N'_k-1) W\left(\mathcal{N}' \to \ldots, N'_{i-1}+1, N'_i-1, \ldots\right) P(\mathcal{N}',t) \\ &+ (N'_k+1) W\left(\mathcal{N}' \to \ldots, N'_i+1, N'_{i+1}-1, \ldots\right) P(\mathcal{N}',t) \\ &+ (N'_k+1) W\left(\mathcal{N}' \to \ldots, N'_{i-1}-1, N'_i+1, \ldots\right) P(\mathcal{N}',t) \\ &+ (N'_k-1) W\left(\mathcal{N}' \to \ldots, N'_i-1, N'_{i+1}+1, \ldots\right) P(\mathcal{N}',t)\Big]\end{aligned} \tag{A.9}$$

Relabeling the marked quantities to unmarked ones shows that all expressions with the prefactor N_k cancel each other out. This leaves only

$$\begin{aligned}\frac{\mathrm{d}}{\mathrm{d}t}\langle N_k\rangle = \sum_{\{\mathcal{N}\}} \Big[&W\left(\mathcal{N} \to \ldots, N_{i-1}-1, N_i+1, \ldots\right) P(\mathcal{N},t) \\ &- W\left(\mathcal{N} \to \ldots, N_i-1, N_{i+1}+1, \ldots\right) P(\mathcal{N},t) \\ &+ W\left(\mathcal{N} \to \ldots, N_i+1, N_{i+1}-1, \ldots\right) P(\mathcal{N},t) \\ &- W\left(\mathcal{N} \to \ldots, N_{i-1}+1, N_i-1, \ldots\right) P(\mathcal{N},t)\Big]\end{aligned} \tag{A.10}$$

The transition rates W can now be connected to the reaction rates eq. (8.5) by considering the proportionality with the number of particles N_i at an individual lattice site,

$$W\left(\mathcal{N} \to \ldots, N_i-1, N_{i+1}+1, \ldots\right) = N_i w_{i\to i+1} = N_i\left(1-\frac{N_{i+1}}{N_0}\right)e^{-V_0+\Delta V_i}. \tag{A.11}$$

With the further introduction of the density of filled oxygen vacancies $n_i := N_i/N_0$, eq. (A.10) becomes

$$\frac{\mathrm{d}}{\mathrm{d}t}\langle n_k\rangle(t) = +\langle n_{k-1}w_{k-1\to k}\rangle - \langle n_k w_{k\to k+1}\rangle + \langle n_{k+1}w_{k+1\to k}\rangle - \langle n_k w_{k\to k-1}\rangle. \tag{A.12}$$

In this part, we want to introduce a continuous limit of the master equation in a mean field approximation (**MFA**). The MFA now decouples the two point and higher order correlations, resulting in

$$\langle n_i w_{i\to j}\rangle = \langle n_i\rangle \Big(1-\langle n_j\rangle\Big) e^{-V_0}\left\langle e^{\Delta V_i}\right\rangle \tag{A.13}$$

Next, we introduce the lattice spacing ϵ between neighboring sites and define $x := i\epsilon$. The continuum limes is taken by letting the lattice spacing become infinitesimal while the number of lattice sites N runs to infinity, in such a way that the product of both remains the constant lattice length $\lim_{\epsilon\to 0, N\to\infty}\epsilon N = L$. Let the averaged density profile be denoted by $\rho(x,t)$, from the connection

$$\langle n_i\rangle(t) = \frac{1}{\epsilon}\int_{i\epsilon}^{(i+1)\epsilon}\partial_x\rho(x,t) \tag{A.14}$$

we obtain $\rho(x=i\epsilon,t) = \langle n_i\rangle(t)$. The hopping rates that formerly depended upon the density of neighboring lattice sites now depend on those at an infinitesimal distance ϵ, which will obviously introduce an derivation. The continuous formulation of the voltage drop eq. (8.7)

$$\Delta V_i \to \frac{\partial V}{\partial x}\epsilon \tag{A.15}$$

further introduces a sign depending on whether we consider forward ($\epsilon = +|\epsilon|$) or backward ($\epsilon = -|\epsilon|$) fluxes, for it is a directed quantity. Entering this into the MFA hopping rate eq. (A.13) yields[1]

$$\begin{aligned}\frac{\partial}{\partial t}\rho(x,t) =& -\sum_{\sigma=\pm1}\rho(x,t)\Big(1-\rho(x+\sigma\epsilon,t)\Big)e^{-V_0}\exp(+\sigma\partial_x V\epsilon)\\ &+\sum_{\sigma=\pm1}\rho(x+\sigma\epsilon,t)\Big(1-\rho(x,t)\Big)e^{-V_0}\exp(-\sigma\partial_x V\epsilon).\end{aligned} \tag{A.16}$$

The individual terms are expended in a series up to the second order,

$$\rho(x+\sigma\epsilon,t) = \rho(x,t)+\sigma\epsilon\partial_x\rho(x,t)+\frac{1}{2}\epsilon^2\partial_x^2\rho(x,t)+\mathcal{O}(\epsilon^3), \tag{A.17}$$

$$\exp(\pm\sigma\partial_x V\epsilon) = 1\pm\sigma\epsilon\partial_x V\pm\frac{1}{2}\epsilon^2\Big(\partial_x V\Big)^2+\frac{1}{2}\epsilon^2\partial_x^2 V+\mathcal{O}(\epsilon^3), \tag{A.18}$$

and plugged into eq. (A.16). Executing the summation according to the scheme $(a+b)(c+d)+(a-b)(c-d) = 2(ac+bd)$, where a and b (c and d) are the symmetric and antisymmetric terms of the first factors (the exponential, respectively) under a sign change of σ, the following terms remain:

$$\begin{aligned}\frac{\partial}{\partial t}\rho(x,t) =& -2e^{-V_0}\rho\left[\Big(1-\rho-\frac{1}{2}\epsilon^2\partial_x^2\rho\Big)\Big(1+\frac{1}{2}\epsilon^2(\partial_x V)^2+\frac{1}{2}\epsilon^2\partial_x^2 V\Big)-\epsilon(\partial_x\rho)\epsilon(\partial_x V)\right]\\ &+2e^{-V_0}(1-\rho)\left[\Big(\rho+\frac{1}{2}\epsilon^2\partial_x^2\rho\Big)\Big(1-\frac{1}{2}\epsilon^2(\partial_x V)^2+\frac{1}{2}\epsilon^2\Big)\partial_x^2 V+\epsilon(\partial_x\rho)\Big(-\epsilon\partial_x V\Big)\right].\end{aligned} \tag{A.19}$$

[1] for sake of brevity we suppress the time dependence in the argument and write $\rho(x,t) = \rho(x)$

From here, all terms of order $\mathcal{O}(\epsilon^3)$ and higher are dropped,

$$\frac{\partial}{\partial t}\rho(x,t) = e^{-V_0}\Big[-2\rho(1-\rho)\Big(1+\frac{1}{2}\epsilon^2(\partial_x V)^2-\frac{1}{2}\epsilon^2\partial_x^2 V\Big)+\epsilon^2\rho\partial_x^2\rho+2\epsilon^2\rho(\partial_x\rho)(\partial_x V)$$
$$-2(1-\rho)\rho\Big(1-\frac{1}{2}\epsilon^2(\partial_x V)^2+\frac{1}{2}\epsilon^2\partial_x^2 V\Big)-\epsilon^2(1-\rho)\partial_x^2\rho+2\epsilon^2(1-\rho)(\partial_x\rho)(\partial_x V)\Big]. \tag{A.20}$$

As we see, most terms cancel each other out. We are left with

$$\frac{\partial}{\partial t}\rho(x,t) = \epsilon^2 e^{-V_0}\Big[\partial_x^2\rho+2\rho(1-\rho)(\partial_x^2 V)+2(1-2\rho)(\partial_x\rho)(\partial_x V)\Big] \tag{A.21}$$
$$= \epsilon^2 e^{-V_0}\Big[\partial_x^2\rho-2\partial_x\Big(\rho(1-\rho)\partial_x V\Big)\Big]. \tag{A.22}$$

As the electrical current through the system is not position dependent, we express local voltage in the following way (cf. eq. (8.7))

$$\partial_x V(x,t) = \frac{V(t)}{\int \partial_x' A(x')\rho(x')}A(x)\rho(x) =: I(t)A(x)\rho(x), \tag{A.23}$$

thereby splitting it in a nonlocal and local component. Bearing in mind the continuity equation $\partial_\tau\rho+\mathrm{div}j=0$, eq. (A.22) is recast into

$$\frac{\partial}{\partial t}\rho(x,t) = \epsilon^2 e^{-V_0}\partial_x\Big[\partial_x\rho-2IA(x)\rho^2\Big(1-\rho\Big)\Big]. \tag{A.24}$$

Here, the term in braces is oxygen vacancy flux. By rescaling the time, the prefactor $\epsilon^2\exp(-V_0)$ can be eliminated. Since for all practical realizations, the density of vacancies is small against one, the last term is a minor contribution and the remaining equation

$$\frac{\partial}{\partial t}\rho(x,t) = \partial_x^2\rho(x,t)-2I(t)\partial_x\left(A(x)\rho^2(x,t)\right), \tag{A.25}$$

is a generalized Burgers' equation with a current and resistance profile dependent prefactor. The generic viscous (with the viscosity ν) Burgers' equation reads $\partial_t u = \nu\partial_x^2 u - u\partial_x u$.

List of Publications

[1] P. K. Radtke, A. L. Hazel, A. V. Straube, and L. Schimansky-Geier. "Stochastic Dynamics of Resistive Switching: Fluctuations Lead to Optimal Particle Number". In: *New J. Phys.* 19.9 (2017), p. 093007. DOI: 10.1088/1367-2630/aa818b.

[2] P. K. Radtke and L. Schimansky-Geier. "Directed transport of confined Brownian particles with torque". In: *Phys. Rev. E* 85.5 (2012), p. 051110. ISSN: 1539-3755. DOI: 10.1103/PhysRevE.85.051110.

[3] P. K. Radtke and L. Schimansky-Geier. "A nonlinear HP-type complementary resistive switch". In: *AIP Adv.* 6.5 (2016), p. 055119. ISSN: 2158-3226. DOI: 10.1063/1.4952755.

[4] L. W. Rossi, P. K. Radtke, and C. Goldman. "Long-range cargo transport on crowded microtubules: The motor jamming mechanism". In: *Phys. A Stat. Mech. its Appl.* 401 (2014), pp. 319–329. ISSN: 03784371. DOI: 10.1016/j.physa.2014.01.041.

[5] C. Weber, P. K. Radtke, L. Schimansky-Geier, and P. Hänggi. "Active motion assisted by correlated stochastic torques". In: *Phys. Rev. E* 84.1 (2011), p. 011132. ISSN: 1539-3755. DOI: 10.1103/PhysRevE.84.011132.

Parts of the thesis have been published in these articles.

Bibliography

[1] Y. Aghababaie, G. Menon, and M. Plischke. "Universal properties of interacting Brownian motors". In: *Phys. Rev. E* 59.3 (1999), pp. 2578–2586. ISSN: 1063-651X. DOI: 10.1103/PhysRevE.59.2578.

[2] S. Ambrogio, S. Balatti, F. Nardi, S. Facchinetti, and D. Ielmini. "Spike-timing dependent plasticity in a transistor-selected resistive switching memory". In: *Nanotechnology* 24.38 (2013), p. 384012. ISSN: 0957-4484. DOI: 10.1088/0957-4484/24/38/384012.

[3] S. Ambrogio, S. Balatti, D. C. Gilmer, and D. Ielmini. "Analytical Modeling of Oxide-Based Bipolar Resistive Memories and Complementary Resistive Switches". In: *IEEE Trans. Electron Devices* 61.7 (2014), pp. 2378–2386. ISSN: 0018-9383. DOI: 10.1109/TED.2014.2325531.

[4] X. Ao, P. Ghosh, Y. Li, G. Schmid, P. Hänggi, and F. Marchesoni. "Active Brownian motion in a narrow channel". In: *Eur. Phys. J. Spec. Top.* 223.14 (2014), pp. 3227–3242. ISSN: 1951-6355. DOI: 10.1140/epjst/e2014-02329-1.

[5] D. Arcizet, B. Meier, E. Sackmann, J. O. Rädler, and D. Heinrich. "Temporal analysis of active and passive transport in living cells". In: *Phys. Rev. Lett.* 101.24 (2008), p. 248103.

[6] P. F. Arndt and V. Rittenberg. "Spontaneous Breaking of Translational Invariance and Spatial Condensation in Stationary States on a Ring. II. The Charged System and the Two-Component Burgers Equations". In: *J. Stat. Phys.* 107.5/6 (2002), pp. 989–1013. ISSN: 00224715. DOI: 10.1023/A:1015101506637.

[7] A. Asamitsu, Y. Tomioka, H. Kuwahara, and Y. Tokura. "Current switching of resistive states in magnetoresistive manganites". In: *Nature* 388.6637 (1997), pp. 50–52. ISSN: 00280836. DOI: 10.1038/40363.

[8] A. Ascoli, F. Corinto, V. Senger, and R. Tetzlaff. "Memristor model comparison". In: *IEEE Circuits Syst. Mag.* 13.2 (2013), pp. 89–105. ISSN: 1531636X. DOI: 10.1109/MCAS.2013.2256272.

[9] R. D. Astumian and M. Bier. "Fluctuation driven ratchets: Molecular motors". In: *Phys. Rev. Lett.* 72.11 (1994), pp. 1766–1769. ISSN: 00319007. DOI: 10.1103/PhysRevLett.72.1766.

[10] S. Balatti, S. Larentis, D. C. Gilmer, and D. Ielmini. “Multiple memory states in resistive switching devices through controlled size and orientation of the conductive filament”. In: *Adv. Mater.* 25.10 (2013), pp. 1474–1478. ISSN: 09359648. DOI: 10.1002/adma.201204097.

[11] R. Bartussek, P. Reimann, and P. Hänggi. “Precise numerics versus theory for correlation ratchets.” In: *Phys. Rev. Lett.* 76.7 (1996), pp. 1166–1169. ISSN: 1079-7114. DOI: 10.1103/PhysRevLett.76.1166.

[12] S. Bazazi, P. Romanczuk, S. Thomas, L. Schimansky-Geier, J. J. Hale, G. A. Miller, G. A. Sword, S. J. Simpson, and I. D. Couzin. “Nutritional state and collective motion: from individuals to mass migration”. In: *Proc. R. Soc. London B* 278.1704 (2011), p. 356. ISSN: 0962-8452.

[13] A. Beck, J. G. Bednorz, C. Gerber, C. Rossel, and D. Widmer. “Reproducible switching effect in thin oxide films for memory applications”. In: *Appl. Phys. Lett.* 77.1 (2000), p. 139. ISSN: 00036951. DOI: 10.1063/1.126902.

[14] S. Benderli and T. Wey. “On SPICE macromodelling of TiO_2 memristors”. In: *Electron. Lett.* 45.7 (2009), p. 377. ISSN: 00135194. DOI: 10.1049/el.2009.3511.

[15] Z. Biolek, D. Biolek, and V. Biolková. “SPICE model of memristor with nonlinear dopant drift”. In: *Radioengineering* 18.2 (2009), pp. 210–214. ISSN: 12102512.

[16] R. A. Blythe and M. R. Evans. “Nonequilibrium steady states of matrix-product form: a solver’s guide”. In: *J. Phys. A Math. Theor.* 40.46 (2007), R333–R441. ISSN: 1751-8113. DOI: 10.1088/1751-8113/40/46/R01.

[17] P. Bressloff and J. Newby. “Stochastic models of intracellular transport”. In: *Rev. Mod. Phys.* 85.1 (2013), pp. 135–196. ISSN: 0034-6861. DOI: 10.1103/RevModPhys.85.135.

[18] A. Brown. “Axonal transport of membranous and nonmembranous cargoes: a unified perspective.” In: *J. Cell Biol.* 160.6 (2003), pp. 817–21. ISSN: 0021-9525. DOI: 10.1083/jcb.200212017.

[19] A. Brown. “Stochastic Simulation of Neurofilament Transport in Axons: The "Stop-and-Go" Hypothesis”. In: *Mol. Biol. Cell* 16.9 (2005), pp. 4243–4255. ISSN: 1059-1524. DOI: 10.1091/mbc.E05-02-0141.

[20] R. K. Budhathoki, M. P. Sah, S. P. Adhikari, H. Kim, and L. Chua. “Composite behavior of multiple memristor circuits”. In: *IEEE Trans. Circuits Syst. I Regul. Pap.* 60.10 (2013), pp. 2688–2700. ISSN: 15498328. DOI: 10.1109/TCSI.2013.2244320.

[21] H. B. Callen and T. A. Welton. “Irreversibility and Generalized Noise”. In: *Phys. Rev.* 83.1 (1951), pp. 34–40. DOI: 10.1103/PhysRev.83.34.

[22] X. Chen, N. J. Wu, J. Strozier, and A. Ignatiev. "Direct resistance profile for an electrical pulse induced resistance change device". In: *Appl. Phys. Lett.* 87.23 (2005), p. 233506. ISSN: 00036951. DOI: 10.1063/1.2139843.

[23] O. Chepizhko and F. Peruani. "Active particles in heterogeneous media display new physics". In: *Eur. Phys. J. Spec. Top.* 224.7 (2015), pp. 1287–1302. ISSN: 1951-6355. DOI: 10.1140/epjst/e2015-02460-5.

[24] O. Chepizhko and F. Peruani. "Diffusion, subdiffusion, and trapping of active particles in heterogeneous media". In: *Phys. Rev. Lett.* 111.16 (2013), pp. 1–5. ISSN: 00319007. DOI: 10.1103/PhysRevLett.111.160604.

[25] L. Chua. "Memristor-the missing circuit element". In: *Circuit Theory, IEEE Trans.* 18.5 (1971), pp. 507–519.

[26] L. Chua. "Resistance switching memories are memristors". In: *Appl. Phys. A* 102.4 (2011), pp. 765–783. ISSN: 0947-8396. DOI: 10.1007/s00339-011-6264-9.

[27] L. O. Chua and S. M. Kang. "Memristive devices and systems". In: *Proc. IEEE* 64.2 (1976), pp. 209–223.

[28] L. Conway and J. L. Ross. "A model system to study transport of self-assembled cargos." In: *Commun. Integr. Biol.* 6.5 (2013), p. 3. ISSN: 1942-0889. DOI: 10.4161/cib.25387.

[29] L. Conway, D. Wood, E. Tüzel, and J. L. Ross. "Motor transport of self-assembled cargos in crowded environments." In: *Proc. Natl. Acad. Sci. U. S. A.* 109.51 (2012), pp. 20814–9. ISSN: 1091-6490. DOI: 10.1073/pnas.1209304109.

[30] F. Corinto and A. Ascoli. "A boundary condition-based approach to the modeling of memristor nanostructures". In: *IEEE Trans. Circuits Syst. I Regul. Pap.* 59.11 (2012), pp. 2713–2726. ISSN: 15498328. DOI: 10.1109/TCSI.2012.2190563.

[31] D. Cubero and F. Renzoni. *Brownian Ratchets*. Cambridge: Cambridge University Press, 2016. ISBN: 9781107478206. DOI: 10.1017/CBO9781107478206.

[32] B. Derrida. "An exactly soluble non-equilibrium system: The asymmetric simple exclusion process". In: *Phys. Rep.* 301 (1998), pp. 65–83. ISSN: 03701573. DOI: 10.1016/S0370-1573(98)00006-4.

[33] P. Dhar, T. M. Fischer, Y. Wang, T. E. Mallouk, W. F. Paxton, and A. Sen. "Autonomously moving nanorods at a viscous interface". In: *Nano Lett.* 6.1 (2006), pp. 66–72. ISSN: 15306984. DOI: 10.1021/nl052027s.

[34] R. Di Leonardo, L. Angelani, D. DellÕArciprete, G. Ruocco, V. Iebba, S. Schippa, M. Conte, F. Mecarini, F. De Angelis, and E. Di Fabrizio. "Bacterial ratchet motors". In: *Proc. Natl. Acad. Sci. U. S. A.* 107.21 (2010), pp. 9541–9545. DOI: 10.1073/pnas.0910426107.

[35] M. Di Ventra, Y. V. Pershin, and L. O. Chua. “Circuit elements with memory: Memristors, memcapacitors, and meminductors”. In: *Proc. IEEE* 97.10 (2009), pp. 1717–1724. ISSN: 00189219. DOI: 10.1109/JPROC.2009.2021077.

[36] W. Ebeling and L. Schimansky-Geier. “Stochastic dynamics of a bistable reaction system”. In: *Phys. A Stat. Mech. its Appl.* 98.3 (1979), pp. 587–600. ISSN: 03784371. DOI: 10.1016/0378-4371(79)90157-2.

[37] A. Einstein. “Über die von der molekularkinetischen Theorie der Wärme geforderte Bewegung von in ruhenden Flüssigkeiten suspendierten Teilchen”. In: *Ann. Phys.* 322.8 (1905), pp. 549–560. ISSN: 00033804. DOI: 10.1002/andp.19053220806.

[38] M. Eisenbach, J. W. Lengeler, M. Varon, D. Gutnick, R. Meili, R. Firtel, J. Segall, G. Omann, A. Tamada, and F. Murakami. *Chemotaxis*. Vol. 1. Imperial College Press London, 2004.

[39] T. A. Engel, B. Helbig, D. F. Russell, L. Schimansky-Geier, and A. B. Neiman. “Coherent stochastic oscillations enhance signal detection in spiking neurons”. In: *Phys. Rev. E* 80.2 (2009), p. 021919. ISSN: 1539-3755. DOI: 10.1103/PhysRevE.80.021919.

[40] P. Eshuis, K. van der Weele, D. Lohse, and D. van der Meer. “Experimental Realization of a Rotational Ratchet in a Granular Gas”. In: *Phys. Rev. Lett.* 104.24 (2010), p. 248001. ISSN: 0031-9007. DOI: 10.1103/PhysRevLett.104.248001.

[41] M. R. Evans, R. Juhász, and L. Santen. “Shock formation in an exclusion process with creation and annihilation”. In: *Phys. Rev. E* 68.2 (2003), p. 026117. ISSN: 1063-651X. DOI: 10.1103/PhysRevE.68.026117.

[42] R. Feistel and W. Ebeling. “Deterministic and stochastic theory of sustained oscillations in autocatalytic reaction systems”. In: *Phys. A Stat. Mech. its Appl.* 93.1-2 (1978), pp. 114–137. ISSN: 03784371. DOI: 10.1016/0378-4371(78)90213-3.

[43] P. A. Ferrari. “Shocks in the Burgers Equation and the Asymmetric Simple Exclusion Process”. In: *Stat. Physics, Autom. Networks Dyn. Syst.* Dordrecht: Springer Netherlands, 1992, pp. 25–64. DOI: 10.1007/978-94-011-2578-9_2.

[44] R. P. Feynman, R. B. Leighton, and M. Sands. *The Feynman Lectures on Physics, Vol. 1, Chapter 46*. Addison Wesley, Reading MA, 1963.

[45] S. Flach, O. Yevtushenko, and Y. Zolotaryuk. “Directed current due to broken time-space symmetry”. In: *Phys. Rev. Lett.* 84.11 (2000), pp. 2358–2361.

[46] B. M. Friedrich and F. Jülicher. “The stochastic dance of circling sperm cells: sperm chemotaxis in the plane”. In: *New J. Phys.* 10 (2008), p. 123025.

[47] B. M. Friedrich, I. H. Riedel-Kruse, J. Howard, and F. Jülicher. "High-precision tracking of sperm swimming fine structure provides strong test of resistive force theory". In: *J. Exp. Biol.* 213.8 (2010), pp. 1226–1234. ISSN: 0022-0949. DOI: 10.1242/jeb.039800.

[48] T. Fujii, M. Kawasaki, A. Sawa, H. Akoh, Y. Kawazoe, and Y. Tokura. "Hysteretic current-voltage characteristics and resistance switching at an epitaxial oxide Schottky junction $SrRuO_3SrTi_0.99Nb_{0.01}O_3$". In: *Appl. Phys. Lett.* 86.1 (2005), p. 012107. ISSN: 0003-6951. DOI: 10.1063/1.1845598.

[49] K. Fujiwara, T. Nemoto, M. J. Rozenberg, Y. Nakamura, and H. Takagi. "Resistance Switching and Formation of a Conductive Bridge in Metal/Binary Oxide/Metal Structure for Memory Devices". In: *Jpn. J. Appl. Phys.* 47.8 (2008), pp. 6266–6271. ISSN: 0021-4922. DOI: 10.1143/JJAP.47.6266.

[50] M. L. Gardel, I. C. Schneider, Y. Aratyn-Schaus, and C. M. Waterman. "Mechanical Integration of Actin and Adhesion Dynamics in Cell Migration". In: *Annu. Rev. Cell Dev. Biol.* 26.1 (2010), pp. 315–333. ISSN: 1081-0706. DOI: 10.1146/annurev.cellbio.011209.122036.

[51] C. W. Gardiner. *Handbook of Stochastic Methods for Physics, Chemistry and the Natural Sciences*. Vol. 13. Springer Series in Synergetics 10. Berlin, Heidelberg: Springer Berlin Heidelberg, 1985. ISBN: 978-3-540-61634-4.

[52] P. S. Georgiou, S. N. Yaliraki, E. M. Drakakis, and M. Barahona. "Quantitative measure of hysteresis for memristors through explicit dynamics". In: *Proc. R. Soc. A Math. Phys. Eng. Sci.* 468.2144 (2012), pp. 2210–2229. ISSN: 1364-5021. DOI: 10.1098/rspa.2011.0585.

[53] N. Ghenzi, M. J. Sánchez, and P. Levy. "A compact model for binary oxides-based memristive interfaces". In: *J. Phys. D. Appl. Phys.* 46.41 (2013), p. 415101. ISSN: 0022-3727. DOI: 10.1088/0022-3727/46/41/415101.

[54] P. Ghosh, P. Hänggi, F. Marchesoni, S. Martens, F. Nori, L. Schimansky-Geier, and G. Schmid. "Driven Brownian transport through arrays of symmetric obstacles". In: *Phys. Rev. E* 85.1 (2012), p. 011101. DOI: 10.1103/PhysRevE.85.011101.

[55] D. T. Gillespie. "A general method for numerically simulating the stochastic time evolution of coupled chemical reactions". In: *J. Comput. Phys.* 22.4 (1976), pp. 403–434. ISSN: 10902716. DOI: 10.1016/0021-9991(76)90041-3.

[56] D. T. Gillespie. "Exact Stochastic Simulation of couple chemical reactions". In: *J. Phys. Chem.* 81.1 (1977), pp. 2340–2361. ISSN: 0022-3654. DOI: 10.1021/j100540a008.

[57] C. Goldman. "A Hopping Mechanism for Cargo Transport by Molecular Motors on Crowded Microtubules". In: *J. Stat. Phys.* 140 (2010), pp. 1167–1181. ISSN: 00224715. DOI: 10.1007/s10955-010-0037-2.

[58] C. Goldman and E. T. Sena. "The dynamics of cargo driven by molecular motors in the context of asymmetric simple exclusion processes". In: *Phys. A Stat. Mech. its Appl.* 388.17 (2009), pp. 3455–3464. ISSN: 03784371. DOI: 10.1016/j.physa.2009.04.038.

[59] I. Goychuk and P. Hänggi. "Minimal quantum Brownian rectifiers". In: *J. Phys. Chem. B* 105.28 (2001), pp. 6642–6647.

[60] L. Greenemeier and J. Kelly. *Will IBM's Watson Usher in a New Era of Cognitive Computing?* 2013.

[61] L. Haeggqwist, L. Schimansky-Geier, I. M. Sokolov, and F. Moss. "Hopping on a zig-zag course". In: *Eur. Phys. J. Spec. Top.* 157.1 (2008), pp. 33–42. ISSN: 1951-6355. DOI: 10.1140/epjst/e2008-00628-8.

[62] B. ten Hagen, F. Kümmel, R. Wittkowski, D. Takagi, H. Löwen, and C. Bechinger. "Gravitaxis of asymmetric self-propelled colloidal particles." In: *Nat. Commun.* 5 (2014), p. 4829. ISSN: 2041-1723. DOI: 10.1038/ncomms5829.

[63] P. Hänggi. "Correlation functions and masterequations of generalized (non-Markovian) Langevin equations". In: *Zeitschrift für Phys. B Condens. Matter* 31.4 (1978), pp. 407–416. ISSN: 0340-224X. DOI: 10.1007/BF01351552.

[64] P. Hänggi and P. Jung. "Colored noise in dynamical systems". In: *Adv. Chem. Phys.* 89 (1995), pp. 239–326.

[65] P. Hänggi, F. Marchesoni, and P. Grigolini. "Bistable flow driven by coloured gaussian noise: A critical study". In: *Zeitschrift für Phys. B Condens. Matter* 56.4 (1984), pp. 333–339. ISSN: 0722-3277. DOI: 10.1007/BF01306642.

[66] Harvard BioVisions group and XVIVO. *The inner life of the Cell.* URL: https://www.youtube.com/watch?v=FzcTgrxMzZk%7B%5C&%7Dt=5s.

[67] D. Hexner and Y. Kafri. "Tug of war in motility assay experiments." In: *Phys. Biol.* 6.3 (2009), p. 036016. ISSN: 1478-3975. DOI: 10.1088/1478-3975/6/3/036016.

[68] W. Horsthemke and R. Lefever. *Noise-Induced Transitions.* Vol. 15. Springer Series in Synergetics. Springer Berlin Heidelberg, 2006, pp. 108–163. ISBN: 978-3-540-11359-1. DOI: 10.1007/3-540-36852-3.

[69] L. H'walisz, P. Jung, P. Hänggi, P. Talkner, and L. Schimansky-Geier. "Colored noise driven systems with inertia". In: *Zeitschrift für Phys. B Condens. Matter* 77.3 (1989), pp. 471–483. ISSN: 0722-3277. DOI: 10.1007/BF01453798.

[70] A. Ignatiev, N. J. Wu, X. Chen, S. Q. Liu, C. Papagianni, and J. Strozier. "Resistance switching in perovskite thin films". In: *Phys. status solidi* 243.9 (2006), pp. 2089–2097. ISSN: 0370-1972. DOI: 10.1002/pssb.200666805.

[71] G. Indiveri, B. Linares-Barranco, R. Legenstein, G. Deligeorgis, and T. Prodromakis. "Integration of nanoscale memristor synapses in neuromorphic computing architectures." In: *Nanotechnology* 24.38 (2013), p. 384010. ISSN: 1361-6528. DOI: 10.1088/0957-4484/24/38/384010.

[72] D. S. Jeong, R. Thomas, R. S. Katiyar, J. F. Scott, H. Kohlstedt, A. Petraru, and C. S. Hwang. "Emerging memories: resistive switching mechanisms and current status". In: *Reports Prog. Phys.* 75.7 (2012), p. 076502. ISSN: 0034-4885. DOI: 10.1088/0034-4885/75/7/076502.

[73] H. R. Jiang, N. Yoshinaga, and M. Sano. "Active motion of a Janus particle by self-thermophoresis in a defocused laser beam". In: *Phys. Rev. Lett.* 105.26 (2010), pp. 1–4. ISSN: 00319007. DOI: 10.1103/PhysRevLett.105.268302.

[74] J. I. Jiménez-Aquino and M. Romero-Bastida. "Fokker-Planck-Kramers equation for a Brownian gas in a magnetic field". In: *Phys. Rev. E* 74.4 (2006), p. 041117. ISSN: 1539-3755. DOI: 10.1103/PhysRevE.74.041117.

[75] J. I. Jiménez-Aquino and M. Romero-Bastida. "Fokker-Planck-Kramers equations of a heavy ion in presence of external fields". In: *Phys. Rev. E* 76.2 (2007), p. 021106. ISSN: 1539-3755. DOI: 10.1103/PhysRevE.76.021106.

[76] S. H. Jo, T. Chang, I. Ebong, B. B. Bhadviya, P. Mazumder, and W. Lu. "Nanoscale memristor device as synapse in neuromorphic systems". In: *Nano Lett.* 10.4 (2010), pp. 1297–1301. ISSN: 15306984. DOI: 10.1021/nl904092h.

[77] S. H. Jo, K.-H. Kim, and W. Lu. "High-density crossbar arrays based on a Si memristive system." In: *Nano Lett.* 9.2 (2009), pp. 870–4. ISSN: 1530-6984. DOI: 10.1021/nl8037689.

[78] Y. N. Joglekar and S. J. Wolf. "The elusive memristor: properties of basic electrical circuits". In: *Eur. J. Phys.* 30.4 (2009), pp. 661–675. ISSN: 0143-0807. DOI: 10.1088/0143-0807/30/4/001.

[79] F. Jülicher, A. Ajdari, and J. Prost. "Modeling molecular motors". In: *Rev. Mod. Phys.* 69.4 (1997), p. 1269.

[80] F. Jülicher, A. Ajdari, and J. Prost. "Modeling molecular motors". In: *Rev. Mod. Phys.* 69.4 (1997), pp. 1269–1282. ISSN: 0034-6861. DOI: 10.1103/RevModPhys.69.1269.

[81] A. Kaiser and H. Löwen. "Vortex arrays as emergent collective phenomena for circle swimmers". In: *Phys. Rev. E* 87.3 (2013), p. 032712. ISSN: 1539-3755. DOI: 10.1103/PhysRevE.87.032712.

[82] N. G. van Kampen. *Stochastic processes in physics and chemistry*. North Holland, 1992.

[83] A. Khintchine. "Korrelationstheorie der stationären stochastischen Prozesse". In: *Math. Ann.* 109.1 (1934), pp. 604–615. ISSN: 0025-5831. DOI: 10.1007/BF01449156.

[84] K.-H. Kim, S. Gaba, D. Wheeler, J. M. Cruz-Albrecht, T. Hussain, N. Srinivasa, and W. Lu. "A functional hybrid memristor crossbar-array/CMOS system for data storage and neuromorphic applications." In: *Nano Lett.* 12.1 (2012), pp. 389–95. ISSN: 1530-6992. DOI: 10.1021/nl203687n.

[85] T. R. Kline, W. F. Paxton, T. E. Mallouk, and A. Sen. "Catalytic Nanomotors: Remote-Controlled Autonomous Movement of Striped Metallic Nanorods". In: *Angew. Chemie Int. Ed.* 44.5 (2005), pp. 744–746. ISSN: 1433-7851. DOI: 10.1002/anie.200461890.

[86] S. Klumpp and R. Lipowsky. "Traffic of Molecular Motors through Tube-Like Compartments". In: *J. Stat. Phys.* 113.1-2 (2003), pp. 233–268. ISSN: 00224715. DOI: 10.1023/A:1025778922620.

[87] S. Klumpp, M. J. I. Muller, and R. Lipowsky. "Cooperative transport by small teams of molecular motors". In: 1.4 (2006), p. 9. ISSN: 1793-0480. DOI: 10.1142/S1793048006000288.

[88] A. B. Kolomeisky, G. M. Schütz, E. B. Kolomeisky, and J. P. Straley. "Phase diagram of one-dimensional driven lattice gases with open boundaries". In: *J. Phys. A. Math. Gen.* 31.33 (1998), pp. 6911–6919. ISSN: 0305-4470. DOI: 10.1088/0305-4470/31/33/003.

[89] J. Krug. "Boundary-induced phase transitions in driven diffusive systems". In: *Phys. Rev. Lett.* 67.14 (1991), pp. 1882–1885. ISSN: 00319007. DOI: 10.1103/PhysRevLett.67.1882.

[90] R. Kubo. "Statistical-mechanical theory of irreversible processes. I. General theory and simple applications to magnetic and conduction problems". In: *J. Phys. Soc. Jpn.* 12.6 (1957), pp. 570–586.

[91] M. Kumar, M. S. Mommer, and V. Sourjik. "Mobility of cytoplasmic, membrane, and DNA-binding proteins in Escherichia coli". In: *Biophys. J.* 98.4 (2010), pp. 552–559. ISSN: 00063495. DOI: 10.1016/j.bpj.2009.11.002.

[92] F. Kümmel, B. ten Hagen, R. Wittkowski, I. Buttinoni, R. Eichhorn, G. Volpe, H. Löwen, and C. Bechinger. "Circular Motion of Asymmetric Self-Propelling Particles". In: *Phys. Rev. Lett.* 110.19 (2013), p. 198302. ISSN: 0031-9007. DOI: 10.1103/PhysRevLett.110.198302.

[93] B. Kursunoglu. "Brownian motion in a magnetic field". In: *Ann. Phys. (N. Y).* 17.2 (1962), pp. 259–268. ISSN: 00034916. DOI: 10.1016/0003-4916(62)90027-1.

[94] P. Langevin. "The theory of Brownian movement". In: *CR Acad. Sci* 146 (1908), p. 530.

[95] M. H. R. Lankhorst, L. van Pieterson, M. van Schijndel, B. A. J. Jacobs, and J. C. N. Rijpers. "Prospects of Doped Sb-Te Phase-Change Materials for High-Speed Recording". In: *Jpn. J. Appl. Phys.* 42.Part 1, No. 2B (2003), pp. 863–868. ISSN: 0021-4922. DOI: 10.1143/JJAP.42.863.

[96] S. H. Larsen, R. W. Reader, E. N. Kort, W.-W. Tso, and J. Adler. "Change in direction of flagellar rotation is the basis of the chemotactic response in Escherichia coli". In: *Nature* 249.21 (1974), pp. 74–77. DOI: 10.1038/249074a0.

[97] R. J. Lasek. "Axonal transport of the cytoplasmic matrix". In: *J. Cell Biol.* 99.1 (1984), 212s–221. ISSN: 0021-9525. DOI: 10.1083/jcb.99.1.212s.

[98] M.-J. Lee, C. B. Lee, D. Lee, S. R. Lee, M. Chang, J. H. Hur, Y.-B. Kim, C.-J. Kim, D. H. Seo, S. Seo, U.-I. Chung, I.-K. Yoo, and K. Kim. "A fast, high-endurance and scalable non-volatile memory device made from asymmetric Ta_2O_{5-x}/TaO_{2-x} bilayer structures". In: *Nat. Mater.* 10.8 (2011), pp. 625–630. ISSN: 1476-1122. DOI: 10.1038/nmat3070.

[99] E. Lehtonen and M. Laiho. "CNN using memristors for neighborhood connections". In: *2010 12th Int. Work. Cell. Nanoscale Networks their Appl. (CNNA 2010)*. IEEE, 2010, pp. 1–4. ISBN: 978-1-4244-6679-5. DOI: 10.1109/CNNA.2010.5430304.

[100] D. Lencer, M. Salinga, and M. Wuttig. "Design rules for phase-change materials in data storage applications". In: *Adv. Mater.* 23.18 (2011), pp. 2030–2058. ISSN: 09359648. DOI: 10.1002/adma.201004255.

[101] C. Lenser, A. Koehl, I. Slipukhina, H. Du, M. Patt, V. Feyer, C. M. Schneider, M. Lezaic, R. Waser, and R. Dittmann. "Formation and Movement of Cationic Defects during Forming and Resistive Switching in $SrTiO_3$ Thin Film Devices". In: *Adv. Funct. Mater.* 25.40 (2015), pp. 6360–6368. ISSN: 16163028. DOI: 10.1002/adfm.201500851.

[102] D. Li, M. Li, F. Zahid, J. Wang, and H. Guo. "Oxygen vacancy filament formation in TiO2 : A kinetic Monte Carlo study". In: *J. Appl. Phys.* 112.7 (2012), p. 073512. ISSN: 0021-8979. DOI: 10.1063/1.4757584.

[103] F.-g. Li, H.-z. Xie, X.-m. Liu, and B.-q. Ai. "The influence of a phase shift between the top and bottom walls on the Brownian transport of self-propelled particles". In: *Chaos An Interdiscip. J. Nonlinear Sci.* 25.3 (2015), p. 033110. ISSN: 1054-1500. DOI: 10.1063/1.4916097.

[104] Y. Li, P. Jung, and A. Brown. "Axonal transport of neurofilaments: a single population of intermittently moving polymers." In: *J. Neurosci.* 32.2 (2012), pp. 746–58. ISSN: 1529-2401. DOI: 10.1523/JNEUROSCI.4926-11.2012.

[105] Y. Li, P. K. Ghosh, F. Marchesoni, and B. Li. “Manipulating chiral microswimmers in a channel”. In: *Phys. Rev. E* 90.6 (2014), p. 062301. ISSN: 1539-3755. DOI: 10.1103/PhysRevE.90.062301.

[106] R. L. Liboff. “Brownian Motion of Charged Particles in Crossed Electric and Magnetic Fields”. In: *Phys. Rev.* 141.1 (1966), pp. 222–227. ISSN: 0031-899X. DOI: 10.1103/PhysRev.141.222.

[107] B. Lindner, L. Schimansky-Geier, P. Reimann, P. Hänggi, and M. Nagaoka. “Inertia ratchets: A numerical study versus theory”. In: *Phys. Rev. E* 59.2 (1999), pp. 1417–1424. ISSN: 1063-651X. DOI: 10.1103/PhysRevE.59.1417.

[108] E. Linn, R. Rosezin, C. Kügeler, and R. Waser. “Complementary resistive switches for passive nanocrossbar memories.” In: *Nat. Mater.* 9.5 (2010), pp. 403–6. ISSN: 1476-1122. DOI: 10.1038/nmat2748.

[109] E. Linn, A. Siemon, R. Waser, and S. Menzel. “Applicability of well-established memristive models for simulations of resistive switching devices”. In: *IEEE Trans. Circuits Syst. I Regul. Pap.* 61.8 (2014), pp. 2402–2410. ISSN: 15498328. DOI: 10.1109/TCSI.2014.2332261.

[110] R. Lipowsky and S. Klumpp. “âLife is motion’: multiscale motility of molecular motors”. In: *Phys. A Stat. Mech. its Appl.* 352.1 (2005), pp. 53–112. ISSN: 03784371. DOI: 10.1016/j.physa.2004.12.034.

[111] R. Lipowsky, S. Klumpp, and T. M. Nieuwenhuizen. “Random walks of cytoskeletal motors in open and closed compartments”. In: *Phys. Rev. Lett.* 87.10 (2001), pp. 108101/1–108171/3. ISSN: 00319007. DOI: 10.1103/PhysRevLett.87.108101.

[112] C. Maggi, M. Paoluzzi, N. Pellicciotta, A. Lepore, L. Angelani, and R. Di Leonardo. “Generalized Energy Equipartition in Harmonic Oscillators Driven by Active Baths”. In: *Phys. Rev. Lett.* 113.23 (2014), p. 238303. ISSN: 0031-9007. DOI: 10.1103/PhysRevLett.113.238303.

[113] R. Mannella. “A Gentle Introduction to the Integration of Stochastic Differential Equations”. In: *Stoch. Process. Physics, Chem. Biol.* Vol. 557. Berlin, Heidelberg: Springer Berlin Heidelberg, 2000, pp. 353–364. ISBN: 978-3-540-41074-4. DOI: 10.1007/3-540-45396-2_32.

[114] S. Martens, G. Schmid, L. Schimansky-Geier, and P. Hänggi. “Entropic particle transport: Higher-order corrections to the Fick-Jacobs diffusion equation”. In: *Phys. Rev. E* 83.5 (2011), p. 51135. DOI: 10.1103/PhysRevE.83.051135.

[115] S. Martens, A. Straube, G. Schmid, L. Schimansky-Geier, and P. Hänggi. “Hydrodynamically enforced entropic trapping of Brownian particles”. In: *Phys. Rev. Lett.* 110.1 (2013), p. 010601. DOI: 10.1103/PhysRevLett.110.010601.

[116] C. Meis and J. Fleche. “Study of the solubility limit of oxygen vacancies in TiO_{2-x} using molecular dynamics”. In: *Solid State Ionics* 101-103 (1997), pp. 333–335. ISSN: 01672738. DOI: 10.1016/S0167-2738(97)84049-0.

[117] S. Menzel, U. Böttger, and R. Waser. “Simulation of multilevel switching in electrochemical metallization memory cells”. In: *J. Appl. Phys.* 111.1 (2012). ISSN: 00218979. DOI: 10.1063/1.3673239.

[118] T. Mirkovic, N. S. Zacharia, G. D. Scholes, and G. A. Ozin. “Nanolocomotion-Catalytic Nanomotors and Nanorotors”. In: *Small* 6.2 (2010), pp. 159–167. ISSN: 16136810. DOI: 10.1002/smll.200901340.

[119] H. Mori. “A Continued-Fraction Representation of the Time-Correlation Functions”. In: *Prog. Theor. Phys.* 34.3 (1965), pp. 399–416. ISSN: 0033-068X. DOI: 10.1143/PTP.34.399.

[120] M. J. I. Müller, S. Klumpp, and R. Lipowsky. “Tug-of-war as a cooperative mechanism for bidirectional cargo transport by molecular motors.” In: *Proc. Natl. Acad. Sci. U. S. A.* 105.12 (2008), pp. 4609–14. ISSN: 1091-6490. DOI: 10.1073/pnas.0706825105.

[121] National Institute of Health. *Fluorescence Microscopy*. URL: https://imagej.nih.gov/ij/images/FluorescentCells.jpg.

[122] H. Nazarian. *Crossbar Resistive Memory: The Future Technology for NAND Flash Industry Views on Current NAND Flash Technology*. 2013. URL: http://www.crossbar-inc.com/assets/resource/whitepaper/Crossbar-ReRAM-Technology-Whitepaper.pdf.

[123] Y. B. Nian, J. Strozier, N. J. Wu, X. Chen, and a. Ignatiev. “Evidence for an oxygen diffusion model for the electric pulse induced resistance change effect in transition-metal oxides”. In: *Phys. Rev. Lett.* 98.14 (2007), pp. 3–6. ISSN: 00319007. DOI: 10.1103/PhysRevLett.98.146403.

[124] L. Onsager. “Reciprocal Relations in Irreversible Processes. I.” In: *Phys. Rev.* 37.4 (1931), pp. 405–426. ISSN: 0031-899X. DOI: 10.1103/PhysRev.37.405.

[125] S. R. Ovshinsky. “Reversible electrical switching phenomena in disordered structures”. In: *Phys. Rev. Lett.* 21.20 (1968), pp. 1450–1453. ISSN: 00319007. DOI: 10.1103/PhysRevLett.21.1450.

[126] X. Pan, M.-Q. Yang, X. Fu, N. Zhang, and Y.-J. Xu. “Defective TiO_2 with oxygen vacancies: synthesis, properties and photocatalytic applications.” In: *Nanoscale* 5.9 (2013), pp. 3601–14. ISSN: 2040-3372. DOI: 10.1039/c3nr00476g.

[127] F. N. C. Paraan, M. P. Solon, and J. P. Esguerra. “Brownian motion of a charged particle driven internally by correlated noise”. In: *Phys. Rev. E* 77.2 (2008), p. 22101.

[128] A. Parmeggiani, T. Franosch, and E. Frey. "Phase Coexistence in Driven One-Dimensional Transport". In: *Phys. Rev. Lett.* 90.8 (2003), p. 086601. ISSN: 0031-9007. DOI: 10.1103/PhysRevLett.90.086601.

[129] A. Parmeggiani, T. Franosch, and E. Frey. "Totally asymmetric simple exclusion process with Langmuir kinetics". In: *Phys. Rev. E* 70.4 (2004), p. 046101. ISSN: 1539-3755. DOI: 10.1103/PhysRevE.70.046101.

[130] A. Parmeggiani, F. Jülicher, A. Ajdari, and J. Prost. "Energy transduction of isothermal ratchets: Generic aspects and specific examples close to and far from equilibrium". In: *Phys. Rev. E* 60.2 (1999), pp. 2127–2140. ISSN: 1063-651X. DOI: 10.1103/PhysRevE.60.2127.

[131] G. A. Patterson, P. I. Fierens, and D. F. Grosz. "On the beneficial role of noise in resistive switching". In: *Appl. Phys. Lett.* 103.7 (2013), p. 074102. ISSN: 0003-6951. DOI: 10.1063/1.4819018.

[132] G. A. Patterson, D. F. Grosz, and P. I. Fierens. "Noise on resistive switching: a Fokker-Planck approach". In: *J. Stat. Mech. Theory Exp.* 2016.5 (2016), p. 054043. ISSN: 1742-5468. DOI: 10.1088/1742-5468/2016/05/054043.

[133] G. A. Patterson, F. Sangiuliano Jimka, P. I. Fierens, and D. F. Grosz. "Memristors under the influence of noise and temperature". In: *Phys. status solidi* 12.1-2 (2015), pp. 187–191. ISSN: 18626351. DOI: 10.1002/pssc.201400125.

[134] F. Peruani and L. G. Morelli. "Self-propelled particles with fluctuating speed and direction of motion in two dimensions". In: *Phys. Rev. Lett.* 99.1 (2007), p. 10602. ISSN: 1079-7114.

[135] M. D. Pickett, D. B. Strukov, J. L. Borghetti, J. J. Yang, G. S. Snider, D. R. Stewart, and R. S. Williams. "Switching dynamics in titanium dioxide memristive devices". In: *J. Appl. Phys.* 106.7 (2009), p. 074508. ISSN: 00218979. DOI: 10.1063/1.3236506.

[136] N. Pottier. *Nonequilibrium statistical physics: linear irreversible processes*. Oxford University Press, USA, 2009.

[137] T. Prodromakis, B. P. Peh, C. Papavassiliou, and C. Toumazou. "A Versatile Memristor Model With Nonlinear Dopant Kinetics". In: *IEEE Trans. Electron Devices* 58.9 (2011), pp. 3099–3105. ISSN: 0018-9383. DOI: 10.1109/TED.2011.2158004.

[138] J. Prost, J. F. Chauwin, L. Peliti, and A. Ajdari. "Asymmetric pumping of particles". In: *Phys. Rev. Lett.* 72.16 (1994), pp. 2652–2655. ISSN: 00319007. DOI: 10.1103/PhysRevLett.72.2652.

[139] M. Prusty and H. Schanz. "Signature of Directed Chaos in the Conductance of a Nanowire". In: *Phys. Rev. Lett.* 96.13 (2006), p. 130601. ISSN: 1079-7114.

[140] M. Quintero, P. Levy, a. Leyva, and M. J. Rozenberg. "Mechanism of Electric-Pulse-Induced Resistance Switching in Manganites". In: *Phys. Rev. Lett.* 98.11 (2007), p. 116601. ISSN: 0031-9007. DOI: 10.1103/PhysRevLett.98.116601.

[141] P. K. Radtke, A. L. Hazel, A. V. Straube, and L. Schimansky-Geier. "Stochastic Dynamics of Resistive Switching: Fluctuations Lead to Optimal Particle Number". In: *New J. Phys.* 19.9 (2017), p. 093007. DOI: 10.1088/1367-2630/aa818b.

[142] P. K. Radtke and L. Schimansky-Geier. "Directed transport of confined Brownian particles with torque". In: *Phys. Rev. E* 85.5 (2012), p. 051110. ISSN: 1539-3755. DOI: 10.1103/PhysRevE.85.051110.

[143] P. K. Radtke and L. Schimansky-Geier. "A nonlinear HP-type complementary resistive switch". In: *AIP Adv.* 6.5 (2016), p. 055119. ISSN: 2158-3226. DOI: 10.1063/1.4952755.

[144] A. G. Radwan and M. E. Fouda. *On the Mathematical Modeling of Memristor, Memcapacitor, and Meminductor*. Vol. 26. Studies in Systems, Decision and Control. Cham: Springer International Publishing, 2015. ISBN: 978-3-319-17490-7. DOI: 10.1007/978-3-319-17491-4.

[145] J. B. Reece, L. A. Urry, M. L. Cain, S. A. Wasserman, P. V. Minorsky, and R. B. Jackson. *Campbell Biology*. 11th. Pearson Boston, 2016. ISBN: 978-0-134-09341-3.

[146] H. Risken. *The Fokker-Planck equation: Methods of solution and applications*. Springer Verlag, 1996.

[147] P. Romanczuk, M. Bär, W. Ebeling, B. Lindner, and L. Schimansky-Geier. "Active brownian particles". In: *Eur. Phys. J. Spec. Top.* 202.1 (2012), pp. 1–162. DOI: 10.1140/epjst/e2012-01529-y.

[148] L. W. Rossi, P. K. Radtke, and C. Goldman. "Long-range cargo transport on crowded microtubules: The motor jamming mechanism". In: *Phys. A Stat. Mech. its Appl.* 401 (2014), pp. 319–329. ISSN: 03784371. DOI: 10.1016/j.physa.2014.01.041.

[149] S. Roy. "Seeing the unseen: the hidden world of slow axonal transport." In: *Neuroscientist* 20.1 (2014), pp. 71–81. ISSN: 1089-4098. DOI: 10.1177/1073858413498306.

[150] M. J. Rozenberg, M. J. Sánchez, R. Weht, C. Acha, F. Gomez-Marlasca, and P. Levy. "Mechanism for bipolar resistive switching in transition-metal oxides". In: *Phys. Rev. B - Condens. Matter Mater. Phys.* 81.11 (2010), pp. 20–23. ISSN: 10980121. DOI: 10.1103/PhysRevB.81.115101.

[151] U. Russo, D. Kamalanathan, D. Ielmini, A. L. Lacaita, and M. N. Kozicki. "Study of multilevel programming in Programmable Metallization Cell (PMC) memory". In: *IEEE Trans. Electron Devices* 56.5 (2009), pp. 1040–1047. ISSN: 00189383. DOI: 10.1109/TED.2009.2016019.

[152] S. E. Savel'Ev, A. S. Alexandrov, A. M. Bratkovsky, and R. Stanley Williams. "Molecular dynamics simulations of oxide memristors: Crystal field effects". In: *Appl. Phys. Lett.* 99.5 (2011), pp. 19–22. ISSN: 00036951. DOI: 10.1063/1.3622665.

[153] S. E. Savel'ev, A. S. Alexandrov, A. M. Bratkovsky, and R. Stanley Williams. "Molecular dynamics simulations of oxide memory resistors (memristors)". In: *Nanotechnology* 22.25 (2011), p. 254011. ISSN: 0957-4484. DOI: 10.1088/0957-4484/22/25/254011.

[154] S. E. Savel'ev, A. S. Alexandrov, A. M. Bratkovsky, and R. S. Williams. "Molecular dynamics simulations of oxide memristors: thermal effects". In: *Appl. Phys. A* 102.4 (2011), pp. 891–895. ISSN: 0947-8396. DOI: 10.1007/s00339-011-6293-4.

[155] A. Schadschneider, D. Chowdhury, and K. Nishinari. *Stochastic transport in complex systems: from molecules to vehicles*. Elsevier, 2010. ISBN: 9780444528537.

[156] H. Schanz and M. Prusty. "Directed chaos in a billiard chain with transversal magnetic field". In: *J. Phys. A* 38 (2005), p. 10085.

[157] M. Schienbein and H. Gruler. "Langevin equation, Fokker-Planck equation and cell migration". In: *Bull. Math. Biol.* 55.3 (1993), pp. 585–608.

[158] C. Schindler, G. Staikov, and R. Waser. "Electrode kinetics of Cu-SiO_2-based resistive switching cells: Overcoming the voltage-time dilemma of electrochemical metallization memories". In: *Appl. Phys. Lett.* 94.7 (2009), pp. 2007–2010. ISSN: 00036951. DOI: 10.1063/1.3077310.

[159] W. Schirmacher, B. Fuchs, F. Höfling, and T. Franosch. "Anomalous Magnetotransport in Disordered Structures: Classical Edge-State Percolation". In: *Phys. Rev. Lett.* 115.24 (2015), p. 240602. ISSN: 0031-9007. DOI: 10.1103/PhysRevLett.115.240602.

[160] D. A. Scott, U. Das, Y. Tang, and S. Roy. "Mechanistic Logic Underlying the Axonal Transport of Cytosolic Proteins". In: *Neuron* 70.3 (2011), pp. 441–454. ISSN: 08966273. DOI: 10.1016/j.neuron.2011.03.022.

[161] A. Sen, M. Ibele, Y. Hong, and D. Velegol. "Chemo and phototactic nano/microbots". In: *Faraday Discuss.* 143 (2009), p. 15. ISSN: 1359-6640. DOI: 10.1039/b900971j.

[162] S. Shin, K. Kim, and S. M. Kang. "Compact models for memristors based on charge-flux constitutive relationships". In: *IEEE Trans. Comput. Des. Integr. Circuits Syst.* 29.4 (2010), pp. 590–598. ISSN: 02780070. DOI: 10.1109/TCAD.2010.2042891.

[163] A. Siemon, S. Menzel, A. Marchewka, Y. Nishi, R. Waser, and E. Linn. "Simulation of TaOx-based complementary resistive switches by a physics-based memristive model". In: *2014 IEEE Int. Symp. Circuits Syst.* 14. IEEE, 2014, pp. 1420–1423. ISBN: 978-1-4799-3432-4. DOI: 10.1109/ISCAS.2014.6865411.

[164] J. G. Simmons. "Generalized Formula for the Electric Tunnel Effect between Similar Electrodes Separated by a Thin Insulating Film". In: *J. Appl. Phys.* 34.6 (1963), pp. 1793–1803. ISSN: 00218979. DOI: 10.1063/1.1702682.

[165] T. P. Simões and R. E. Lagos. "Kramers equation for a charged Brownian particle: The exact solution". In: *Phys. A Stat. Mech. its Appl.* 355.2-4 (2005), pp. 274–282. ISSN: 03784371. DOI: 10.1016/j.physa.2005.03.034.

[166] Y. G. Sinai. "Dynamical systems with elastic reflections". In: *Russ. Math. Surv.* 25 (1970), p. 137.

[167] M. von Smoluchowski. "Zur kinetischen Theorie der Brownschen Molekularbewegung und der Suspensionen". In: *Ann. Phys.* 326.14 (1906), pp. 756–780. ISSN: 00033804. DOI: 10.1002/andp.19063261405.

[168] M. V. Smoluchowski. "Experimentell nachweisbare, der üblichen Thermodynamik widersprechende Molekularphänomene". In: *Phys. Zeitschrift* 13 (1912), p. 1069.

[169] G. S. Snider. "Spike-timing-dependent learning in memristive nanodevices". In: *2008 IEEE Int. Symp. Nanoscale Archit.* IEEE, 2008, pp. 85–92. ISBN: 978-1-4244-2552-5. DOI: 10.1109/NANOARCH.2008.4585796.

[170] A. Sokolov, M. M. Apodaca, B. A. Grzybowski, and I. S. Aranson. "Swimming bacteria power microscopic gears". In: *Proc. Natl. Acad. Sci.* 107.3 (2010), pp. 969–974. ISSN: 0027-8424, 1091-6490. DOI: 10.1073/pnas.0913015107.

[171] A. Stotland and M. Di Ventra. "Stochastic memory: Memory enhancement due to noise". In: *Phys. Rev. E* 85.1 (2012), p. 011116. ISSN: 1539-3755. DOI: 10.1103/PhysRevE.85.011116.

[172] D. B. Strukov, F. Alibart, and R. Stanley Williams. "Thermophoresis/diffusion as a plausible mechanism for unipolar resistive switching in metal-oxide-metal memristors". In: *Appl. Phys. A* 107.3 (2012), pp. 509–518. ISSN: 0947-8396. DOI: 10.1007/s00339-012-6902-x.

[173] D. B. Strukov, G. S. Snider, D. R. Stewart, and R. S. Williams. "The missing memristor found." In: *Nature* 453.7191 (2008), pp. 80–3. ISSN: 1476-4687. DOI: 10.1038/nature06932.

[174] K. Szot, W. Speier, G. Bihlmayer, and R. Waser. "Switching the electrical resistance of individual dislocations in single-crystalline $SrTiO_3$." In: *Nat. Mater.* 5.4 (2006), pp. 312–20. ISSN: 1476-1122. DOI: 10.1038/nmat1614.

[175] S. Tang, F. Tesler, F. G. Marlasca, P. Levy, V. Dobrosavljević, and M. Rozenberg. "Shock Waves and Commutation Speed of Memristors". In: *Phys. Rev. X* 6.1 (2016), p. 011028. ISSN: 2160-3308. DOI: 10.1103/PhysRevX.6.011028.

[176] Y. Tang, U. Das, D. A. Scott, and S. Roy. "The slow axonal transport of alpha-synuclein–mechanistic commonalities amongst diverse cytosolic cargoes." In: *Cytoskeleton (Hoboken).* 69.7 (2012), pp. 506–13. ISSN: 1949-3592. DOI: 10.1002/cm.21019.

[177] S. Tsui, A. Baikalov, J. Cmaidalka, Y. Y. Sun, Y. Q. Wang, Y. Y. Xue, C. W. Chu, L. Chen, and A. J. Jacobson. "Field-induced resistive switching in metal-oxide interfaces". In: *Appl. Phys. Lett.* 85.2 (2004), pp. 317–319. ISSN: 00036951. DOI: 10.1063/1.1768305.

[178] G. E. Uhlenbeck and L. S. Ornstein. "On the theory of the Brownian motion". In: *Phys. Rev.* 36.5 (1930), p. 823.

[179] I. Valov, E. Linn, S. Tappertzhofen, S. Schmelzer, J. van den Hurk, F. Lentz, and R. Waser. "Nanobatteries in redox-based resistive switches require extension of memristor theory." In: *Nat. Commun.* 4 (2013), p. 1771. ISSN: 2041-1723. DOI: 10.1038/ncomms2784.

[180] I. Valov, R. Waser, J. R. Jameson, and M. N. Kozicki. "Electrochemical metallization memories–fundamentals, applications, prospects." In: *Nanotechnology* 22.25 (2011), p. 254003. ISSN: 0957-4484. DOI: 10.1088/0957-4484/22/28/289502.

[181] S. Van Teeffelen and H. Löwen. "Dynamics of a Brownian circle swimmer". In: *Phys. Rev. E* 78.2 (2008), pp. 2–5. ISSN: 15393755. DOI: 10.1103/PhysRevE.78.020101.

[182] P. O. Vontobel, W. Robinett, P. J. Kuekes, D. R. Stewart, J. Straznicky, and R. Stanley Williams. "Writing to and reading from a nano-scale crossbar memory based on memristors." In: *Nanotechnology* 20.42 (2009), p. 425204. ISSN: 0957-4484. DOI: 10.1088/0957-4484/20/42/425204.

[183] I. Vourkas and G. C. Sirakoulis. "Nano-Crossbar Memories Comprising Parallel/Serial Complementary Memristive Switches". In: *Bionanoscience* 4.2 (2014), pp. 166–179. ISSN: 2191-1630. DOI: 10.1007/s12668-014-0132-y.

[184] R. Waser, R. Dittmann, G. Staikov, and K. Szot. "Redox-Based Resistive Switching Memories - Nanoionic Mechanisms, Prospects, and Challenges". In: *Adv. Mater.* 21.25-26 (2009), pp. 2632–2663. ISSN: 09359648. DOI: 10.1002/adma.200900375.

[185] C. Weber, P. K. Radtke, L. Schimansky-Geier, and P. Hänggi. "Active motion assisted by correlated stochastic torques". In: *Phys. Rev. E* 84.1 (2011), p. 011132. ISSN: 1539-3755. DOI: 10.1103/PhysRevE.84.011132.

[186] C. Weber, I. M. Sokolov, and L. Schimansky-Geier. "Active particles forced by an asymmetric dichotomous angle drive". In: *Phys. Rev. E* 85.5 (2012), p. 052101. DOI: 10.1103/PhysRevE.85.052101.

[187] S. Weitz, S. Blanco, R. Fournier, J. Gautrais, C. Jost, and G. Theraulaz. "Residence times and boundary-following behavior in animals". In: *Phys. Rev. E* 89.5 (2014), p. 052715. ISSN: 1539-3755. DOI: 10.1103/PhysRevE.89.052715.

[188] N. Wiener. "Generalized harmonic analysis". In: *Acta Math.* 55.C (1930), pp. 117–258. ISSN: 0001-5962. DOI: 10.1007/BF02546511.

[189] N. Yamada, E. Ohno, K. Nishiuchi, N. Akahira, and M. Takao. "Rapid-phase transitions of GeTe-Sb_2Te_3 pseudobinary amorphous thin films for an optical disk memory". In: *J. Appl. Phys.* 69.5 (1991), pp. 2849–2856. ISSN: 00218979. DOI: 10.1063/1.348620.

[190] T. Yanagida, K. Nagashima, K. Oka, M. Kanai, A. Klamchuen, B. H. Park, and T. Kawai. "Scaling effect on unipolar and bipolar resistive switching of metal oxides." In: *Sci. Rep.* 3.c (2013), p. 1657. ISSN: 2045-2322. DOI: 10.1038/srep01657.

[191] J. J. Yang, J. Borghetti, D. Murphy, D. R. Stewart, and R. S. Williams. "A Family of Electronically Reconfigurable Nanodevices". In: *Adv. Mater.* 21.37 (2009), pp. 3754–3758. ISSN: 09359648. DOI: 10.1002/adma.200900822.

[192] J. J. Yang, D. B. Strukov, and D. R. Stewart. "Memristive devices for computing." In: *Nat. Nanotechnol.* 8.1 (2013), pp. 13–24. ISSN: 1748-3395. DOI: 10.1038/nnano.2012.240.

[193] S. Yu, J. Liang, Y. Wu, and H.-S. P. Wong. "Read/write schemes analysis for novel complementary resistive switches in passive crossbar memory arrays." In: *Nanotechnology* 21.46 (2010), p. 465202. ISSN: 0957-4484. DOI: 10.1088/0957-4484/21/46/465202.

[194] K. B. Zeldovich, J. F. Joanny, and J. Prost. "Motor proteins transporting cargos". In: *Eur. Phys. J. E* 17 (2005), pp. 155–163. ISSN: 12928941. DOI: 10.1140/epje/i2004-10137-6.

[195] Y. Zhang. "Properties of tug-of-war model for cargo transport by molecular motors". In: *Phys. Rev. E* 79.6 (2009), p. 061918. ISSN: 1539-3755. DOI: 10.1103/PhysRevE.79.061918.

[196] F. Zhuge, K. Li, B. Fu, H. Zhang, J. Li, H. Chen, L. Liang, J. Gao, H. Cao, Z. Liu, and H. Luo. “Mechanism for resistive switching in chalcogenide-based electrochemical metallization memory cells”. In: *AIP Adv.* 5.5 (2015), p. 057125. ISSN: 2158-3226. DOI: 10.1063/1.4921089.

List of Publications

1. P. K. Radtke, A. L. Hazel, A. V. Straube, and L. Schimansky-Geier. "Stochastic Dynamics of Resistive Switching: Fluctuations Lead to Optimal Particle Number". In: *New J. Phys.* 19.9 (2017), p. 093007. DOI: 10.1088/1367-2630/aa818b

2. P. K. Radtke and L. Schimansky-Geier. "A nonlinear HP-type complementary resistive switch". In: *AIP Adv.* 6.5 (2016), p. 055119. ISSN: 2158-3226. DOI: 10.1063/1.4952755

3. L. W. Rossi, P. K. Radtke, and C. Goldman. "Long-range cargo transport on crowded microtubules: The motor jamming mechanism". In: *Phys. A Stat. Mech. its Appl.* 401 (2014), pp. 319–329. ISSN: 03784371. DOI: 10.1016/j.physa.2014.01.041

4. P. K. Radtke and L. Schimansky-Geier. "Directed transport of confined Brownian particles with torque". In: *Phys. Rev. E* 85.5 (2012), p. 051110. ISSN: 1539-3755. DOI: 10.1103/PhysRevE.85.051110

5. C. Weber, P. K. Radtke, L. Schimansky-Geier, and P. Hänggi. "Active motion assisted by correlated stochastic torques". In: *Phys. Rev. E* 84.1 (2011), p. 011132. ISSN: 1539-3755. DOI: 10.1103/PhysRevE.84.011132

Parts of the thesis have been published in these articles.

Danksagung

Zunächst möchte ich mich bei Prof. Schimansky-Geier für die Betreuung und Kooperation bedanken. Seine Ideen und Diskussionsfreude haben die Grundlage für diese Arbeit gelegt und die seine witzige und anekdotenreiche Art hat die Zusammenarbeit nie langweilig werden lassen.

No doutorado tive a oportunidade de pesquisar durante sete meses na Universidade de São Paulo sob a supervisão da Profa. Carla Goldman. O nosso trabalho cientifico foi baseado no respeito e atenção mutuos e nas boas ideias, que surgiam durante as nossas reunioes. Em relaçao a estadia em São Paulo so posso dizer que sempre me lembrarei desses sete meses particularmente a recepçao calorosa, com que as pessoas me receberam. Também gostaria de agradecer a Profa. Theresa Lamy, ao Marcos Markusawa, ao Fernando Villela, ao Tiago Oliveira, ao Erick Carvalho e a Gabriela Depetri pelo carinho e apoio.

Danke auch an alle Mitgliedern der TSP-TSD-TCSNP Gruppe für die angenehme Arbeitsatmosphäre und die unzähligen Stunden Konversation in der Kaffeeküche. Ich möchte besonders David Hansmann hervorheben, der bei allen Problemen stets hilfreich war und mein Graduiertenprogramm beeindruckend gut organisiert hat. Außerdem bedanke ich mich bei den jahrelangen Freunden und Kollegen Bernard Sonnenschein, Torsten Wendav, Sebastian Milster, Malte Kähne, Martin Rückl und Linn Dahms für ihr Feedback zu Teilen der Thesis und ihren Beitrag am Leben drum herum.

Schließlich gilt mein herzlicher Dank meinen Eltern, deren Förderung die Grundlage meines forschenden Geistes gelegt hat und die mich während all der Jahre meiner Ausbildung unermüdlich unterstützt haben.

Eigenständigkeitserklärung

Hiermit erkläre ich, dass ich die vorliegende Arbeit selbständig verfasst und keine anderen als die angegebenen Quellen und Hilfsmittel verwendet habe.

Berlin, den 03. Mai 2017

Paul Kaspar Radtke